SANDIA REPORT

SAND2005-5078
Unlimited Release
Printed August 2005

Deuterium Accelerator Experiments for APT

Kristin L. Hertz, Rion A. Causey, Donald F. Cowgill

Prepared by
Sandia National Laboratories
Albuquerque, New Mexico 87185 and Livermore, California 94550

Sandia is a multiprogram laboratory operated by Sandia Corporation,
a Lockheed Martin Company, for the United States Department of Energy's
National Nuclear Security Administration under Contract DE-AC04-94-AL85000.

Sandia National Laboratories

Issued by Sandia National Laboratories, operated for the United States Department of Energy by Sandia Corporation.

Available to DOE and DOE contractors from
U.S. Department of Energy
Office of Scientific and Technical Information
P.O. Box 62
Oak Ridge, TN 37831

Telephone: (865) 576-8401
Facsimile: (865) 576-5728
E-Mail: reports@adonis.osti.gov
Online ordering: http://www.doe.gov/bridge

Available to the public from
U.S. Department of Commerce
National Technical Information Service
5285 Port Royal Rd
Springfield, VA 22161

Telephone: (800) 553-6847
Facsimile: (703) 605-6900
E-Mail: orders@ntis.fedworld.gov
Online order: http://www.ntis.gov/help/ordermethods.asp?loc=7-4-0#online

SAND2005-5078
Unlimited Release
Printed August 2005

Deuterium Accelerator Experiments for APT

K. L. Hertz, R. A. Causey, D. F. Cowgill
Engineered Materials Department
Sandia National Laboratories
P.O. Box 969
Livermore, California 94551-9402

ABSTRACT

Sandia National Laboratories in California initiated an experimental program to determine whether tritium retention in the tube walls and permeation through the tubes into the surrounding coolant water would be a problem for the Accelerator Production of Tritium (APT), and to find ways to mitigate the problem, if it existed. Significant holdup in the tube walls would limit the ability of APT to meet its production goals, and high levels of permeation would require a costly cleanup system for the cooling water.

To simulate tritium implantation, a 200 keV accelerator was used to implant deuterium into Al 6061-T^ and SS316L samples at temperatures and particle fluxes appropriate for APT, for times varying between one week and five months.

The implanted samples were characterized to determine the deuterium retention and permeation. During the implantation, the D(d,p)T nuclear reaction was used to monitor the build-up of deuterium in the implant region of the samples.

These experiments increased in sophistication, from mono-energetic deuteron implants to multi-energetic deuteron and proton implants, to more accurately reproduce the conditions expected in APT.

Micron-thick copper, nickel, and anodized aluminum coatings were applied to the front surface of the samples (inside of the APT walls) in an attempt to lower retention and permeation.

The reduction in both retention and permeation produced by the nickel coatings, and the ability to apply them to the inside of the APT tubes, indicate that both nickel-coated Al 6061-T6 and nickel-coated SS316L tubes would be effective for use in APT.

The results of this work were submitted to the Accelerator Production of Tritium project in document number TPO-E29-Z-TNS-X-00050, APT-MP-01-17.

CONTENTS

LIST OF FIGURES

LIST OF TABLES

Intentionally Left Blank

Deuterium Accelerator Experiments for APT

1 Introduction

The concept of the Accelerator Production of Tritium (APT) device is to accelerate protons to very high energies, interact these protons with tungsten to produce spallation neutrons, multiply and moderate the neutrons in a water cooled Pb blanket, and then capture the neutrons on ^{3}He to produce tritium (T). The APT blanket will contain approximately 8,000 thin-walled tubes filled with ^{3}He to a pressure of 0.68 to 0.88 MPa. As the ^{3}He gas is converted to tritium, the tritium pressure generated on the inside of the tubes may result in some tritium retention in and permeation through the tubes. However, the tritium that is directly implanted into the tube walls by the exothermic ^{3}He(n,p)T reaction is of much greater concern.

The ^{3}He(n,p)T reaction provides the triton with a kinetic energy of 192 keV. Depending on the diameter of the tubes as well as the ^{3}He pressure, approximately 10 to 15 % of the tritium produced will be directly implanted into the tube walls. Depending on the location of the tubes in the APT blanket, the tritium flux incident on the tube walls will vary between 10^{10} and 10^{13} T/cm^2-s with an average of about 5×10^{11} T/cm^2-s. The temperature of the tubes will vary between about 330 and 370 K and the tubes will be fabricated from either 6061-T6 aluminum alloy (Al 6061-T6) or 316L stainless steel (SS 316L). If Al 6061-T6 is used, the wall thickness will be between 0.051 and 0.081 cm (0.020" and 0.032") thick and if SS 316L is used the thickness will be between 0.056 to 0.064 cm (0.022" to 0.025").

With the more or less constant tritium gas pressure and continuous energetic triton implantation, there is a real possibility that there will be substantial retention of tritium in the tube walls and/or permeation through the tubes into the surrounding coolant water. Neither of these conditions is deemed acceptable for APT operation. Significant holdup in the tube walls would limit the ability of APT to meet its production goals, and high levels of permeation would necessitate a very costly cleanup system for the cooling water.

An experimental program was initiated at Sandia National Laboratories in California to first determine if tritium retention and permeation may be a problem for APT, and then determine ways to mitigate these problems if they exist. To simulate the tritium implantation, a 200 keV accelerator was used to implant deuterium into Al 6061-T6 and SS 316L samples at temperatures and particle fluxes appropriate for APT for times varying between one week and five months. It was possible to use deuterium in these experiments because deuterium migration in materials is very similar to that for tritium. Diffusivity is expressed by the equation

$$D = D_o \exp(-E_D/kT). \qquad (1.1)$$

where D_o is the diffusion coefficient, E_D is the activation energy of diffusion, and k is the Boltzmann constant. The isotope dependence of migration is dependent on the structure of the host metal. Katz et al [1] found that in fcc copper and nickel the isotopic dependence for D_o is:

$$D_o(H):\ D_o(D):\ D_o(T):\ \approx 1:\ \frac{1}{\sqrt{2}}:\ \frac{1}{\sqrt{3}} \tag{1.2}$$

and for E_D is:

$$E_D(H) \geq E_D(D) \geq E_D(T) \tag{1.3}$$

The implanted samples were characterized to determine the deuterium retention and permeation. During the implantation, the D(d,p)T nuclear reaction was used to monitor the build-up of deuterium in the implant region of the samples. The deuterium retained in the samples after the implantation was measured with the use of a mass spectrometer during thermal desorption. In the final experiment, a zirconium layer was applied to the back surface of the samples to trap any deuterium that permeated through the sample. The Zr layer was then analyzed with the $D(^3He,p)^4He$ nuclear reaction to measure the trapped deuterium. Scanning electron microscopy (SEM) was used to image the surface and cross sections of the samples before and after implantation. These analysis techniques provided a thorough characterization of the samples.

During the last year of the program, the sophistication of the experiments was significantly increased. In the beginning, monoenergetic implants were used. The tritium produced by the $^3He(n,p)T$ reaction is monoenergetic. However, the tritium is emitted isotropically and at various distances from the APT tube walls. The tritium loses energy in the ^3He gas before striking the tube walls resulting in the continuous, linearly decreasing profile of ions implanted into the tube walls shown in Fig. 1.1. Initially, the experiments were improved by varying the energy of the implants to give a flat distribution of implanted particles in the samples. For the final experiments, the linearly decreasing profile (Fig. 1.1) was simulated by running for longer periods of time at the lower energies and shorter periods of time at the higher energies. The final improvement was the addition of protons, also energy tailored to match that of 576 keV protons from the $^3He(n,p)T$ reaction. The higher energy of the protons compared to the deuterons results in three times the number of protons striking the tube walls than deuterons. The proton profile is shown in Fig. 1.1 as well.

When initial measurements demonstrated that uncoated Al 6061-T6 and SS 316L retained a significant amount of the implanted tritium, micron-thick coatings were applied to the front surface of the samples (inside of the APT tube walls) in an attempt to lower this retention. Both copper and nickel coatings were examined. These materials

are relatively easy to apply to Al 6061-T6 and SS 316L, do not form stable oxides, and have relatively high tritium diffusivities and solubilities. The idea was to apply a coating that would permit rapid recombination of the implanted tritium and protium back into gas at the inner boundary, lowering both retention and permeation. A micron-thick layer of anodized aluminum on Al 6061-T6 was tested as well. The surface of anodized aluminum is porous increasing the surface where recombination may occur and possibly increasing the release of tritium.

This report describes all of the accelerator experiments performed on deuterium retention and permeation through APT materials at Sandia National Laboratories. The results of these experiments and the modeling used to understand the results are discussed as well.

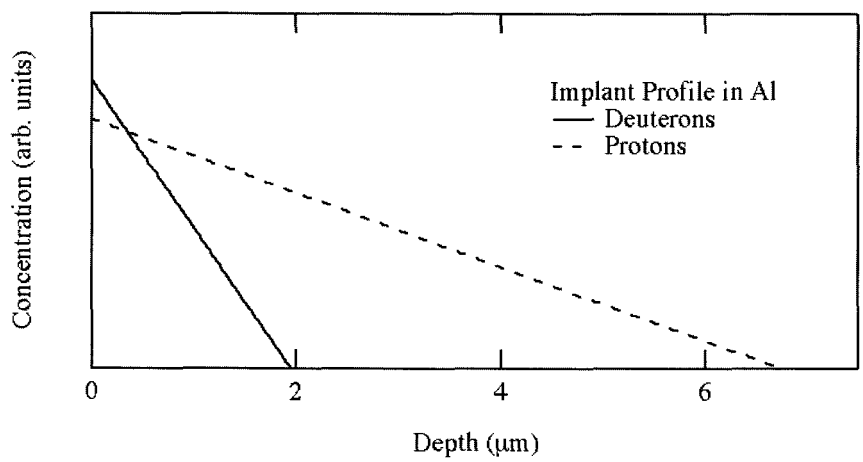

Figure 1.1: The calculated profiles expected in the APT tube walls for the 192 keV tritons and 576 keV protons produced in the $^{3}He(n,p)T$ reaction.

Intentionally Left Blank

2 Experimental Techniques

2.1 Deuteron and Proton Implantation

2.1.1 Experimental Equipment

The 200 keV and 750 keV accelerators at Sandia National Laboratories were used to implant deuterons and protons, respectively, into APT test samples. Six experiments were completed, after each experiment changes and improvements were made to the experimental apparatus. The schematic of the experimental assembly shown in Fig. 2.1 is of the final experimental configuration. The changes in the setup will be described in the experimental procedure for each run. Fig. 2.1 shows the setup used for deuteron and proton implants. The components marked by an * were added to the system when the 750 keV accelerator was installed. The 200 keV and 750 keV accelerators are located at ±15° from the analyzing magnet. The analyzing magnet selects the mass-to-charge ratio of the ion of interest from the various ions leaving the source of the accelerator. Immediately following the analyzing magnet are the stabilization slits used with the 750 keV accelerator. An aperture held at –200 V is used to reduce randomly scattered beam and to suppress electrons resulting from beam scattering. A rotating beam profiler allows the size and uniformity of the beam to be monitored throughout the experiment. To improve the vacuum and to reduce carbon build-up on the surface of the samples, a cold trap was added close to the sample holder. The liquid nitrogen cold trap uses temperature sensors to automatically fill the trap throughout the experiments. A quartz viewer may be inserted into the beam line to optically view the beam while conditioning before the run. Directly preceding the sample holder there is a foil ladder used to allow energy changes in the implanted deuterium without changing the beam energy. A picture of this setup is shown in Fig. 2.2.

The sample holder shown in Fig. 2.1 may be removed and replaced by beam line to allow the beam to continue through the apparatus shown in Fig. 2.3. The sample holder is moved to the position shown in Fig. 2.3 for $D(^3He,p)^4He$ nuclear reaction profiling. The quadrupole focus, left-right and top-bottom steerers, and slits are all used to provide a well-focused beam for this profiling technique.

2.1.2 Run 1 – Experimental Procedure

The first deuterium implantation experiment performed at Sandia National Laboratories, Run 1, used a monoenergetic 150 keV deuteron beam accumulated over 20 hours using 4 to 8 hour intervals. Al 6061-T6 samples were implanted with a flux of 2.6×10^{13} D/cm^2–s. This flux is considerably higher than those expected under APT conditions (10^{10} to 10^{13} T/cm^2–s), but allowed initial measurements to be made at high fluences quickly. The sample chamber base vacuum was 4×10^{-7} torr, but increased to 6×10^{-7} torr with the deuteron beam. The samples were heated to 348±2 K during the implantation. The sample block temperature was measured with a thermocouple. The

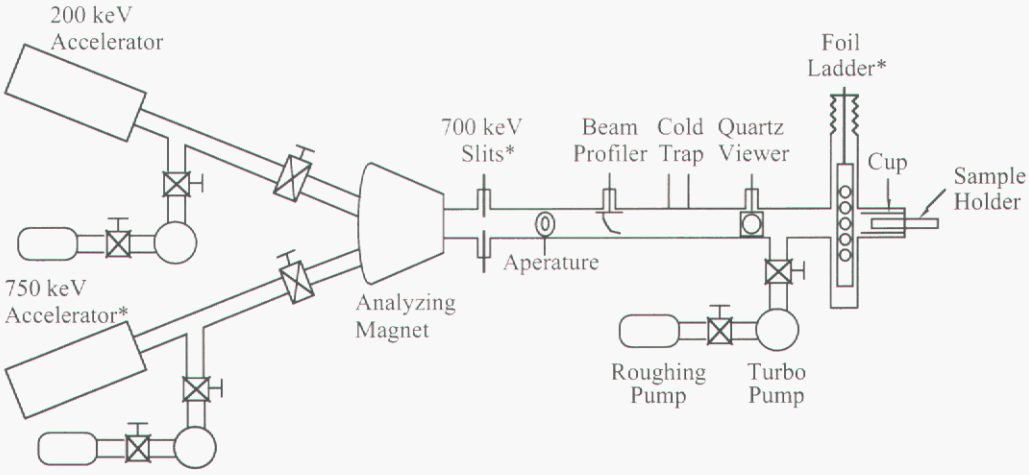

Figure 2.1: A schematic of the 200 keV and 750 keV accelerators used for the deuterium implantation experiments. The asterisk indicates the equipment added between Runs 4 and 5.

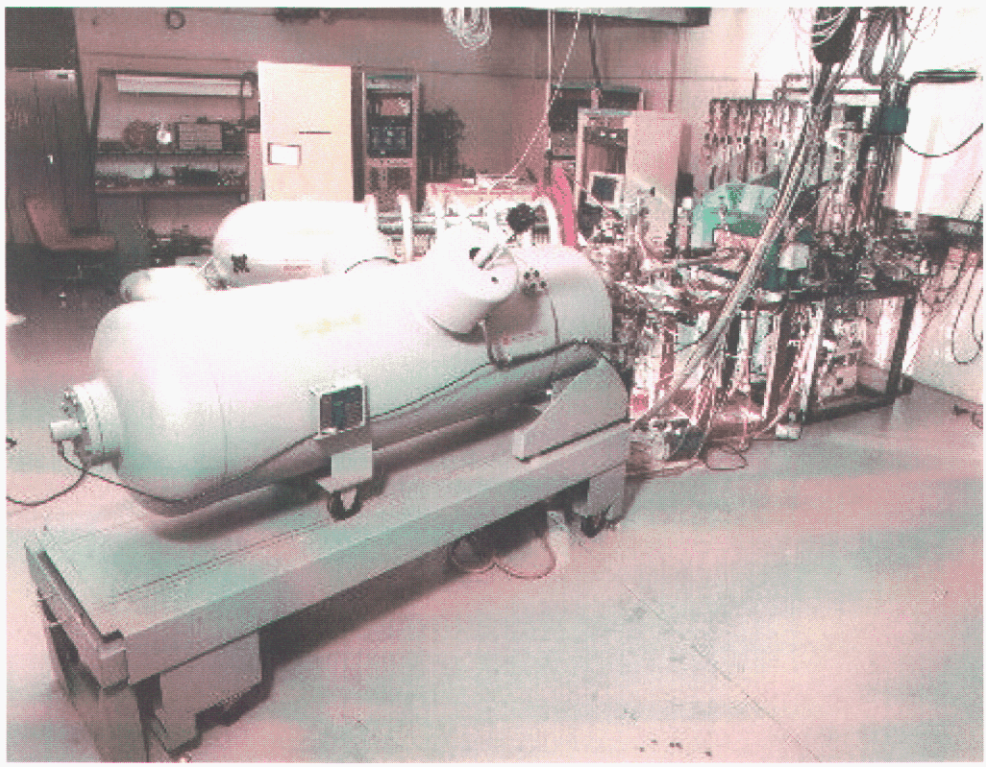

Figure 2.2: A picture of the 750 keV accelerator (foreground) and 200 keV accelerator (background) used for the implants and analysis of the samples.

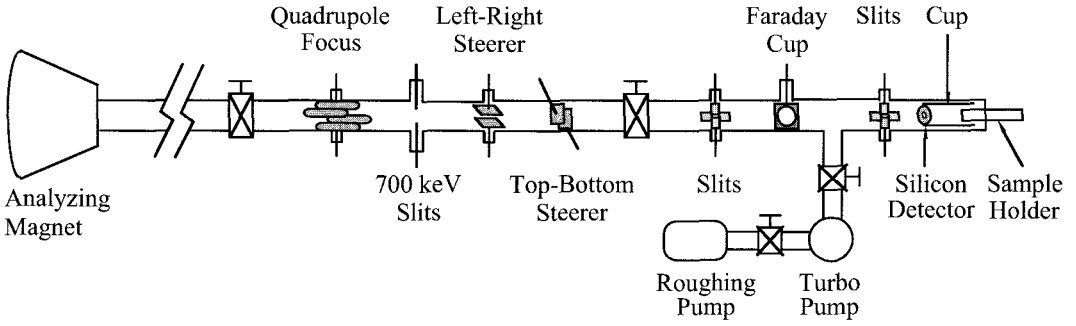

Figure 2.3: A schematic of the beam line assembly used for D(^{3}He,p)^{4}He nuclear reaction profiling. The sample holder in Figure 2.1 is removed and placed in the position shown here.

deuterium beam was focused to a removable quartz viewer for conditioning. A camera placed 135° from the beam was used to view the scintillation of the quartz by the ions. Fig. 2.4 shows the defocused beam that was elliptical in the vertical direction and had an area of approximately 6.44 cm^2. This allowed only three 0.635 cm (0.25") diameter Al 6061–T6 samples to be uniformly implanted simultaneously. As is seen in Fig. 2.4, five samples (darkly shaded) were mounted behind the three main samples to be used for post-implant analysis. When a beam of the proper shape, energy, and current was obtained the quartz viewer was removed and implantation began. A current integrator monitored the beam current. The integrated current was used to determine the total deuterium fluence implanted in the samples. When the desired fluence was reached, the implantation was stopped and the sample heaters were turned off.

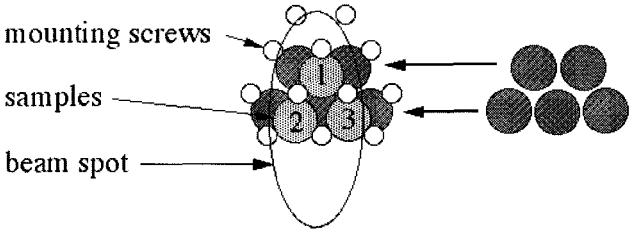

Figure 2.4: The beam spot overlaid on the samples implanted during Run 1. Two layers, lightly shaded in front and darkly shaded in back, of Al 6061–T6 samples were mounted. The right edge of sample 3 was not within the uniform beam spot. The mounting screws are also shown.

During implantation, a silicon detector with an active area of 100 mm^2 at an angle of 135° with respect to the beam was used to detect protons generated by the D(d,p)T nuclear reaction in real time. The analysis of the proton energy spectrum provides information on the amount of deuterium in the implant region of the sample during the implantation (see Sec. 2.3). The silicon detector subtended a solid angle of about 1 msr and collected protons from all of the samples, the sample mounting plate, and the mounting screws. Analysis of the proton spectrum from all of these components was completed.

The sample matrix for Run 1 primarily consisted of four Al 6061-T6 samples implanted with 150 keV deuterium to fluences of 0.46, 1.44 and 1.90x10^{18} D/cm^2. After

implantation to a fluence of $0.46x10^{18}$ D/cm^2, sample 1 was replaced to generate a suite of samples implanted to fluences of 0.46, 1.44 and $1.90x10^{18}$ D/cm^2. The aluminum samples were prepared from the same piece of 0.081 cm (0.032") thick certified Al 6061–T6 (see Appendix A). All samples discussed in this report were prepared by punching and cleaning with ethanol. Nothing else was done to the samples unless specified.

2.1.3 Run 2 – Experimental Procedure

Run 2 concentrated on a low flux implantation schedule to simulate APT conditions. There were a couple of improvements made to the experiment from Run 1. The first improvement was the implementation of a multi-energy implant procedure instead of the monoenergetic implant used in Run 1. The deuterium was implanted at energies of 10, 30, 70, 130, and 200 keV with an average flux of $5x10^{11}$ D/cm^2-s. Several Al 6061-T6 and both copper and nickel coated Al 6061–T6 samples were implanted during this experiment. Deuterium implantation profiles calculated using TRIM [2] are shown in Fig. 2.5 for a) aluminum, b) stainless steel, c) copper and d) nickel. The accelerator was tuned to one of the specified energies each day for approximately eight to ten hours resulting in a daily fluence of $1.5x10^{16}$ D/cm^2. Implantation began with 10 keV deuterons and stepped through each of the five energies to complete one cycle. The cycle was repeated four times until a total fluence of $4.46x10^{17}$ D/cm^2 was reached. The experiment took approximately 250 hours to complete.

The second improvement was made to the accelerator setup. The accelerator was moved back about 45 cm from the analyzing magnet before the start of this run. This allowed a larger and more uniform beam (see Fig. 2.6) than was available during Run 1. Thirdly, an Omega CN9000A temperature controller was connected to the sample heater. A NIST traceable calibrated thermocouple was connected to the sample block to measure the temperature (see Appendix A). A second thermocouple was mounted to the front of the sample holder, shown in Fig. 2.6. These improvements increased the accuracy with which the temperature of the samples was measured. Finally, a liquid nitrogen cold trap was added to the secondary electron suppressor electrode to improve the vacuum conditions and reduce carbon buildup on the samples. The pressure in the sample chamber during Run 2 was $1.4x10^{-7}$ torr.

The daily implant procedure began by filling the cold trap with LN. Then, the samples were heated to the desired temperature, 348±2 K for this experiment. The deuterium beam was then focused to the quartz viewer for conditioning. In addition to the visual assessment of the beam, a rotating wire beam profiler was added to the beam line to continuously monitor the beam uniformity throughout the experiment. The beam was defocused to form a collimated 2.5 cm diameter (4.91 cm^2) beam with < 10 % deviation in intensity over the entire beam spot. This large beam spot allowed seven samples shown in Fig. 2.6 to be implanted simultaneously. As with Run 1, when the proper beam was obtained, the quartz viewer was removed and implantation began. The current integrator monitored the beam current until the desired fluence was reached. Then, the quartz viewer was inserted into the beam and both the sample heaters and the liquid nitrogen were turned off. The silicon detector discussed in Run 1 was used to monitor protons from the D(d,p)T reaction during the 30, 70, 130 and 200 keV implants (see Sec. 2.3).

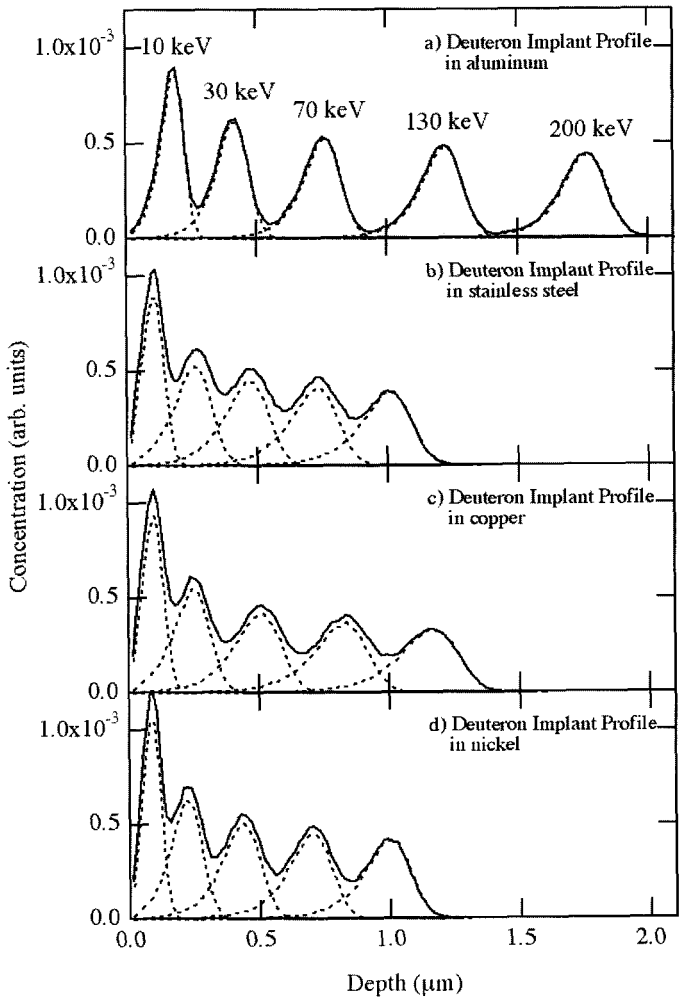

Figure 2.5: Deuterium implant profiles calculated with TRIM [2] in a) aluminum, b) stainless steel, c) copper and d) nickel. The dashed lines are the profiles for each of the single energy implants and the solid line is the sum profile.

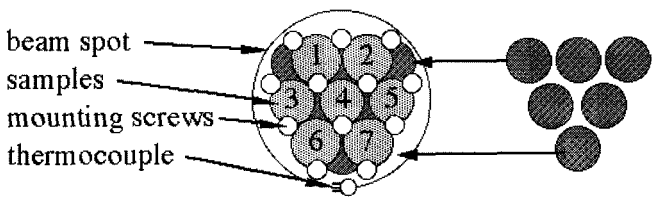

Figure 2.6: The beam spot overlaid on the samples implanted during Run 2. Two layers, lightly shaded in front and darkly shaded in back, of Al 6061–T6 samples were mounted. The mounting screws and the thermocouple are shown as well.

The sample matrix for Run 2 consisted of Al 6061-T6 and both copper and nickel coated Al 6061-T6 samples implanted with the deuterium energies and fluences listed in Table 2.1. The coated samples included an electroplated Ni coating, a plasma-plated Cu

coating, and a plasma-plated Ni coating. Two layers of samples were mounted on the sample holder as shown in Fig. 2.6. The six samples mounted in the back were all Al 6061–T6. All of the samples were prepared from the same piece of 0.081 cm (0.032") thick certified Al 6061-T6 (see Appendix A).

Table 2.1: The Al 6061–T6 sample matrix implanted during Run 2. Both single energy and multiple energy deuterium implants were completed. The multi-energy implants included deuterium implants at 10, 30, 70, 130, and 200 keV.

Position	Sample	Diameter (cm)	Implant Energy (keV)	Fluence (D/cm^2)
1.	Ni electroplate	0.714	Multi-energy	$4.463x10^{17}$
2.	Ni plasma plate	0.714	Multi-energy	$4.463x10^{17}$
3.	Al 6061-T6	0.635	10	$0.156x10^{17}$
			30	$0.156x10^{17}$
			70	$0.156x10^{17}$
			130	$0.161x10^{17}$
			200	$0.158x10^{17}$
			Multi-energy	$1.592x10^{17}$
				$2.084x10^{17}$
4.	Al 6061-T6	0.635	Multi-energy	$4.463x10^{17}$
5.	Al 6061-T6	0.635	Multi-energy	$0.787x10^{17}$
				$3.676x10^{17}$
6.	Al 6061-T6	0.714	Multi-energy	$4.463x10^{17}$
7.	Cu plasma plate	0.714	Multi-energy	$4.463x10^{17}$
Back	Al 6061-T6	0.635	Multi-energy	$4.463x10^{17}$

2.1.4 Run 3 – Experimental Procedure

A single Al 6061–T6 sample was implanted during Run 3. The original sample holder was replaced by a sample holder that allowed the back surface of the sample to be in contact with water of pH 3.5. The pH of the water was chosen to be comparable to that expected in the APT water coolant system. Slightly acidic water is normally used to reduce corrosion. The deuterium was implanted at 200 keV with an average flux of $6.63x10^{12}$ D/cm^2-s to a fluence of $1.35x10^{17}$ D/cm^2. The beam spot was the same as that used during Run 2, approximately 4.91 cm^2. Before the experiment began, the sample was heated to 348 K overnight. Then, the cold trap was filled, the beam was tuned and the implant began. The pressure during the implant was $3.3x10^{-7}$ torr. After implantation the sample heater was turned off and the water was removed. The liquid nitrogen cold trap remained filled until the sample was cool.

2.1.5 Run 4 - Experimental Procedure

Run 4 followed a long duration, low flux implantation schedule to simulate low flux APT conditions. The deuterium was implanted at energies of 10, 30, 70, 130, and 200 keV with an average flux of $1.7x10^{12}$ D/cm^2-s. The profiles of the implanted deuterium are the same as those in Run 2 (Fig. 2.5). The accelerator was tuned to one of the specified energies each day for approximately eight to ten hours. Implantation began with 10 keV deuterons and stepped through each of the five energies to complete one cycle. The cycle was repeated

until a total fluence of 3.04×10^{18} D/cm^2 was reached. The experiment took approximately 3 months to complete.

The Elcor model A310C current integrator used during these experiments was calibrated during these experiments. A Keithley 263 Calibrator/Source from Lawrence Livermore National Laboratories (serial number 40343) was used to check the linearity of the current reading and the integrator reading. The current reading was 3 % low and was corrected. The integrator reading was 4 % high.

The following procedure was used for the daily single-energy deuterium implantation. Before implantation began, the liquid nitrogen cold trap was filled, the samples were heated to 348±2 K and the deuterium beam was then focused to the quartz viewer for conditioning. Again, a collimated 2.5 cm diameter beam with < 10 % deviation in intensity over the entire beam spot was used. Seven samples were implanted simultaneously as shown in Fig. 2.7. When the quartz viewer was removed the current integrator monitored the beam current. After the desired fluence was reached, the quartz viewer was inserted into the beam line, the sample heater was turned off and finally the liquid nitrogen was turned off. The silicon detector monitored the proton yield produced in the D(d,p)T nuclear reaction during the deuteron implantation.

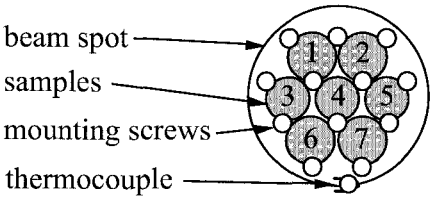

Figure 2.7: The beam spot overlaid on the samples implanted during Run 4. The samples, the mounting screws and the thermocouple are shown.

The samples exposed in this experiment allowed a comparison of the deuterium retention in the coated and bare samples. The sample matrix consisted of one Al 6061–T6, two Cu coated Al, two SS 316L, and two Cu coated SS samples as listed in Table 2.2. All samples were 0.714 cm (9/32") in diameter except sample 4 which was 0.635 cm (0.25") in diameter. The aluminum samples were prepared from the same piece of 0.081 cm (0.032") thick certified Al 6061-T6 (see Appendix A). The stainless steel samples were prepared from the same piece of 0.025 cm (0.010") thick SS 316L. The stainless steel samples all had two uncoated 0.025 cm thick stainless steel samples mounted behind them, so that they were 0.076 cm thick. This allowed them to be mounted securely to the sample holder with the same mounting screws as the thicker aluminum samples. The 6 μm Cu coatings were applied by an electroplating process. Two of each type of sample were implanted to study the build up of deuterium over time. After a fluence of 0.93×10^{18} D/cm^2 was reached one of each of the samples (excluding the single Al sample) was replaced with a new sample. This allowed samples implanted to fluences of 0.93×10^{18}, 2.11×10^{18}, and 3.04×10^{18} D/cm^2 to be reached by the end of the experiment. The Al 6061–T6 sample had been previously irradiated to a fluence of 0.46×10^{18} D/cm^2 during Run 2, resulting in a total fluence of 3.5×10^{18} D/cm^2 by the end of this experiment.

Table 2.2: The samples implanted during Run 4. The method used to prepare the samples and the fluences obtained during the experiment are listed.

Position	Sample	Sample Preparation	Fluence (D/cm^2)
1.	SS 316L	SS 316L, 0.025 cm thick	0.93 and $2.11x10^{18}$
2.	Cu coated SS	Electroplating	$3.04x10^{18}$
3.	Cu coated SS	Same as position 2.	0.93 and $2.11x10^{18}$
4.	Al 6061–T6	Al 6061-T6, 0.081 cm thick	$3.5x10^{18}$
5.	Cu coated Al	Electroplating	0.93 and $2.11x10^{18}$
6.	Cu coated Al	Same as position 5.	$3.04x10^{18}$
7.	SS 316L	Same as position 1.	$3.04x10^{18}$

2.1.6 Run 5 - Experimental Procedure

Four major improvements in the experimental setup were made before Run 5 began. The most important addition was that of the 750 keV accelerator shown in Fig. 2.1. This allowed the implantation of protons with energies up to 600 keV in addition to the deuterium. The 750 keV accelerator was placed at –15° with respect to the analyzing magnet to accommodate the 200 keV accelerator that is located at +15°. Simply changing the polarization of the magnet allows the use of either accelerator. Unlike the 200 keV accelerator, the 750 keV accelerator does not maintain a constant voltage without a proper stabilization system. Therefore, slits were installed in the beam line before the beam profiler to be used in conjunction with the accelerator's corona points to provide a very stable beam.

Secondly, a foil ladder (visible in Fig. 2.8) was added to vary the energy of the implanted deuterium without changing the voltage of the accelerator, the foil ladder was not used for the proton implants. This allowed energy changes to be made without an experimenter present, making it possible to run the experiment overnight and decrease the number of days needed to reach the fluences of interest to APT. The foil ladder is located directly in front of the samples to prevent loss of the beam due to scattering in the foils. The foil ladder consists of 0.5, 1.0, 1.5 μm thick 99.1 % pure Al foils and a piece of Reynolds Wrap aluminum foil to act as a beam stop.

The third improvement was an array of five silicon detectors to measure the charged particles emitted during the 200 keV deuterium implants (visible in Fig. 2.8). Protons from the D(d,p)T reaction at 200 keV were measured to provide information on the deuterium build-up over time in the implanted region of the samples. These detectors were well collimated so that protons scattered from only one sample were collected in each detector. This was a significant improvement over Run 4 where the silicon detector saw all of the samples. Five of the seven samples (samples 1-5 in Table 2.4) were individually monitored by a detector. Sec. 2.3 provides a complete discussion of the nuclear reaction profiling analysis.

Finally, a LabVIEW program was designed to monitor the experiment and control the movement of the foil ladder. The sample temperature, beam flux, beam fluence, and sample pressure were periodically recorded manually. The LabVIEW program recorded the beam flux on a strip chart and saved the charged particle spectra from the silicon detectors at

specified intervals throughout the experiment. During the deuterium implantation the foil ladder was programmed to shuffle through the foils to vary the implant energy.

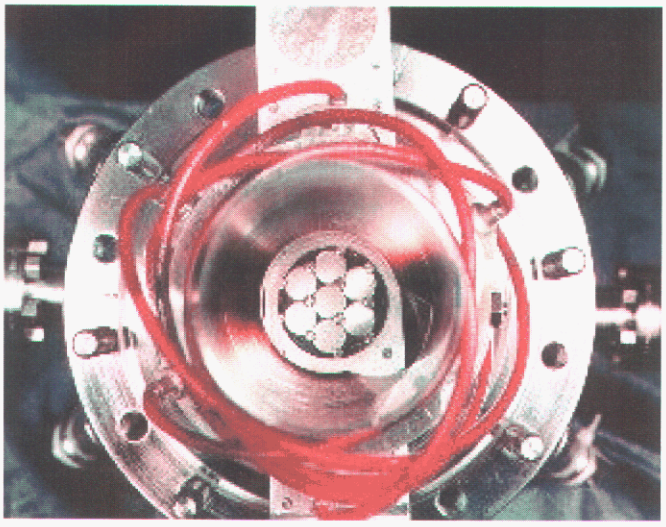

Figure 2.8: A picture of the seven Al 6061–T6 samples mounted on the sample holder used during Runs 5 and 6. The cup used to suppress scattered electrons and the foil ladder are visible. The five red cables are connected to the five silicon detectors used for nuclear reaction profiling.

This experiment proceeded in a manner similar to the daily schedule of Run 4. The cold trap was filled with liquid nitrogen and then the samples were heated to 373±5 K. The deuteron or proton beam was conditioned on the quartz viewer and then implantation began. The experiment progressed through 9 cycles alternating between deuteron and proton implants. The deuterium was implanted at the energies and fluences listed in Table 2.3. A 200 keV beam was tuned to the samples and the foil ladder shuffled through the foils in the order listed in the table. The protons were implanted at the energies and fluences listed in Table 2.4. The 700 keV accelerator loses stability at energies lower than 150 keV, thus the lowest proton energy implanted was 150 keV. The proton implants began with the 150 keV energy beam and stepped through each of the energies in the order listed in the table. The profiles for the implanted deuterons and protons calculated using TRIM [2] are shown in Fig. 2.9 for a) aluminum, b) stainless steel, c) copper, d) nickel and e) anodized aluminum. The deuterons and protons were implanted with average fluxes of 1.0×10^{13} ions/cm^2-s to a total fluence of 3×10^{18} D/cm^2 and 3×10^{18} p/cm^2. Running for longer periods of time at the lower energies and shorter periods of time at the higher energies simulated a linearly decreasing deuteron and proton profile shown if Fig. 2.9.

Run 5 had several goals. The main objective was to look at the effects of higher temperature and flux to simulate conditions of APT near the spallation source. The inclusion of proton implants for the first time is also important. During APT operation the ^{3}He tube walls will be simultaneously bombarded with tritons and protons. Three times as many protons as tritons will strike the tube walls due to the higher energy of the emitted protons and the geometry of the tubes. There are several differences between the APT conditions and these experiments. The first is that an equal number of deuterons and protons were implanted instead of three times the number of protons compared to deuterons. The differences in the theoretical APT deuteron and proton profiles and the experimental profiles for aluminum are shown in Fig. 2.9a). Secondly, the proton and deuteron implants alternate,

they are not simultaneous. This probably has the greatest effect on the results. And finally, the protons were implanted at energies greater than 150 keV. In APT, protons will be implanted into the tube walls with energies between 0 and 592 keV. This would increase the damage in the APT tube walls compared to these experiments. These differences will be recalled when the experimental results are discussed and summarized.

Table 2.3: The linear deuteron implant profile followed during Run 5. The cycle was repeated nine times alternating with the protons to equal the total fluence.

Deuteron Energy (keV)	Foil thickness (μm)	Cycle Fluence (D/cm^2)	Total Fluence (D/cm^2)
14	1.5	1.19×10^{17}	1.07×10^{18}
78	1.0	9.52×10^{16}	8.57×10^{17}
140	0.5	7.14×10^{16}	6.43×10^{17}
200	None	4.76×10^{16}	4.29×10^{17}
TOTAL		3.33×10^{17}	3.00×10^{18}

Table 2.4: The linear proton implant profile followed during Run 5. The cycle was repeated nine times alternating with the deuterons to equal the total fluence.

Proton Energy (keV)	Cycle Fluence (p/cm^2)	Total Fluence (p/cm^2)
150	7.62×10^{16}	6.86×10^{17}
225	6.67×10^{16}	6.00×10^{17}
300	5.71×10^{16}	5.14×10^{17}
375	4.76×10^{16}	4.29×10^{17}
450	3.81×10^{16}	3.43×10^{17}
525	2.86×10^{16}	2.57×10^{17}
600	1.90×10^{16}	1.71×10^{17}
TOTAL	3.33×10^{17}	3.00×10^{18}

The new sample holder shown in Fig. 2.8 was used during Runs 5 and 6 and was designed to hold seven 7.9 mm (5/16") diameter samples. The two thermocouples were mounted the same way they were on the previous sample holder. One thermocouple was attached to the sample block and the other was mounted to the front side of the sample holder as shown in Fig. 2.7. The samples used in this experiment were chosen to study the retention of deuterium in coated and bare Al 6061–T6. The sample matrix consisted of one Al 6061–T6, one anodized Al, three Cu coated Al, and two Ni coated Al samples (see Table 2.5). All of the sample substrates were 0.081 cm (0.032") thick certified Al 6061–T6 (see Appendix A). After two-thirds of the total fluence was reached, samples 1, 2, 6, and 7 were replaced with new samples so that samples implanted to fluences of 1×10^{18}, 2×10^{18}, and 3×10^{18} D/cm^2 (and p/cm^2) were obtained by the end of the experiment.

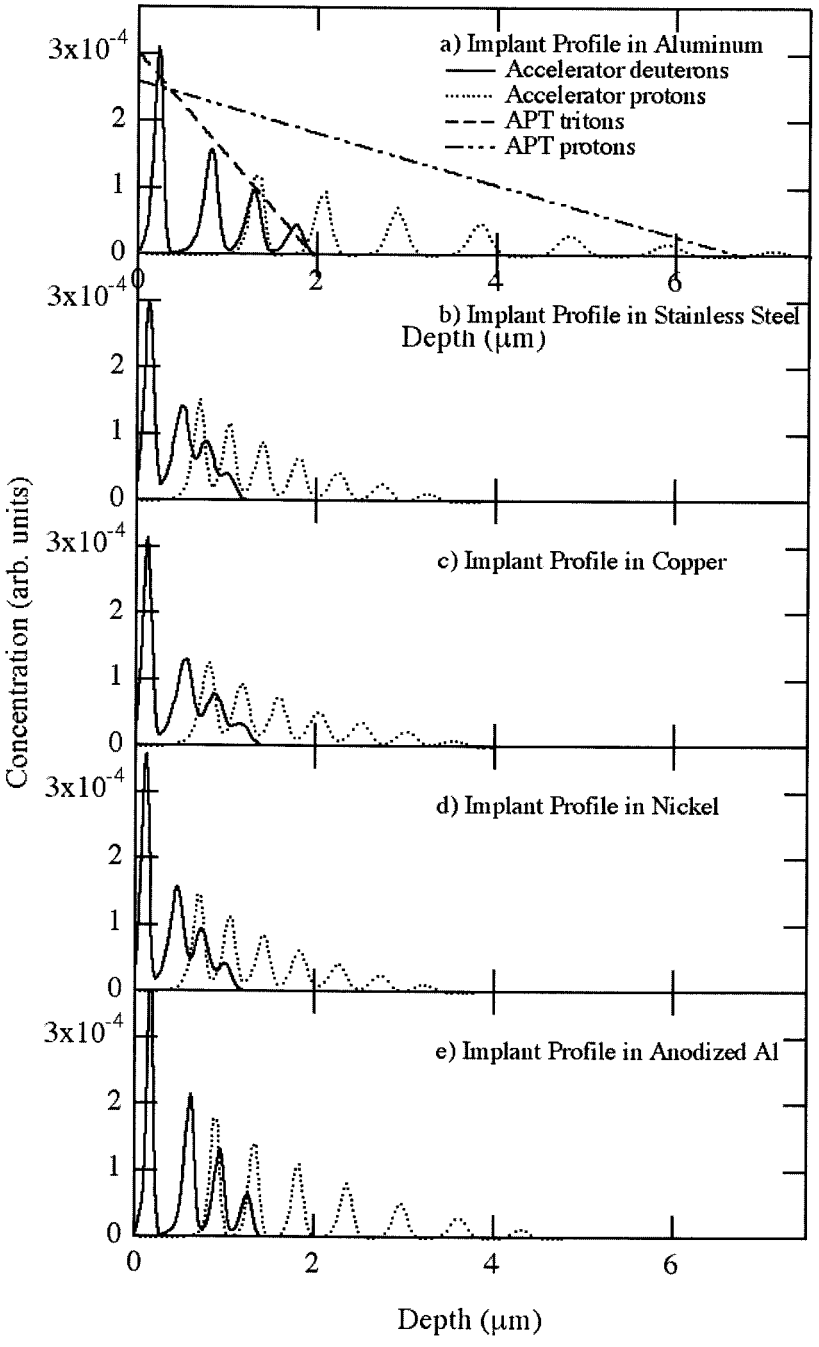

Figure 2.9: Run 5 implantation profiles for deuterons (solid curves) and protons (dashed curves) calculated using TRIM [2]. The implant profiles are based on the energy profiles given in Tables 2.3 and 2.4 for a) aluminum, b) stainless steel, c) copper, d) nickel and e) anodized aluminum. The dashed lines in a) are the theoretical deuteron and proton implant profiles expected for aluminum tubes in APT for comparison to the experimental profiles.

Table 2.5: The samples implanted in Run 5. The methods used to prepare the samples and the fluences obtained during the experiment are listed.

Position	Sample	Sample Preparation	Fluence (D/cm^2)
1.	Anodized Al	20 μm thick anodized coating	1 and 2 $x10^{18}$
2.	Al 6061-T6	Al 6061-T6, 0.081 cm thick	1 and 2 $x10^{18}$
3.	Cu coated Al	Electroless electroplating process: 1 minute Ni deposition at 372 K 120 minutes Cu deposition at 316 K	3 $x10^{18}$
4.	Ni coated Al	Electroless electroplating process: Zincated 20 minutes Ni deposition at 361 K	3 $x10^{18}$
5.	Cu coated Al	Electroplated: Zincated Cu plating for 7 minutes at 10 ASF	3 $x10^{18}$
6.	Ni coated Al	Same as sample 4.	1 and 2 $x10^{18}$
7.	Cu coated Al	Same as sample 5.	1 and 2 $x10^{18}$

2.1.7 Run 6 – Experimental Procedure

The beam line shown in Fig. 2.3 was added to the experimental setup before the start of Run 6. This addition allowed for measurements of the deuterium that permeated through the samples. The permeated deuterium was trapped in a thin zirconium layer applied to the back surface of the samples. This layer was then analyzed by D(3He,p)4He nuclear reaction profiling to measure the amount of trapped deuterium (see Sec. 2.4 for details). The deuteron and proton implant schedule of Run 6 was the same as Run 5. However, after each 1x1018 D (and p)/cm2 interval the samples were removed, turned over, and the zirconium layer was analyzed.

The samples implanted during this experiment were chosen to compliment those implanted during Run 5 and to provide permeation measurements for all possible APT candidate materials. The large list of samples is given in Table 2.6. Bare SS 316L, copper coated SS 316L, and nickel coated SS 316L were implanted to 1x1018 and 2x1018 D (and p)/cm2. These samples were used to provide deuterium retention data. All of the stainless steel samples were made from 0.025 cm (0.010") thick SS 316L. A 0.5 μm thick zirconium layer was evaporated onto the back surface of one sample of all six candidate samples for permeation measurements. The oxide layer on the sample surface was removed by sputtering before the zirconium layer was applied. An oxide layer between the sample and the zirconium layer would prevent the deuterium from entering the zirconium. The Al 6061–T6 samples were implanted to a fluence of 3x1018 D (and p)/cm2 and the SS 316L samples were implanted to 5x1018 D (and p)/cm2.

Table 2.6: The samples implanted in Run 6. The methods used to prepare the samples and the fluences obtained during the experiment are listed.

Position	Sample	Sample Preparation	Fluence (D/cm^2)
1.	S/Zr	316L SS, 0.025 cm thick□0.82 μm Zr layer	5×10^{18}
2.	Cu/SS/Zr	3 minutes watts nickel at 50 ASF at room temperature for adhesion. 20 minutes acid copper sulfate at 25 ASF at room temperature. 0.50 μm Zr layer	5×10^{18}
3.	Ni/SS/Zr	5 μm thick Ni coating 20 minutes nickel sulfamate at 20 ASF 0.81 μm Zr layer	5×10^{18}
4.	Al/Zr	6061-T6 Al, 0.81 cm thick 0.63 μm Zr layer	2×10^{18}
	Ni/Al/Zr	Ni coated Al sample used in Run 5 0.5 μm Zr layer	3×10^{18}
5.	SS	Same as sample 1 (without Zr).	2×10^{18}
	Al/Zr	0.63 μm Zr layer	3×10^{18}
6.	Ni/SS	Same as sample 3 (without Zr).	1 and 2×10^{18}
	Cu/SS	Same as sample 2 (without Zr).	1×10^{18}
	SS	Same as sample 1 (without Zr).	1×10^{18}
7.	Cu/SS	Same as sample 2 (without Zr).	2×10^{18}
	Cu/Al/Zr	Electroless Cu coated Al sample used in Run 5 0.51 μm Zr layer	3×10^{18}

2.2 Thermal Desorption Spectroscopy (TDS)

2.2.1 TDS Experimental Equipment

Thermal desorption spectroscopy was used to measure the amount of deuterium retained within the samples after implantation. A schematic of the equipment used with the radiant vacuum furnace and mass spectrometer to thermally desorb the samples is shown in Fig. 2.10. A sample loader and a moveable sample holder allow the furnace to remain under vacuum when a new sample is placed in the system; this reduces the amount of background contamination measured by the spectrometer. The mass spectrometer is calibrated preceding each desorption with a D_2 standard leak. The furnace is regulated by a programmable temperature controller. The controller ramps the temperature at a specified rate while the elapsed time, temperature, and selected mass peaks from the mass spectrometer are read into a computer and saved to a data file.

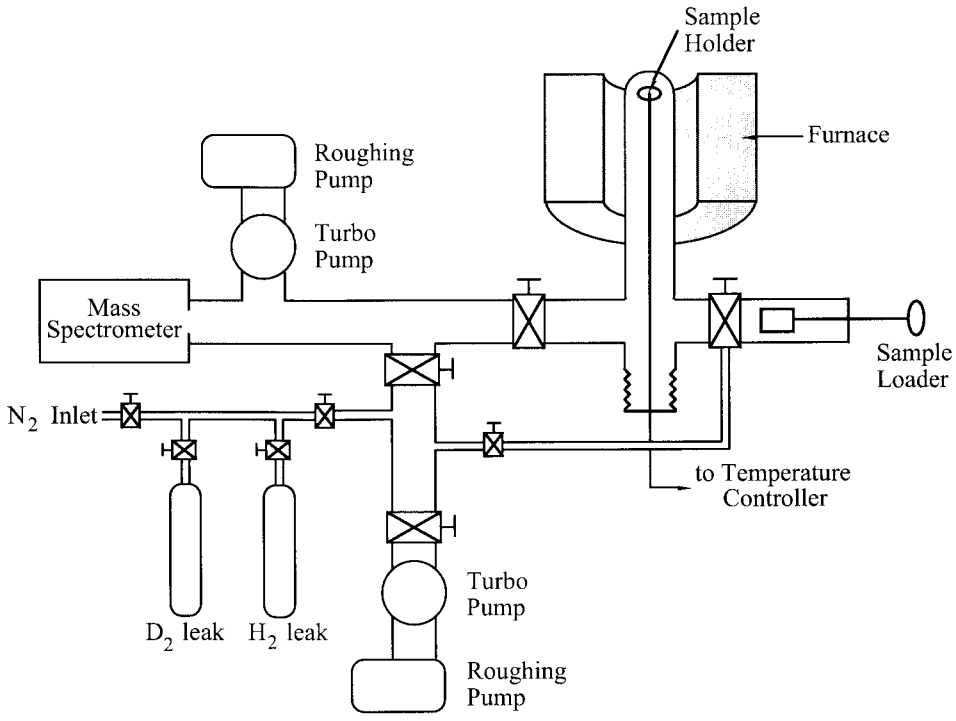

Figure 2.10: A schematic of the thermal desorption experimental apparatus.

2.2.2 TDS Experimental Procedure

The following procedure was used to thermally desorb the implanted samples. The sample was loaded into the furnace and pumped for approximately 10 minutes down to a pressure of $2x10^{-7}$ torr. At this time, the calibration leak was opened to the mass spectrometer and the computer started accumulating data. The leak was then closed off from the mass spectrometer and the temperature ramp of the furnace began. The furnace was programmed to ramp the temperature at a rate of 1 K/s. The coated and bare Al 6061–T6 samples were heated to 903 K, just below the 933 K melting temperature of aluminum. The coated and bare SS 316L samples were heated to 1273 K. The temperature was maintained until desorption of the relevant masses was completed. Data on H_2, HD, D_2, and various water and methane molecules (masses 2, 3, 4, 16, 17, 18, 19 and 20) were collected by the mass spectrometer and recorded in a data file for analysis. The total quantity of deuterium released from the sample was calculated by integrating the mass spectrometer signals over time and adding the deuterium contributions from the various molecules.

Samples that were not implanted were desorbed to use as a baseline comparison for the implanted samples. There are two major considerations in assuring an accurate measurement of the total retained deuterium. Is the apparatus absorbing deuterium? The D_2 leak calibration will account for any fraction of deuterium that may be absorbed by the system because the calibration is done under the same conditions as the desorption. Secondly, is any deuterium being retained in the system during the temperature ramp? Generally, between desorptions the furnace was ramped without a sample. No HD or D_2 (masses 3 and 4) were

seen during these ramps indicating that deuterium was not absorbed into the apparatus. There is a possibility that some deuterium was not desorbed from the nickel and stainless steel due to their high melting points, 1728 K and 1675 K. respectively. However, the HD and D_2 signals generally returned to zero before the end of the temperature ramp indicating that all of the deuterium was released.

2.3 D(d,p)T Nuclear Reaction Profiling

The deuteron beam is unique in that it can be used to simultaneously implant deuterium and probe the accumulation of deuterium in the implant-region of the sample via the D(d,p)T nuclear reaction. Incoming deuterons may react with previously implanted deuterons that are still in the metal producing a proton. A silicon detector is used to measure the number and energy of the emitted protons. These measurements are used to calculate the concentration of deuterium versus depth in the near-surface region of the sample over time.

2.3.1 D(d,p)T Experimental Equipment

A schematic diagram of the experimental setup used for the nuclear reaction profiling of a single sample during Runs 5 and 6 is shown in Fig. 2.11. The setup of the silicon detector used during Runs 1 through 4 was the same as that shown in Fig 2.11, except for the omission of the collimator. Without the collimator, protons resulting from the D(d,p)T reaction in the sample holder and all of the samples were collected in the detector. The collimator restricted the detectors to measuring charged particles from a single sample. The following discussion concentrates on the analysis of the data collected during Runs 5 and 6. The deuteron beam is incident normal to the sample. A silicon detector located at 135° with respect to the beam monitors the sample during the 200 keV deuterium implants. A collimator placed in front of the detector insures that only particles scattered at 135° from a single 0.49 cm^2 sample can enter the detector. The detector subtends a solid angle of 0.0177 sr, calculated from the geometry of the experimental setup. A 2 μm thick aluminum foil placed in front of the detector stops the low energy backscattered deuterons while allowing the tritons and protons to pass through to the detector. At specified intervals throughout the implantation, LabVIEW records the energy signals from the silicon detector and the integrated current. Fig. 2.12 shows the raw data accumulated from the silicon detector. The tritons and protons are easily identified.

2.3.2 D(d,p)T Experimental Procedure

A general description of the nuclear reaction profiling analysis procedure follows. For a more detailed description of the D(d,p)T profiling technique and the limitations of this method the reader is referred to a paper by Cowgill [3]. The experimentally measured quantities during the implantation are the number of protons and their energies. To equate the measured proton energy with the depth of the D(d,p)T reaction in the sample one must consider the energy loss of the incident deuterons in the sample, the D(d,p)T nuclear reaction, the energy loss of the emitted proton as it exits the sample and the energy loss of the proton in the Al foil before the detector. Fig. 2.13 illustrates the path of the incident deuteron and the emitted proton from the D(d,p)T reaction.

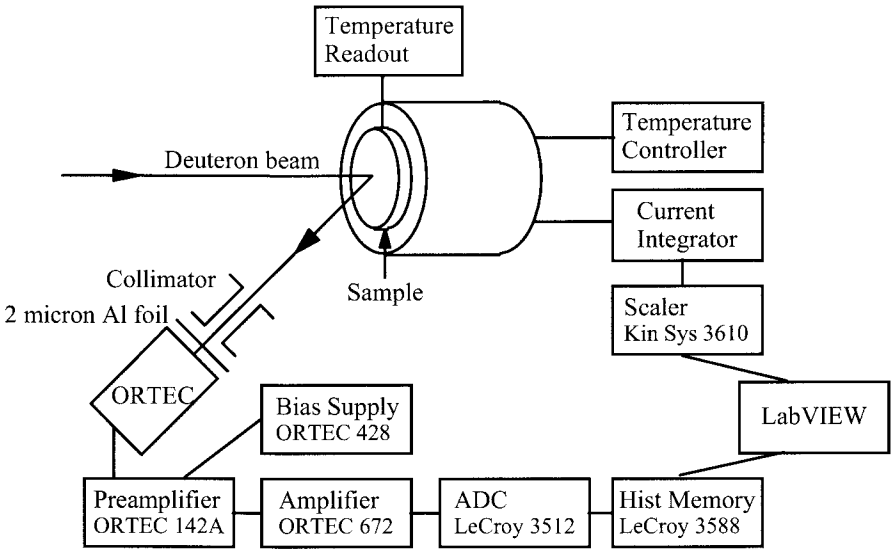

Figure 2.11: A diagram of the experimental setup for the nuclear reaction profiling during Run 5.

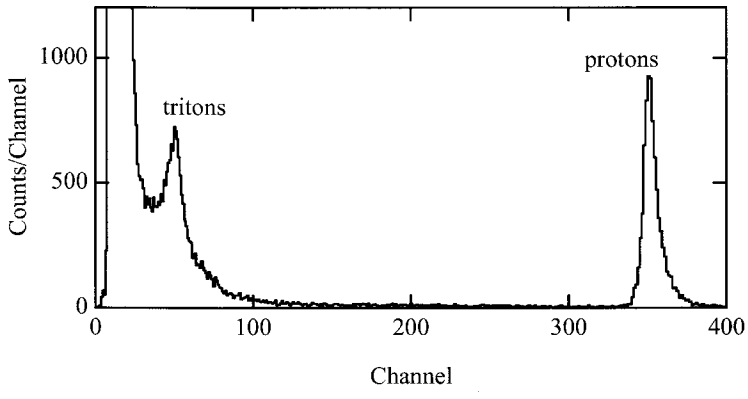

Figure 2.12: A raw spectrum acquired from one of the silicon detectors during D(d,p)T profiling. The tritons and protons are easily identified.

Before stepping through the calculation that converts proton energy to deuteron range in the sample, the differences between path length and range need to be clarified. Fig. 2.14 illustrates the difference of these two terms with the example of deuterium in aluminum using TRIM [2] calculations. The stopping power is the energy loss by a particle over a given distance traveled in the sample. However, as the particle slows down it scatters around causing the total path length traveled to be greater than the actual depth or range in the sample. Thus, integrating the stopping power gives the path length, no the range of the particle in the material. For the following calculations the energy loss of the deuteron and proton over a given range is the value of interest. The stopping power and the energy loss

over a given range differ significantly for the low energy, $0 < E_1 < 200$ keV, deuterons in this experiment. For the high energy protons, these two values are nearly equivalent.

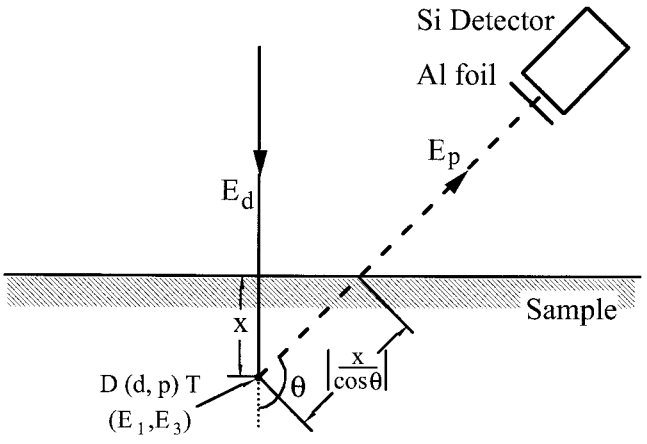

Figure 2.13: A schematic diagram of an incident deuteron, solid line, and the emitted proton, dotted line, resulting from the D(d,p)T nuclear reaction at a depth x in the sample.

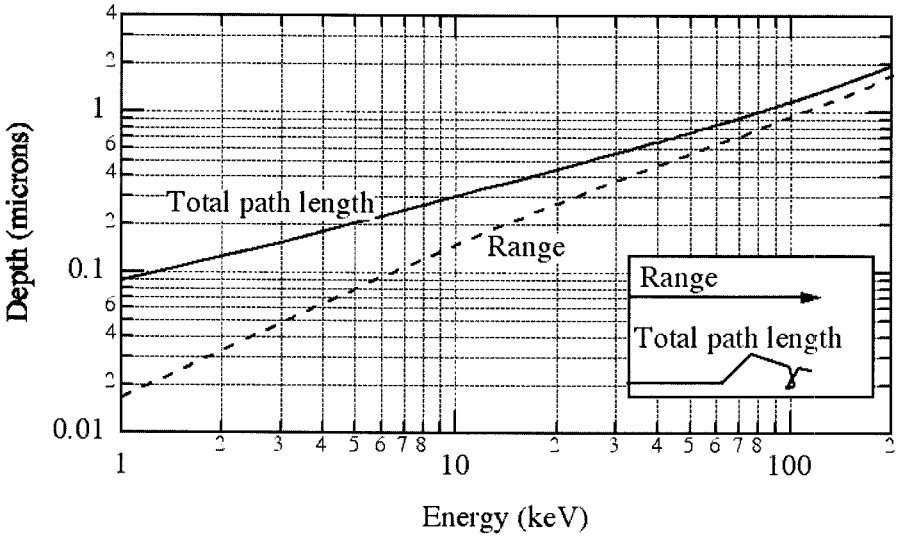

Figure 2.14: The path length and range of deuterium in aluminum calculated with the computer code TRIM [2].

The first step of the analysis is to accurately calculate the energy of the incident deuterons, E_1, at a depth, x, within the sample. The incident deuterons lose energy as they interact with the sample material and come to rest at a depth known as the projected range. This is calculated with the computer code TRIM [2]. At any depth between the sample surface and the projected range of the deuteron, the incident deuteron may interact with a previously implanted deuteron. The probability the a D-D interaction will emit a proton is calculated from the differential cross section. The cross section and asymmetry coefficient for this reaction are described in Ref. 4 and 5, respectively. The proton is emitted with an energy of $2.5 < E_3 < 3.7$ MeV dependent on the energy of the incident deuteron and the angle

of emission, θ, of the proton. This energy is calculated from basic kinematic calculations of momentum and energy conservation. The energy loss with depth and stopping power of the proton in this range of energies are equivalent. Therefore, the energy of the proton upon exiting the sample, E_p, is calculated by integrating the stopping power over the distance $|x/\cos\theta|$ that the proton travels in the sample. Finally, the energy loss of the protons in the aluminum foil is calculated.

The above relationships between energy and depth allow for the calculation of the expected proton yield. The number of protons emitted in the solid angle, Ω, can be calculated for deuterons in the energy range E_1 to $E_1 + \Delta E_1$ and is given by

$$Y(E_1) = \left(\frac{d\sigma_{lab}(\theta)}{d\Omega}\right) I_d \; cn \; \Omega \; \frac{\Delta E_1}{S_d} \qquad (2.1)$$

where $d\sigma/d\Omega$ is the differential cross section for proton production in the laboratory frame, I_d is the incident deuteron fluence, n is the target atom density, c is the deuteron concentration, and S_d is the deuteron stopping power. This equation must be written in terms of the proton energy to be useful for analysis. The number of protons emitted with energies ranging from E_p to $Ep + \Delta E_p$ is calculated by

$$Y(E_p) = \left(\frac{d\sigma_{lab}(\theta)}{d\Omega}\right) I_d \; cn \; \Omega \left(\frac{dE_1}{dE_p}\right) \frac{\Delta E_p}{S_d}. \qquad (2.2)$$

The dE_1/dE_p term is used to convert the deuteron energy to the measured proton energy.

Five preloaded ErD_2 (erbium di-deuteride) samples were bombarded by 200 keV deuterons to a fluence of $2x10^{16}$ D/cm^2 to calibrate the depth profiling calculations. Initially, a theoretical proton spectrum is calculated from Eq. 2.2 assuming the sample is entirely deuterium (c = 1). The proton energy interval, $\Delta E_p \approx 7$ keV/channel, is the energy per channel calibration of the charged particle spectrum obtained from the silicon detector. Both tritons and protons are detected providing two values for use in calculating ΔE_p. The energies of the tritons and protons emitted from a D(d,p)T reaction occurring on the surface of the sample are easily calculated from reaction kinematics and the energy loss through the 0.2 μm aluminum foil. The energy of the incident deuteron with respect to depth in the ErD_2 was calculated using the computer code TRIM [2] and is shown in Fig. 2.15a). The stopping powers of the deuteron and the proton were calculated with TRIM [2] as well.

The measured proton spectrum divided by the theoretical proton spectrum gives the deuterium concentration profile. Fig. 2.16 shows the proton spectra from 200 keV deuterons incident on ErD_2 samples and the resulting deuteron concentration profiles for the five silicon detectors. The channel corresponding to protons emitted from the surface of the sample was chosen by requiring the concentration to be approximately half-maximum at the surface. Ideally, the concentration would be a step function form zero to the deuterium concentration

at the surface channel, however the detector resolution causes broadening of the spectrum. Once the surface channel was determined, it remained unchanged for the analysis of the implanted samples. The dotted lines through the proton spectra in Figs. 2.16 a-e) mark the surface channels for each detector. From Fig. 2.15a) the range of the deuteron in ErD_2 is seen to be 1.1 μm. The resolution of the profiling method is only sufficient to profile to depths of ≈ 0.7 μm, thus calculations beyond that are unreliable. This is clearly seen in the concentration profiles of Fig. 2.16 f-j). Three of the ErD_2 samples were 0.84 μm thick and two of the samples were 12 μm thick. The thickness of these samples is greater than the range of this profiling technique, 0.7 μm: therefore, no difference should be seen in the resulting deuterium profiles.

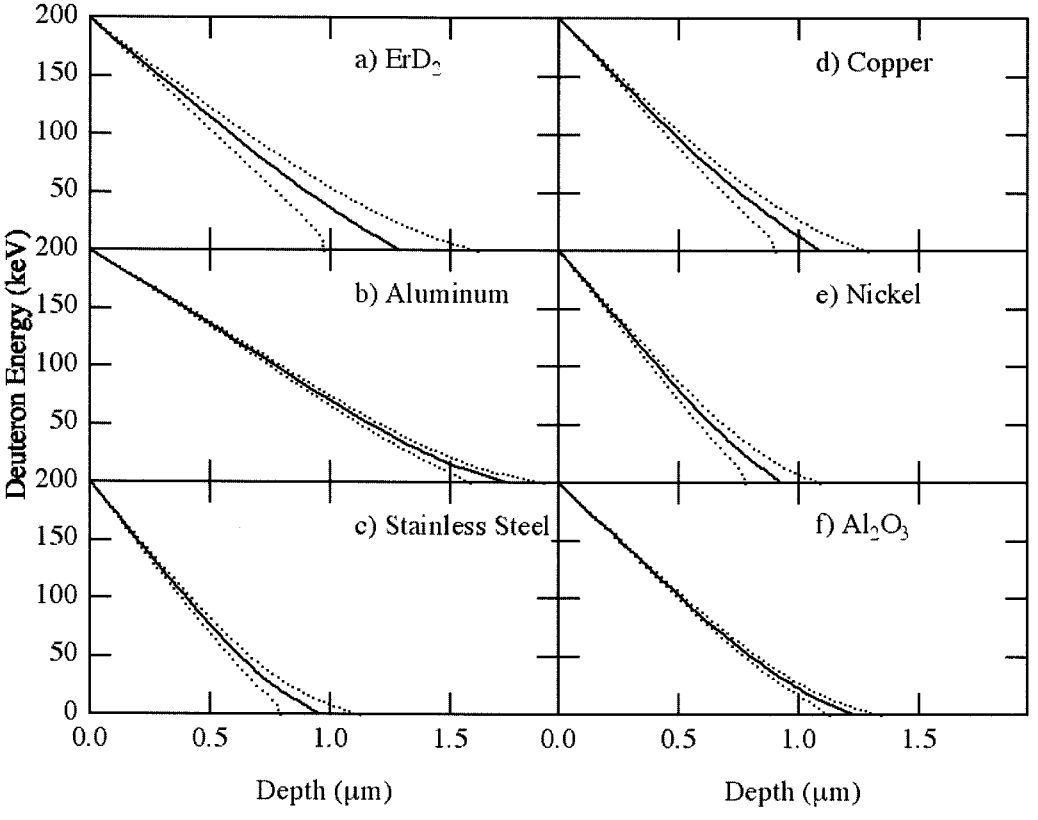

Figure 2.15: The energy versus projected depth of an incident 200 keV deuteron in a) ErD_2, b) aluminum, c) stainless steel, d) copper, and e) nickel, and f) anodized aluminum. The dotted curves indicate the standard deviation of the longitudinal straggling.

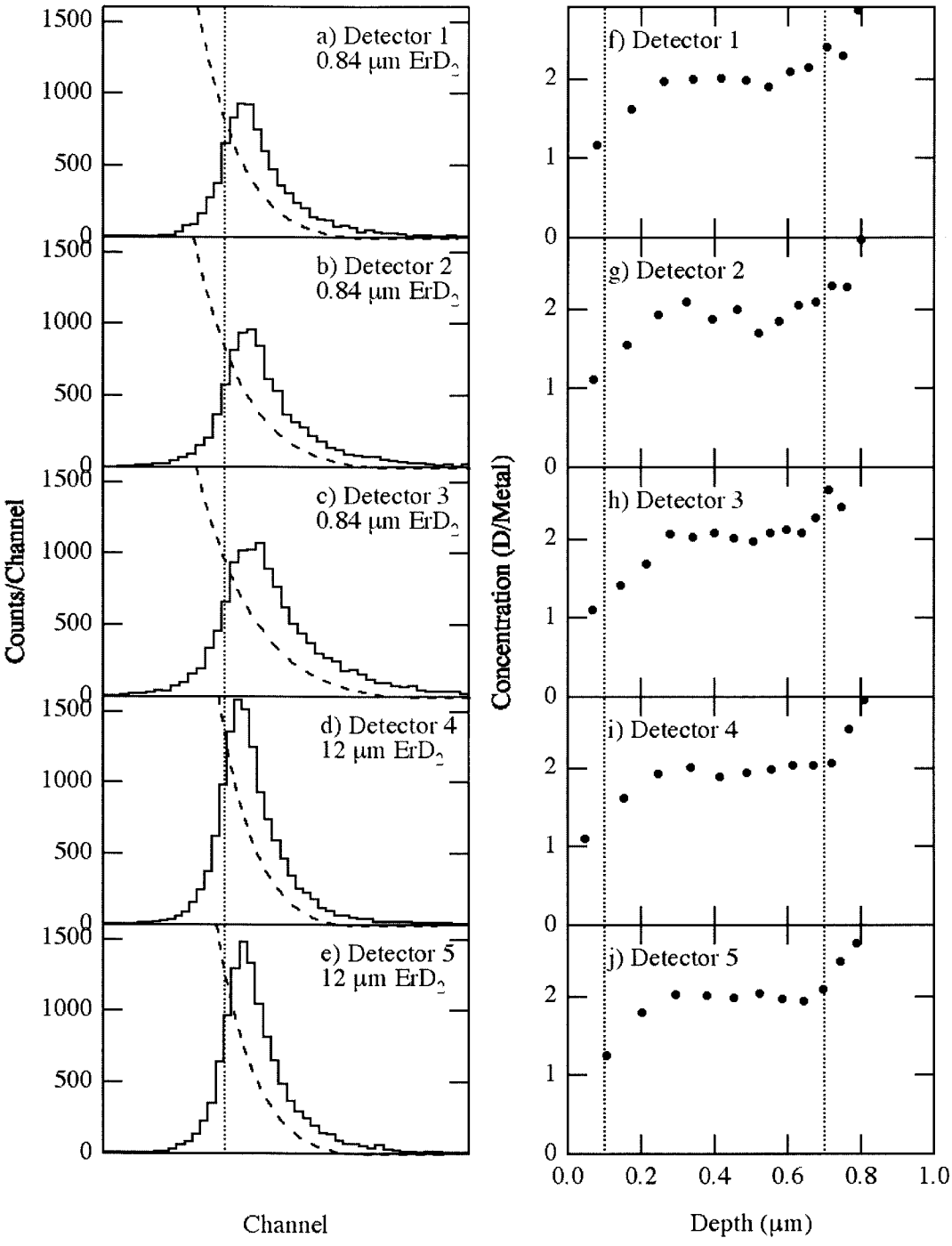

Figure 2.16: a-e) The proton spectra from D(d,p)T profiling obtained from the five silicon detectors. The dotted lines indicate the channel that corresponds to the surface of the sample. f-j) The calculated deuteron concentration with respect to sample depth. The region within the dotted lines is the area in which these measurements are reliable.

The gradual increase in the deuterium concentration from the surface to about 0.2 μm is due to the depth resolution of these measurements. The depth resolution is dependent on three major contributions: the detector resolution, the straggling of the incident deuterons, and the straggling of the outgoing protons. A detailed discussion of the resolution is found in the paper by Cowgill [3]. The three contributions are plotted in Fig. 2.17. For these calculations, the detector resolution includes both the energy straggling of the protons in the 2 μm thick aluminum foil and energy broadening due to the acceptance angle of the detector. The total depth resolution is calculated by adding the three contributions in quadrature.

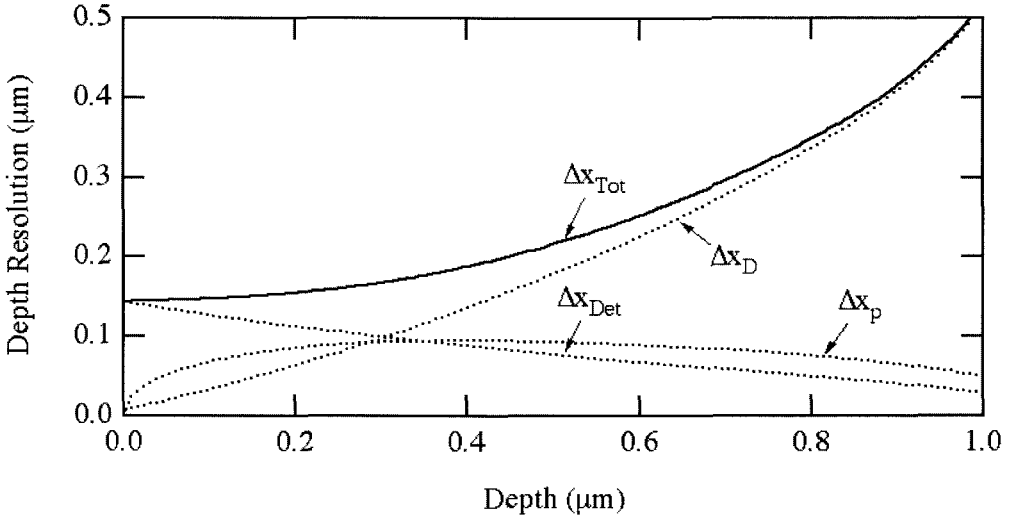

Figure 2.17: The three contributions to the total depth resolution, Δx_{TOT}, from D(d,p)T profiling. The detector resolution, Δx_{Det}; the straggling of the incident deuterons, Δx_D; and the straggling of the outgoing protons, Δx_p, are added in quadrature to give the total depth resolution.

2.4 D(^{3}He,p)^{4}He Nuclear Reaction Profiling

There is a possibility that the deuterium implanted in the samples may permeate through to the back surface of the sample. To measure the permeation, a thin zirconium layer was applied to the back surface of samples implanted during Run 6. Deuterium that migrages into the zirconium layer is trapped and may be measured. The exothermic D(^{3}He,p)^{4}He nuclear reaction was used to measure the deuterium concentration in the zirconium layer. A well-focused ^{3}He beam incident on the zirconium may interact with trapped deuterium and emit a proton. A silicon detector was used to measure the number and energy of the protons emitted. These measured values were then used to calculate the concentration of deuterium that permeated through the sample to the zirconium layer on the back surface.

The water in the cooling system in the APT blanket will probably be slightly acidic to reduce corrosion. The acidity of the water would also reduce the oxide layer on the outer surface of the ^{3}He tubes and, therefore, promote the recombination of tritium into the water. Thus, an oxide free interface between the sample and the Zr layer is comparable to the interface the ^{3}He tubes will have with the cooling water in the APT blanket.

2.4.1 D(^{3}He,p)^{4}He Experimental Equipment

A schematic diagram of the experimental setup used for the nuclear reaction profiling of a single sample is shown in Fig. 2.18. A 650 keV ^{3}He beam is incident normal to the sample. An annular silicon detector located at 180° with respect to the beam detects the scattered protons. The area of the detector is 200 mm^2 with a 4 mm diameter opening where the ^{3}He beam passes through. The detector is shielded on the upstream side by an aluminum aperture held at –200 V to suppress scattered electrons and on the downstream side by a 2 μm thick aluminum foil to prevent low energy backscattered particles from entering the detector. The detector subtends a solid angle of 0.0187 sr. This is calculated from the geometry of the experimental setup and was confirmed using an ^{241}Am alpha source. The energy signals from the silicon detector and the integrated current were recorded using LabVIEW.

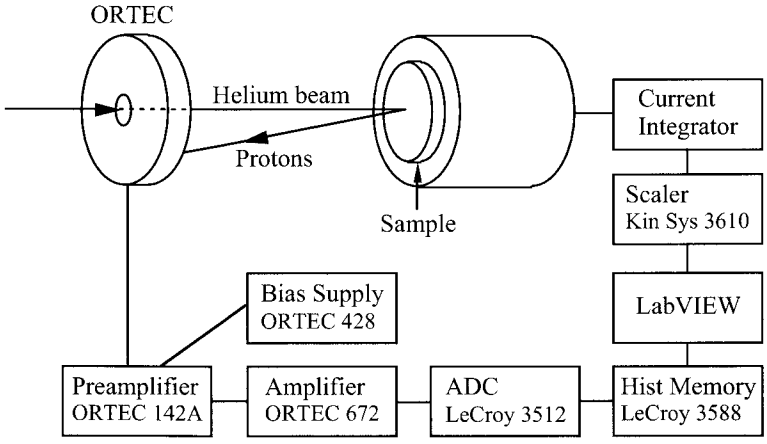

Figure 2.18: A diagram of the experimental setup used for the D(^{3}He,p)^{4}He nuclear reaction profiling during Run 6.

2.4.2 D(^{3}He,p)^{4}He Experimental Procedure

The D(^{3}He,p)^{4}He profiling analysis procedure is the same as that of the D(d,p)T profiling analysis. The differences are in the interaction of the incident ^{3}He with the sample, the D(^{3}He,p)^{4}He reaction, and the outgoing energy of the protons. The energy of the incident ^{3}He ions, $0 < E_1 < 650$ keV, result in protons emitted with energies of $12.78 < E_3 < 17.11$ MeV. The cross section of the D(^{3}He,p)^{4}He reaction was taken from measurements by Moller and Besenbacher [6]. The stopping powers and ranges were calculated using TRIM [2]. Fig. 2.19 shows the energy of the incident ^{3}He ion with respect to the depth in the sample. A 1.39 μm thick ErD_2 sample was used to calibrate the depth profiling calculations. A typical spectrum for the calibration is shown in Fig. 2.20. The range of the ^{3}He in the ErD_2 is about 1.5 μm, however the profiling is only accurate to about 1.0 μm as seen in Fig. 2.20. The gradual increase in the deuterium concentration from the surface to 0.1 μm is due to the depth resolution of these measurements, therefore the useful

range is from 0.1 to 1.0 μm. Comparing Fig. 2.20b) to Figs. 2.16f-j) one can easily see that the depth resolution for the ^{3}He profiling is significantly better than for the D profiling under these experimental conditions. The calculated contributions to the depth resolution are shown in Fig. 2.21. A comparison of this figure to Fig. 2.17 reinforces the improved resolution that the ^{3}He profiling provides.

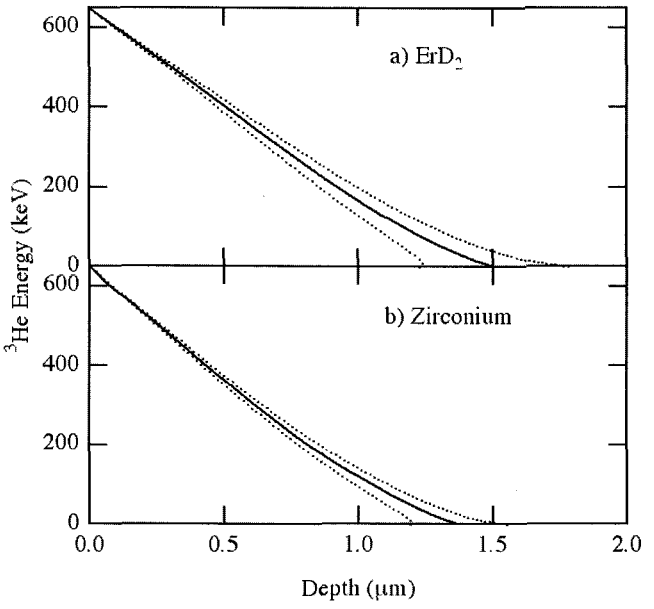

Figure 2.19: The energy versus projected depth of the ^{3}He in a) ErD_2 and b) Zr. The dotted curves indicate the standard deviation of the longitudinal straggling.

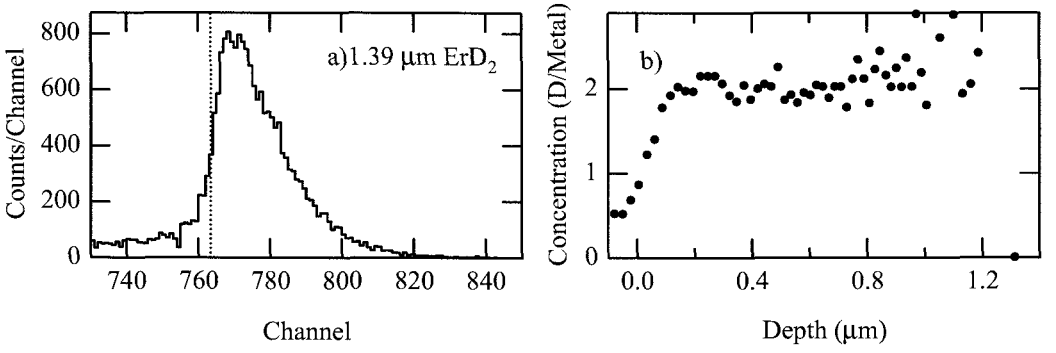

Figure 2.20: The proton spectra obtained from the silicon detector and the calculated deuteron concentration with respect to sample depth from D(^{3}He,p)^{4}He profiling. The dotted line in a) indicates the surface channel of the profile.

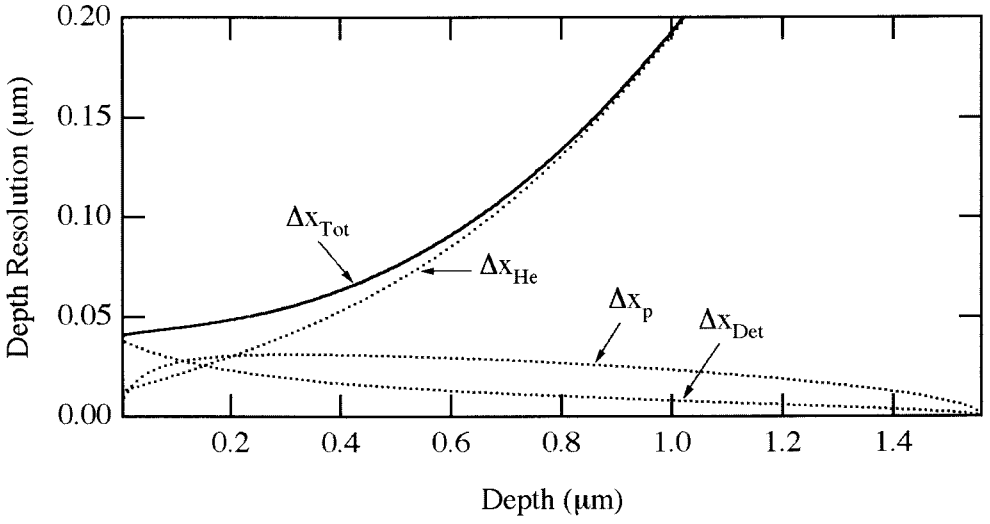

Figure 2.21: The three contributions to the total depth resolution, Δx_{Tot}, for the $D(^3He,p)^4He$ profiling. The detector resolution, Δx_{Det}; the straggling of the incident helium, Δx_{He}; and the straggling of the outgoing protons, Δx_p, are added in quadrature to give the total depth resolution.

3 Modeling and Sample Properties

The objective of the implantation experiments is to determine the behavior of deuterium in the reference materials for APT tubes under conditions closely resembling those expected for APT operation. This information can then be used to predict the behavior of tritium in the materials under APT conditions. There are four main factors that determine the steady-state concentration profile of deuterium in the sample: the diffusion of deuterium within the metal, the solubility of deuterium within the metal, the recombination rate of the deuterium at the inner and outer surfaces of the metal, and trapping and bubble formation of deuterium in the metal.

3.1 Modeling

3.1.1 Bare Samples

A simple model can be used to describe the steady-state deuterium concentration in the accelerator samples. The implanted deuterium will migrate through the sample from areas of high concentration to those of low concentration based on the following simplified equation:

$$\frac{dc}{dt} = D\nabla^2 + \text{source} \qquad (3.1)$$

where c is the concentration of deuterium and D is the diffusivity. This equation is constrained by boundary conditions; two cases will be discussed. The first case occurs when the surface of a material is exposed to a fixed pressure of deuterium gas. If the gas transfer at the surface is not impeded, the deuterium concentration in the sample is given by the solubility of deuterium in the material times the square root of the gas pressure. The second case occurs if there is release of deuterium from the surface, and if the release rate is limited by the rate at which deuterium atoms are able to recombine into molecules. This situation can occur if there is a constant source of deuterium entering the system, such as implantation. A diagram of the concentration profile for the steady-state solution of the second case is shown in Fig. 3.1. The deuterium is implanted at a given depth, x = R. The concentration of deuterium in solution linearly decreases from R to both the inside surface at x = 0 and the outside surface at x = L. At steady-state (in the absence of trapping or bubble formation) the incident flux, J, must equal the sum of the flux recycled to the inner surface, J_r, and the flux permeating through to the outside surface, J_p.

$$J = J_p + J_r \qquad (3.2)$$

Recombination is the rate limiting process for the release of deuterium from most materials. This recombination is a second order process with the release rate defined as the product of the recombination rate coefficient times the square of the concentration of deuterium at the surface:

$$J_r = k_o c_o^2 \tag{3.3}$$

$$J_p = k_L c_L^2 \tag{3.4}$$

where k_o and k_L are the recombination coefficients for deuterium at the inside and outside surfaces, respectively; and c_o and c_L are the deuterium concentrations at the inside and outside surfaces. In APT, the outside wall of the tubes will be in contact with water. The water chemistry will determine the recombination coefficient of the outside surface.

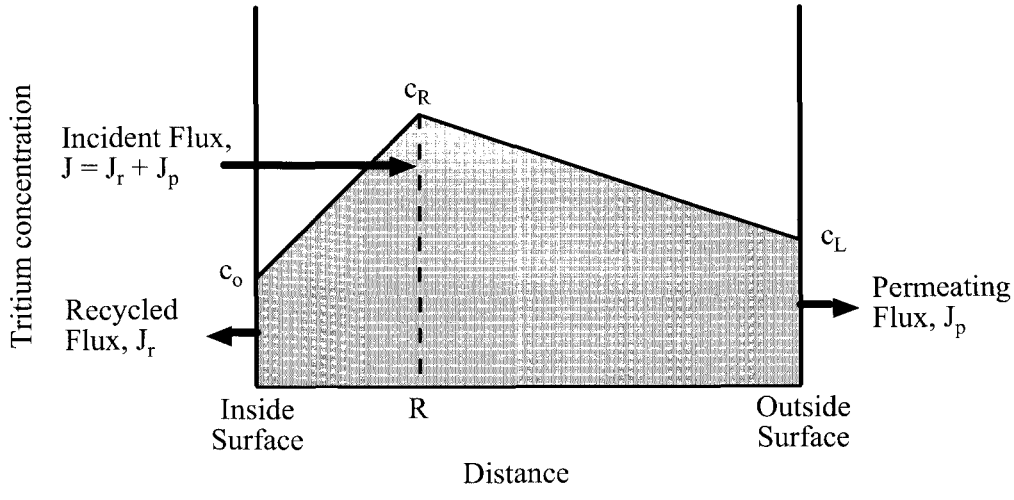

Figure 3.1: A diagram of the model of the steady-state deuterium concentration profile through the tube wall.

3.1.2 Bubbles and Trapping

A more complete discussion of steady-state deuterium concentrations should include the precipitation of deuterium bubbles and trapping. The tritium produced in APT is recoil injected into the walls of the metal tubes. The direct implantation of deuterium into a metal during the accelerator experiments simulates this process by allowing a high concentration of deuterium to develop in the implant region dependent on the incident flux and diffusivity of the deuterium. If the deuterium concentration exceeds the solubility limit of the metal, bubbles of deuterium may form within the metal. A diagram of the concentration profile for the steady-state solution with bubbles is shown in Fig. 3.2. The concentration of deuterium above the solubility limit will precipitate into bubbles. The concentration of deuterium trapped in the bubbles is dependent on the depth of the bubbles from the surface. When the

bubbles are precipitated, an upper limit to the mobile concentration of deuterium is reached and the trapped concentration of deuterium is increased. Bubbles are not expected to form in stainless steel and nickel under APT conditions due to their high deuterium solubility. However, the deuterium fluxes obtained in APT will cause bubbles to form in the aluminum. The solubility of deuterium in copper is in a region where the formation of bubbles under APT conditions is questionable.

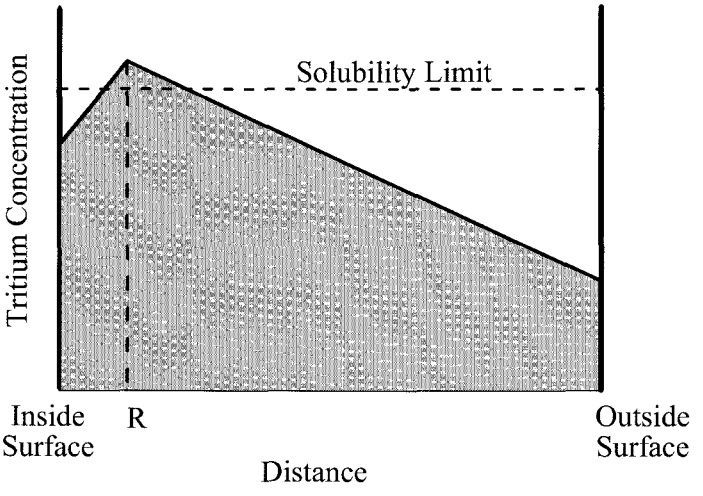

Figure 3.2: A diagram of the model of the steady-state deuterium concentration profile through the tube wall when bubbles are precipitated.

If bubbles do not form, deuterium trapping in ion damaged metals is dominated by vacancies and other defects. Thermal desorption spectroscopy (TDS) of the irradiated samples may be used to determine the amount and type of trapping. The computer code DIFFUSE [7] is a finite difference computer code that computes the trapped and mobile concentrations of deuterium in a material based on the parameters for the diffusivity, solubility, recombination rate coefficient, and trapping input into the code. If the diffusivity, solubility, and recombination rate coefficient are known, the trapping parameters may be varied until agreement between the code calculations and the experimental data is achieved. In this way, information on the deuterium trapping in the APT test samples can be determined. This technique was used with data from the implant experiments.

3.1.3 Coated Samples

A thin coating was applied to the aluminum and stainless steel samples in an attempt to lower the deuterium retention and permeation. The model used to describe the deuterium concentrations in the coated samples is the same as that used for the bare samples with the addition of an interface between the coating and the substrate at $x = F$. A diagram of the concentration profile for the steady-state solution of a coated sample is compared to an uncoated sample in Fig. 3.3. If the coating material has a higher recombination rate coefficient than the bulk material, the recombination rate is increased, lowering the deuterium concentration at the surface and in the bulk. At the interface between the coating and the substrate there is a discontinuity in deuterium concentration based on the ratio of the

solubility of deuterium in the substrate to the solubility of deuterium in the coating. A coating with higher deuterium solubility than that of the substrate material will help reduce the permeation. Therefore, we are looking for a material that does not form a stable oxide, has a high recombination rate coefficient, and has relatively high tritium diffusivity and solubility. Both copper and nickel are good candidates.

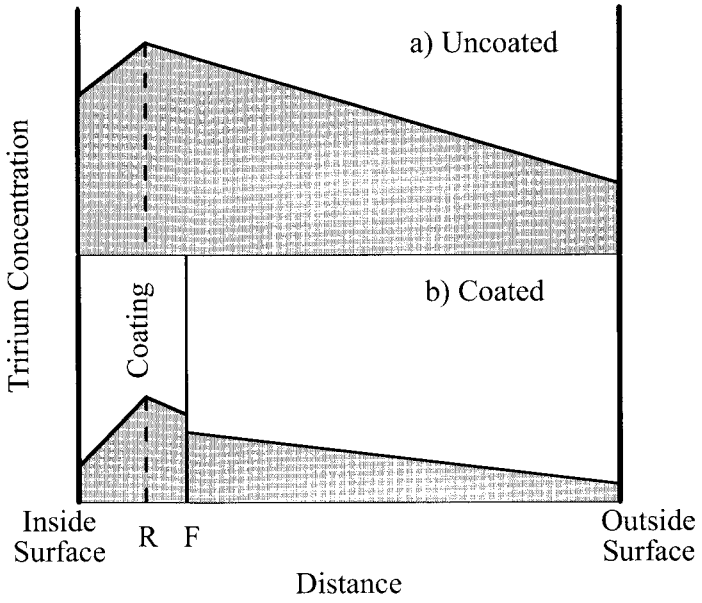

Figure 3.3: A diagram of the steady-state deuterium concentration profile through a) an uncoated tube wall and b) a coated tube wall.

3.2 Sample Properties

The description given above for the migration of deuterium through the samples is highly dependent on the properties of the metal and the experimental conditions. The diffusivity, solubility and recombination rate of hydrogen isotopes in the various metals will be discussed. Bubble formation and trapping will also be discussed.

3.2.1 Diffusivity

When the implanted deuterium ions come to rest in the metal they may start diffusing back towards the metal surface or into the bulk. Diffusion is most simply described using a random walk model of deuterium migrating away from areas of high concentration toward areas of low concentration. The diffusion of deuterium obeys the Arrhenius relation:

$$D = D_o \exp\left[\frac{-E_D}{kT}\right] \tag{3.5}$$

where D_o is the diffusion coefficient, E_D is the activation energy of diffusion, k is the Boltzmann constant and T is the temperature. Measured values for these two constants are listed in Table 3.1 and graphed in Fig. 3.4.

Table 3.1: Experimentally determined values of the diffusion coefficients. The table includes the hydrogen isotope, the temperature range, and the method used for the measurement. The coefficients listed in bold type were used in calculations in this work.

Sample	Isotope	D_o (cm^2/s)	E_D (eV)	Temperature (K)	Method	Ref.
99.5 % Al	H	0.21	0.47	743-863	Outgassing	9
Pure Al	H	0.11	0.43	633-873		12
99.5 % Al	T	0.002	0.44	338-472	Recoil-Injected	13
99.5 % Al	T	0.009	0.54	423-796	Thermally-doped	13
99.999 % Al	D	0.014	0.37	473-873	Permeation	14
Al (see text)	**H**	**0.92**	**0.57**	**285-328**	**Electrolytic**	**8**
99.999 % Cu	D	0.00082	0.24	500-1000	Permeation	14
99.999 % Cu	D	0.0073	0.38	723-1073	Outgassing	15
Pure Cu	**H**	**0.011**	**0.40**	**543-923**	**Outgassing**	**9**
99.999 % Ni	D	0.0039	0.40	500-1000	Permeation	14
99.999 % Ni	D	0.0053	0.40	723-1273	Outgassing	15
99.998 % Ni	D	0.00318	0.40	220-340	Electrical Resistivity	16
99.98 % Ni	**H**	**0.0040**	**0.41**	**297-673**	**Permeation**	**10**
316 SS	H	0.0073	0.54	502-863	Pressure modulation	17
304 SS	D	0.00035	0.44	650-1050	Permeation	18
316 SS	D	0.00017	0.41	540-680	Permeation	19
304, 304L SS	D	0.0066	0.52	812-1190	Permeation	20
SS (see text)	**D**	**0.0047**	**0.56**	**400-700**		**11**

The diffusion coefficients listed in bold type in Table 3.1 were used in calculations in this work. The primary reason for using these values is that they were measured in temperature ranges close to those of interest to APT. Ishikawa and McLellan [8] measured the diffusivity of hydrogen in 25 μm thick aluminum films with 50 ppm impurities. These authors were careful to exclude oxide and trapping effects. They used an electrolytic method at temperatures where vacancy concentrations are essentially zero. They were also able to show that their data extrapolated nicely to the values determined by the other groups at higher temperatures. For the temperature range of 285 to 328 K, they determined the diffusivity of hydrogen in aluminum to be, $D = 0.92 \exp(-0.57\ eV/kT)\ cm^2/s$. No measurements for the diffusivity of hydrogen in copper in the temperature range of interest to APT were found in the literature. The diffusion coefficient for hydrogen in pure copper was measured by Eichenauer and Pebbler [9] between 543 K and 923 K by degassing. They found the diffusivity for copper to be $D = 0.011 \exp(-0.40\ eV/kT)\ cm^2/s$. Robertson [10] measured the diffusivity of hydrogen in 99.98 % pure nickel at temperatures between 297 K and 673 K by permeation methods. From a comparison of his own results with results found

in the literature, he concluded that the diffusivity is independent of grain size and dislocation structure. He determined the diffusivity to be, $D = 0.0040 \exp(-0.41 \text{ eV/kT}) \text{ cm}^2/\text{s}$. The diffusivity of deuterium in stainless steel was measured by analyzing the time and temperature dependence of deuterium flux through various stainless steel foils by Louthan and Derrick [11]. The diffusivity was found to be $D = 0.0047 \exp(-0.56 \text{ eV/kT}) \text{ cm}^2/\text{s}$ at temperatures between 400 and 700 K and insensitive to alloy composition. The alloy stested included 304N, 304L, 310, 309S, 21-6-9, and A-216. Care was taken in these experiments to minimize surface effects.

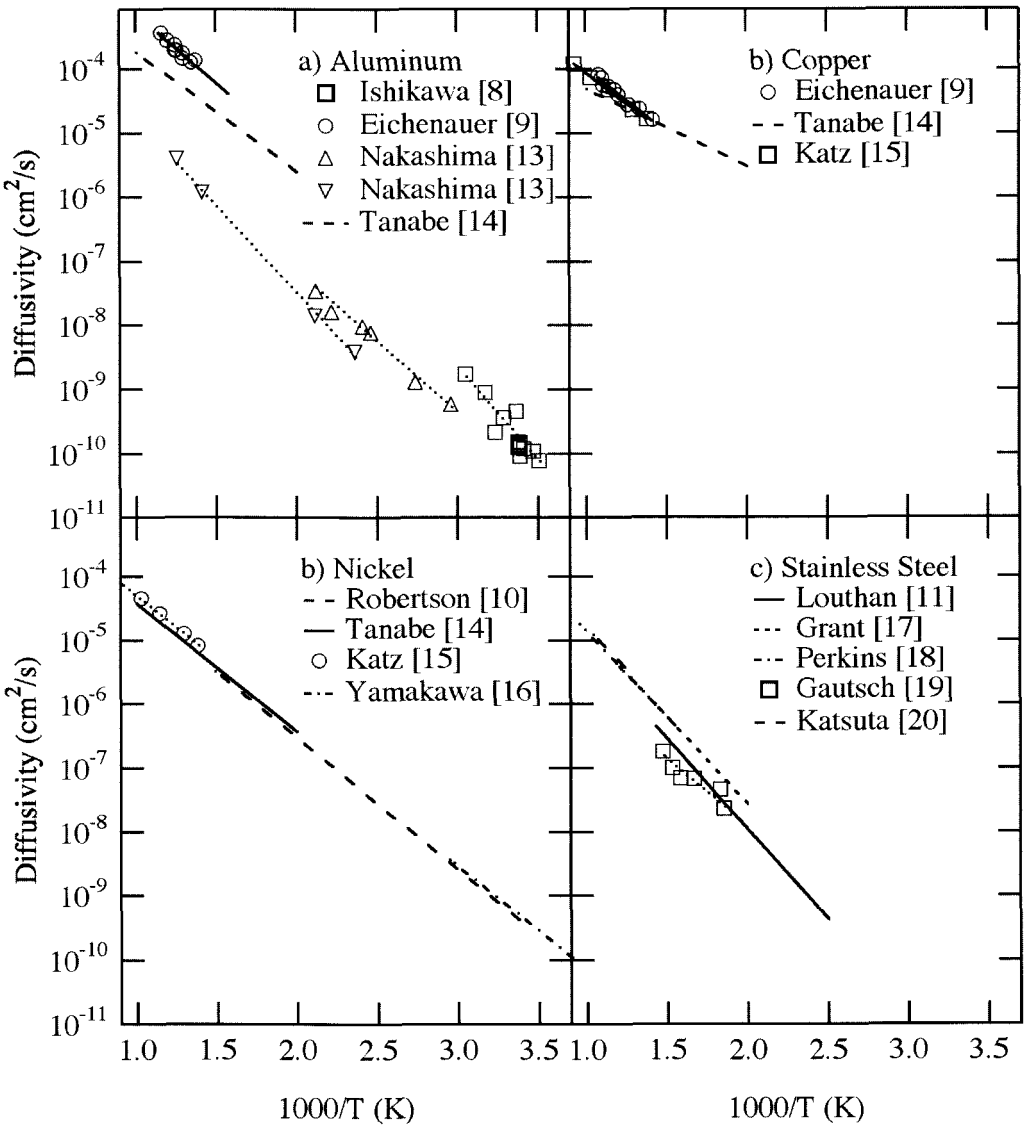

Figure 3.4: Measured diffusivity for a) aluminum, b) copper, c) nickel and d) stainless steel. The references are labeled in Table 3.1.

3.2.2 Solubility

Al, SS, Cu and Ni are all endothermic absorbers. The solubility of hydrogen isotopes in endothermic metals, unlike exothermic metals, increases with increasing temperature. At equilibrium and in low concentrations the solubility of hydrogen gas in solids is dependent on the square root of the pressure as described by Sievert's law:

$$S = S_o \exp\left[\frac{-E_S}{kT}\right]\sqrt{p} \tag{3.6}$$

where S_o is the solubility coefficient, E_S is the heat of solution and p is the pressure. Measured values of S_o and E_S are listed in Table 3.2. Eichenauer et al [9, 12, 21] calculated the solubility of hydrogen in pure aluminum, copper, and nickel from measurements of the diffusivity. The solubility of hydrogen in 304 and 304L stainless steel was measured by Katsuta and Furukawa [20] using the permeation time-lag method.

Fig. 3.5 is a plot of the solubility of hydrogen in the various metals versus the hydrogen gas pressure at 353 K. The curves are terminated at the metal's yield strength. When the concentration of hydrogen gas exceeds the limit of solubility, the recombination of atoms to form molecules of hydrogen at defects in the metal may force the metal to yield with the formation of bubbles. Significantly larger quantities of hydrogen can be trapped in bubbles, H/Metal = 0.1, than in solution.

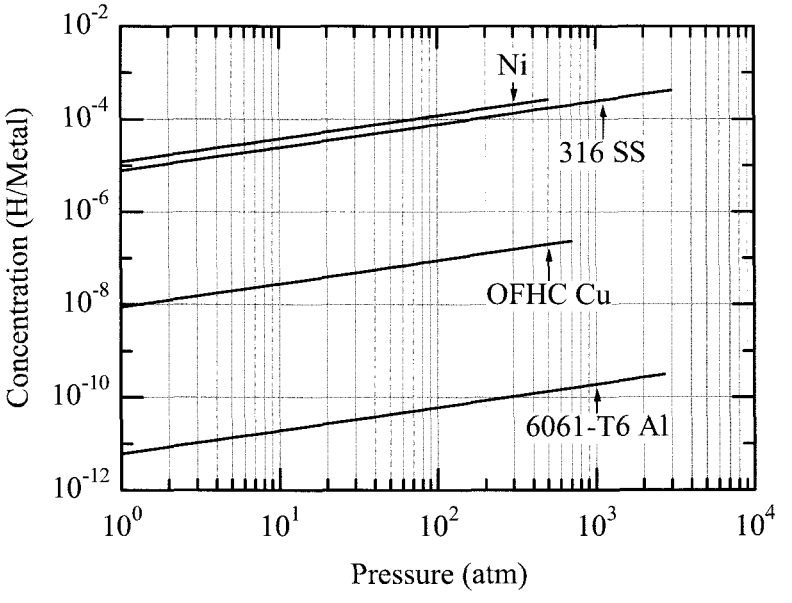

Figure 3.5: The solubility of hydrogen in aluminum, stainless steel, copper, and nickel calculated at 353 K. The curves follow Sievert's law and are terminated at the yield strength of the metals.

Table 3.2: Experimentally determined values of the solubility of hydrogen in the sample materials. Katsuta and Furukawa [20] determined the solubility for stainless steel and Eichenauer et al [9,12,21] determined the solubility for Al, Cu, and Ni.

Material	S_o (H/Metal- $atm^{-1/2}$)	E_S (eV)	Reference
Pure Al	2.20×10^{-3}	0.60	12
304, 304L SS	1.03×10^{-3}	0.15	20
Pure Cu	1.68×10^{-3}	0.37	9
Pure Ni	1.64×10^{-3}	0.15	21

3.2.3 Recombination Rate Coefficient

Recombination rate coefficients are highly affected by surface conditions and impurities (especially oxides). Therefore, it is necessary that the experiments be performed at conditions closely resembling those of the actual application if they are to be relevant. For a tritium atom implanted in a material to be re-emitted back in the same direction from which it came, it is necessary for this atom to migrate back to the surface and then recombine with another tritium atom. This reemission process is defined by the equation:

$$\text{Release Rate} = k_R c^2 \tag{3.7}$$

where k_R is the recombination rate coefficient and c is the volumetric tritium concentration immediately below the surface. The recombination rate coefficient is dependent on temperature in the following manner:

$$k_r = k_{ro} \exp\left[\frac{-E_k}{kT}\right] \tag{3.8}$$

Recombination rate coefficients have been studied for many years, and formulas have been derived that are correct for clean metal surfaces. It is when oxides or other impurities are added to the surface that the formulas become less useful. In all cases, the addition of impurities decreases the recombination rate coefficient. On a clean metal surface, each surface atom serves as a recombination site (effectively serving as a catalyst). The addition of impurities covers these sites. Some impurities are more effective than others at this site removal process, and oxygen is one of the most effective.

For a material such as aluminum, the oxygen further complicates the release process. Not only is the oxygen blocking the metal recombination sites, but the oxide layer also serves as a permeation barrier making it difficult for tritium in the bulk to get to the surface where it may recombine and release. It is typical in implantation studies for the effect of the retarded migration back to the surface to be lumped together with the recombination process. The same formula as Eq. 3.7 is used with the k_R being an effective value for the entire process.

Recombination rate coefficients have been measured for Al, Cu, Ni and SS. Yamaguchi et al [22] performed measurements and compared their data to data collected from other authors for these materials in Fig. 3.6. Two different research groups have measured the recombination rate coefficient for hydrogen in aluminum. Kamada et al [23] used elastic recoil detection (ERD) in 1984 to determine the recombination rate coefficient for hydrogen in aluminum. In their experiments, 25 and 50 keV H_2^+ implantation was used to inject hydrogen at a rate of $3x10^{13}$ H/cm^2-s into 99.999 % pure Al and Al alloy (3 % Mg, 2.3 % Li, and 0.2 % Zr). From measurements of the total retention, the authors were able to determine the rate of release of hydrogen from the surface as a function of temperature and time. Then, using the near surface hydrogen concentration as the driving force for the recombination, they were able to determine the recombination rate coefficient for the aluminum. For APT relevant temperatures, 323 K<T<373 K, the recombination rate coefficient for hydrogen in pure aluminum is approximately 10^{-28} cm^4/s. Another point made by the authors is that hydrogen trapped in defects begins to become mobile at temperatures above about 343 K. This is in the middle of the APT relevant temperature range.

In 1992, Hayashi et al [24] determined the recombination rate coefficient for deuterium implanted into 99.999 % pure aluminum. The samples were polished before use. This significantly reduces the oxide layer, but because the sample is exposed to air a thin oxide layer will still be present. No removal of the oxide layer was attempted after the sample was put in the vacuum before implantation. After a series of pre-implantations over several days, they were able to get reproducible data on the reemission of deuterium from the front surface. From this data they determined the effective recombination rate coefficient to be approximately 10^{-14} cm^4/s at 500 K. The particle flux during the measurements was $1x10^{15}$ D/cm^2-s, much higher than that expected for APT. Because the higher implantation flux continuously "stirs" the oxide layer on the surface, it is doubtful that this data is relevant to APT. The difference between the values of the recombination rate coefficients measured by Kamada et al and Hayashi et al is fourteen orders of magnitude. It is obvious that new measurements need to be performed where the conditions duplicate as closely as possible those that will exist for APT.

It is not possible to pick out a preferred value for the recombination rate coefficient for hydrogen in aluminum. The factor that most greatly affects the effective value is the oxide layer on the surface. The rate of implantation has an affect to a lesser degree. The conclusion is that the recombination rate coefficient must be measured under the conditions that are expected for the actual application intended for the aluminum. It is very likely for the APT application that the recombination rate coefficient for bare aluminum is going to be quite low due to the low temperature, low particle flux, and relatively high oxygen potential that will be present.

Wilson et al [25] implanted 10 keV D_3^+ deuterons at a flux of $1x10^{16}$ D/cm^2-s to a fluence of $1x10^{19}$ D/cm^2 at room temperature into Marz-grade copper. The recombination rate coefficient was measured to be a constant $6.7x10^{-18}$ cm^4/s over the temperature range 575-825 K. They found that carbon appears to have little effect on deuterium permeation compared to other impurities such as oxygen.

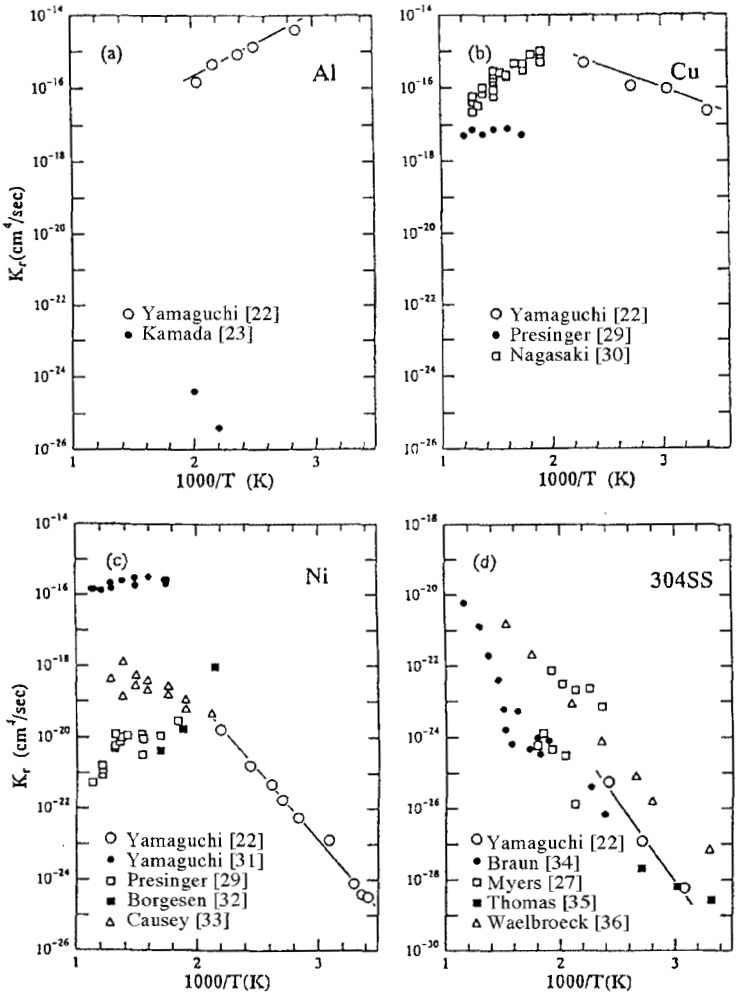

Figure 3.6: Measured recombination rate coefficients for a) aluminum, b) copper, c) nickel and d) 304 SS.

Besenbacher et al [26] determined the recombination coefficient for Marz-grade, single-crystal nickel of 99.995 % purity to be at least 10^{-19} cm^4/s at 350 K. The nickel surface was electropolished and exposed to air before the measurements were made.

Myers and Wampler [27] implanted 25 μm thick 304 SS samples with $4x10^{16}$ atoms/cm^2 of 15 keV ^4He and $2x10^{16}$ atoms/cm^2 of 15 keV deuterons. Before implantation, the foils were electropolished and exposed to air. One of the samples was sputtered with 30 keV Fe ions to remove the oxide layer. After implantation the samples were ramped to around 425–575 K and held there. The deuterium in the near surface region was measured with 700 keV ^3He ions over time. Recombination rates of $(9.6x10^{-20}$ $cm^4/s)exp(-0.34eV/kT)$ and $(1.3x10^{-17}$ $cm^4/s)exp(-0.81eV/kT)$ were found for the sputtered and oxide surfaces, respectively.

Causey et al [28] found that the recombination rate coefficients of $7x10^{-24}$ and $1.6x10^{-21}$ cm^4/s on 304 SS are dependent on the surface cleanliness. Surface contaminates

were found to inhibit molecular recombination. They also associated a lowering of the permeation rate with the cleaning of the upstream surface due to the ion bombardment.

The recombination rate coefficients used in DIFFUSE calculations are listed in Table 3.3. The references these values were obtained from are listed in the table.

Table 3.3: Recombination coefficients used in DIFFUSE calculations. The temperature range in which the coefficient was obtained is listed as well as the references.

Material	k_r (cm^4/s)	Measured Temperature Range (K)	Reference
Pure Al	$1x10^{-28}$	343 - 493	12
304 SS	$3x10^{-30}$	425 - 575	27
Pure Cu	$7x10^{-18}$	575 - 825	9
99.995 % Ni	$1x10^{-20}$	350	26

Table 3.4: Measured trap energies, E_T, for Al, Cu, Ni and SS. The experimentally determined type of trap is listed.

Sample	E_T (eV)	Trap Type	Ref.
99.999 % Al	0.52	vacancies	39,40
	0.71	bubbles	
	1.2	O-D bonding	
Marz-grade Cu	0.22	self-interstitials	41
	0.42	monovacancies and vacancy clusters	
99.995 % Ni	0.24	single vacancy	26
	0.43	multiple-vacancy	
316 SS	0.3	radiation damage	47

3.2.4 Bubbles and Traps

Retention of deuterium in the samples is partially due to trapping at defects or to bubble formation. Defects throughout the bulk may exist as well as defects created by radiation damage. The manner in which deuterium is trapped in various metals has been studied extensively. The traps found in Al, Cu, Ni and SS are listed in Table 3.4. The energy required for deuterium to move from a trap site to a nearby lattice site is the sum of the diffusivity activation energy, E_D, and the true trap energy, E_T. The trap energy listed in Table 3.4 and discussed in the text is the true trap energy, E_T, unless noted otherwise.

Extensive work has been completed on the characteristics of traps and is discussed in the following paragraphs. Wilson and Haggmark [37] examined the trapping of deuterium in Marz-grade aluminum at lower temperatures. They found deuterium to be trapped in aluminum at two different activation sites. The majority of the trapping was at a site with an activation energy of about 1.3 eV. A second energy site was found at 2.0 eV, but the

concentration of this site was much smaller. The trap energy reported here is the energy required to get deuterium to move from a trap site to a nearby lattice site, $E_D + E_T$. Using the 0.57 eV activation energy determined by Ishikawa and McLellan [8], the true trap energies are closer to 0.8 and 1.4 eV.

In 1981, Kido et al [38] studied the defect trapping of deuterium implanted in single-crystal and polycrystal aluminum of 99.99 % purity. They used nuclear reaction profiling to examine the movement of deuterium in the material during anneals after the implantation. The aluminum was irradiated with 680 keV D_2^+ ions to fluences of 1 to $3x10^{16}$ D^+/cm^2 at temperatures below 180 K. When the implantation profile was seen to change only slightly during three days at room temperature, they concluded that the deuterium was trapped at defects created during the implantation. They concluded that the diffusivity of deuterium in aluminum is approximately 10^{-3} to 10^{-4} cm^2/s at room temperature. After these findings, the authors then examined the deuterium profiles after heating to 358, 443, and 533 K for 30 minutes. At each higher temperature anneal, the maximum concentration was seen to continuously decrease, but the shape of the concentration profile did not change. It was concluded from this information that the probability of release from the trap zone increased as the temperature was increased, and that all deuterium released from this zone rapidly migrated away. Final analysis of the data suggested that the probability of being released from the trap site is proportional to $\exp(-E_T/kT)$ where E_T is 0.12 eV.

By far, the most comprehensive study of trapping of deuterium in aluminum was reported by Myers et al [39] in 1985. This group used nuclear reaction profiling to examine the migration of deuterium away from and near the oxide layer in 99.999 % pure aluminum. They found the activation energy of the monovacancy to be 0.52 eV. When the oxide layer was removed from the samples, the deuterium was seen to migrate at about 350 K either out of the sample or to a depth in the sample below that at which it could be seen by the ^3He analysis beam. When the oxide layer was left on the sample, the deuterium remained in the near surface region until the temperature reached about 450 to 500 K. These authors were able to show that this delayed migration was due to the formation of deuterium bubbles at the oxide layer interface. The effective activation energy of this trap was reported to be 0.71 eV. In a subsequent paper, Myers and Follstaedt [40] found that another trap could be generated in 99.999 % pure aluminum if implantation was present. The activation energy of this trap was 1.2 eV. This trap was believed to be due to the O-D trapping at oxide inclusions and at the metal-oxide interface at the surface. The density of the lowest energy trap was reported to be close to the initial density of the implanted particles. The two higher energy traps occur only at oxides (inclusions and the interface), and have a relatively low density.

Two groups determined trap energies for deuterium in copper. Besenbacher, Nielsen and Myers [41] investigated the effects of defect trapping on the migration of deuterium in Marz-grade single-crystal copper. Two traps were found: a 0.22 eV trap associated with self-interstitials and a 0.42 eV trap associated with monovacancies and small vacancy clusters. These energies result in deuterium release from implanted copper occurring at 250 and 300 K, again showing relatively rapid migration at APT temperatures. Wilson et al [25] implanted 10 keV D_3^+ deuterons at a flux of $1x10^{16}$ D/cm^2-s to a fluence of $1x10^{19}$ D/cm^2 at room temperature into Marz-grade copper. Two traps were found in the near surface region at 0.6 and 0.9 eV ($E_D + E_T$). The 0.9 eV trap may be due to deuterium trapped in bubbles

whereas the 0.6 eV trap may be due to deuterium-vacancy traps. The traps were measured using thermal desorption spectroscopy.

Fukui et al [42] bombarded 99.999 % pure copper with 0.2–8 keV hydrogen ions at fluxes of $1–10x10^{14}$ H/cm^2-s at temperatures between 303 and 573 K. The implantations were done in a transmission electron microscope to study the microstructural evolution of the samples. At 303 K interstitial type dislocation loops formed, both size and density increased with increasing fluence. The dislocation loops interacted with each other forming tangled dislocation structures. At temperatures greater than 373 K loop densities saturated very early in the implantation. The high mobility of point defects and hydrogen and the relatively low hydrogen-vacancy interaction allowed for a large decrease in the damage and retention of hydrogen above room temperature. At high fluences at 303 K bubbles formed preferentially near dislocations and distributed in the region of the displacement damage.

Johnson and Armstrong [43,44] found that blisters formed rapidly in 99.999 % pure copper at a fluence of $7x10^{18}$ D/cm^2. Their experiment was performed with polycrystalline copper samples heated to 350 K and bombarded with a 200 keV deuteron beam at a flux of 150 μA/cm^2 ($9.36x10^{14}$ D/cm^2-s). After blisters formed, the deuterium concentration in the blistered area stayed constant. This was measured by D(d,p)T nuclear reaction profiling during implantation. They found that the critical dose for blistering in Cu is about 1 at. %.

Besenbacher, Bottiger and Myers [26] investigated the effects of defect trapping on the migration of deuterium in Marz-grade, single-crystal nickel of 99.995 % purity. They reported two trap energies for deuterium attached to defects produced by implantation. The first trap, with an energy of 0.24 eV, is associated with the attachment of deuterium to a single vacancy. The other trap was reported at 0.43 eV, associated with deuterium attachment to multiple-vacancy defects. For both trap energies, the deuterium remained mobile at the temperatures relevant to APT. Relatively rapid migration of the trapped deuterium was seen for temperatures between 250 and 350 K.

Petitpierre et al [45] implanted 10 keV D into polycrystalline nickel between 233 and 313 K at a flux of $1.06x10^{15}$ D$^+$/cm^2-s. A ^{4}He beam was used to analyze the deuterium profile in the near surface. The deuterium profiles were found to be flat which suggests that in this temperature range the high diffusivity and recombination coefficient allowed the deuterium to migrate easily. This was independent of implant fluence or flux. Samples implanted at 90 K show two traps with binding energies of 0.43 and 0.24 eV with concentrations of 0.9 % and 4.0 %, respectively. The 0.43 eV trap is associated with a single or multiple vacancy. Polycrystalline Ni also shows a trap at 0.1 eV associated with dislocations and extended lattice defects.

Borgeson et al [46] implanted 2–22 keV deuterons into 25 μm thick cold-rolled nickel foils with a flux of $4.3x10^{14}$ D/cm^2-s near room temperature. Permeation measurements revealed a concentration of $4x10^{-4}$ of saturable bulk traps of binding energy 0.26 eV and a larger concentration of weaker traps. Annealing eliminated these traps. Reemission of deuterium on the upstream surface was found to be diffusion limited. Deuterium was implanted into a surface highly damaged from 20 keV He bombardment. The traps were quickly saturated, but the permeation remained negligible until $3x10^{19}$ D/cm^2. It is thought that blisters formed "channels" to the surface that facilitated the release of deuterium. They also observed evidence to support large concentrations, 10^{-2} to 10^{-3}, of weaker, 0.10 to

0.15 eV, energy traps. Borgeson et al [32] continued work at temperatures of 264 to 600 K. They found that at low temperatures diffusion is delayed by the trapping and detrapping in the bulk and at high temperatures permeation is enhanced due to recombination at the irradiated surface.

316 SS was implanted at 296 K with 1–10 keV D^+ ions to fluences of 10^{17}–10^{19} D/cm^2 by Wilson and Baskes [47]. The samples were held at 296 K for several hours after implantation. They observed that the deuterium migrated with an energy of 0.6 eV and that near surface traps due to radiation damage have an energy of 0.9 eV, ($E_D + E_T$). Samples implanted to 10^{18} D/cm^2 with 10 keV D^+ held $2x10^{-2}$ atom fractions at $E_T = 0.26$ eV and $8x10^{-2}$ atom fractions at $E_T = 0.14$ eV. The 0.14 eV trap became negligible after several hours. 1 keV bombardment resulted in the development of a trap with a binding energy of 0.29 eV.

Wilson and Baskes [48] implanted 304LN SS with 10 keV D^+ or D_3^+ at temperatures between 308 and 368 K at fluxes of $3.3x10^{14}$ or $1x10^{15}$ D/cm^2-s. They found that release from a 0.8 eV radiation damage trap ($E_D + E_T$) was the rate limiting step at temperatures ranging from 308 to 338 K. At temperatures above 368 K recombination becomes an important factor.

Bohdansky et al [49] implanted 6 keV D_3^+ at a flux of $5x10^{14}$ atoms/cm^2-s in 304LN SS at temperatures between 295 to 375 K for fluences up to 10^{19} atoms/cm^2. At low energies most of the deuterium was reflected during implantation. The deuterium retained in the samples was found to be trapped in radiation damage sites with detrapping energies of 0.74 and 0.88 eV ($E_D + E_T$) and migrating through the bulk with a diffusivity activation energy of 0.6 eV. At 375 K, the deuterium in traps was insignificant compared to that migrating. For the fairly clean surface, diffusion was the rate-limiting step. D(^{3}He,α)H nuclear reaction profiling was used to measure the near surface deuterium and TDS was used to measure total retention. The main source of retention was diffusion into the sample.

4 Results

The implanted samples were analyzed using nuclear reaction profiling, thermal desorption spectroscopy (TDS), and scanning electron microscopy (SEM). D(d,p)T nuclear reaction profiling was used to determine the concentration of deuterium in the near-surface region of the samples during the implantation. During Run 6, some samples were implanted that had a zirconium layer on the back surface of the sample. At specified intervals during the implant, $D(^3He,p)^4He$ nuclear reaction profiling was used to measure the amount of deuterium that permeated through the sample into the zirconium layer on the back surface. For all the samples without a zirconium layer on the back surface, deuterium retained in the samples after implantation was determined by heating the samples and measuring the deuterium released by integrating the response of a mass spectrometer with respect to time. SEM provided information on the build-up of blisters and other visual changes in the surface of the samples.

4.1 Thermal Desorption Spectroscopy

Deuterium was released in the form of HD, D_2, and HDO molecules during thermal desorption. The quantities of these molecules released from the samples implanted during each of the experiments are listed in Tables 4.1 to 4.5. A significant amount of carbon accumulated on the surface of the samples implanted during Run 1. Deuterium trapped in the carbon layer was desorbed as CDH_3 and the amount of desorbed CDH_3 is listed in Table 4.1. The carbon layer inhibits the deuterium from reaching the surface of the samples where it can recombine with a hydrogen or deuterium atom and release. Thus, the retention results from this experiment should be considered preliminary. Carbon build-up on the surface is not expected in APT. Run 2 reduced the carbon build-up on the sample with the addition of a cold trap near the samples during the implantation. Therefore, these results are more interesting and applicable to expected APT retention.

The deuterium retention measured by thermal desorption for all of the samples implanted during Runs 4, 5 and 6 is plotted versus fluence in Fig. 4.1a) for the coated and bare Al 6061-T6 samples and in b) for the coated and bare SS 316L samples. A few striking observations can be made from the data. Deuterium retention in the Al 6061-T6 sample implanted with only 150 keV deuterons during Run 1 reached saturation at a significantly smaller value than the Al 6061-T6 samples implanted at multi-energies during Runs 2 and 4. The multi-energy implants create a larger region of damage in the sample where trapping and bubble formation may occur, thus increasing the amount of deuterium that may be retained. The Al 6061-T6 sample implanted with both protons and deuterons during Run 5 retained less deuterium than the Al 6061-T6 sample implanted with only deuterons during Runs 2 and 4. The proton implants always followed the deuteron implants during Run 5, thus the diffusing protons may have exchanged with the trapped deuterons, decreasing the deuterium retention. APT will have three times as many protons as tritons injected into the tube walls simultaneously. During these experiments, the same number of protons and deuterons were implanted in the samples and they were not implanted simultaneously. These differences will have an effect on the tritium retention in the APT tubes compared to the retention

measured in these experiments. In Fig. 4.1 there is a general trend that the samples implanted with both protons and deuterons (Runs 5 and 6) retained less deuterium than the samples implanted with only deuterons (Run 4). This may be due to the fact that the proton implants always followed the deuteron implants, thus the diffusing protons may have exchanged with the trapped deuterons, decreasing the deuterium retention. This will be discussed more in Chapter 5.

The other important observation is that the anodized coating appears to have slightly increased retention whereas the copper and nickel coatings appear to have reduced the deuterium retention. The copper coating lowered the retention in both the SS 316L and Al 6061-T6. The nickel coating nearly eliminated deuterium retention in both the SS 316L and the Al 6061-T6.

Fig. 4.2 compares the deuterium released as HD to that released as D_2 during thermal desorption for the samples implanted during Runs 1 and 2. In general, the deuterium released as HD is thought to be the result of the recombination of atomic D that diffused to the surface of the sample and combined with H. The D_2, however, may originate from bubbles within the metal. The 150 keV, high fluence, monoenergetic implant of Run 1 resulted in an order of magnitude higher release of D_2 than HD. This is a strong indication of the precipitation of bubbles in the region where the deuterium comes to rest in the sample. During Run 2, deuterons with energies between 10 and 200 keV were implanted into the samples. The release of HD remained fairly constant at each fluence indicating that the concentration of mobile deuterium was at a maximum and bubbles were forming. The amount of deuterium apparently released from the bubbles continued to grow as higher fluences were reached. Fig. 4.3 compares the HD and D_2 release from the thermally desorbed samples implanted during Runs 4, 5, and 6. The most significant difference between the desorption spectra from Run 4 and those of Runs 5 and 6 is the decrease in the amount of D_2 released. This is probably due to the addition of the implanted protons during Run 5 and 6. The hydrogen released from the bubbles may be released as H_2, HD, or D_2 in this case. Since, the proton implants always followed the deuteron implants the D_2 release would be decreased. These results will be discussed further in the following sections.

Table 4.1: The thermal desorption data for the samples implanted with 150 keV deuterons during Run 1. The implant fluence and the total deuterium desorbed as HD, D_2, and CDH_3 molecules are listed for each sample.

Sample	Fluence (D/cm^2)	HD (D/cm^2)	D_2 (D/cm^2)	CDH_3 (D/cm^2)	Total D (D/cm^2)
6061-T6 Al	4.62×10^{17}	6.00×10^{15}	6.25×10^{16}	2.10×10^{16}	1.52×10^{17}
	14.43×10^{17}	1.58×10^{16}	6.12×10^{16}	3.98×10^{16}	1.78×10^{17}
	19.05×10^{17}	1.73×10^{16}	7.41×10^{16}	2.45×10^{16}	1.90×10^{17}
	19.05×10^{17}	1.85×10^{16}	9.02×10^{16}	0.01×10^{16}	1.99×10^{17}

Table 4.2: The thermal desorption data for the samples from Run 2 and the water backed sample implanted during Run 3. The implant fluence and the total deuterium desorbed as HD and D_2 molecules are listed for each sample.

Sample	Energy (keV)	Fluence (D/cm^2)	HD (D/cm^2)	D_2 (D/cm^2)	Total D (D/cm^2)
6061-T6 Al	10	0.156×10^{17}	1.02×10^{16}	1.00×10^{15}	1.23×10^{16}
	30	0.156×10^{17}	5.90×10^{15}	0.	6.00×10^{15}
	70	0.156×10^{17}	9.10×10^{15}	1.20×10^{15}	1.14×10^{16}
	130	0.161×10^{17}	6.40×10^{15}	1.00×10^{14}	6.50×10^{15}
	200	0.158×10^{17}	7.10×10^{15}	3.00×10^{14}	7.70×10^{15}
Run 3 Al	200	1.35×10^{17}	2.03×10^{16}	2.56×10^{16}	7.15×10^{16}
6061-T6 Al	10-200	0.787×10^{17}	2.39×10^{16}	9.90×10^{15}	4.38×10^{16}
	10-200	1.592×10^{17}	2.06×10^{16}	1.66×10^{16}	5.38×10^{16}
	10-200	2.084×10^{17}	2.08×10^{16}	2.26×10^{16}	6.61×10^{16}
	10-200	3.676×10^{17}	3.13×10^{16}	4.12×10^{16}	1.137×10^{17}
	10-200	4.463×10^{17}	2.32×10^{16}	4.11×10^{16}	1.053×10^{17}

Table 4.3: The thermal desorption data for the samples from Run 4. The implant fluence and the total deuterium desorbed as HD and D_2 molecules are listed for each sample.

Sample	Fluence (D/cm^2)	HD (D/cm^2)	D_2 (D/cm^2)	Total D (D/cm^2)
6061-T6 Al	3.50×10^{18}	2.23×10^{16}	3.40×10^{17}	7.03×10^{17}
Electroless Cu/Al	0.93×10^{18}	1.17×10^{16}	1.11×10^{15}	1.39×10^{16}
	2.11×10^{18}	1.09×10^{16}	1.03×10^{15}	1.29×10^{16}
	3.04×10^{18}	2.48×10^{16}	9.19×10^{15}	4.31×10^{16}
316L SS	0.93×10^{18}	2.33×10^{16}	8.40×10^{16}	1.91×10^{17}
	2.11×10^{18}	3.91×10^{16}	8.80×10^{16}	2.15×10^{17}
	3.04×10^{18}	2.24×10^{16}	1.20×10^{17}	2.63×10^{17}
Electroless Cu/SS	0.93×10^{18}	4.94×10^{16}	9.00×10^{14}	5.12×10^{16}
	2.11×10^{18}	6.21×10^{16}	4.33×10^{16}	2.63×10^{17}
	3.04×10^{18}	4.94×10^{16}	5.66×10^{16}	1.63×10^{17}

Table 4.4: The thermal desorption data for the samples from Run 5. The implant fluence and the total deuterium desorbed as HD, D_2, and HDO molecules are listed for each sample.

Sample	Fluence (D/cm^2)	HD (D/cm^2)	D_2 (D/cm^2)	HDO (D/cm^2)	Total D (D/cm^2)
6061-T6 Al	1.0×10^{18}	5.40×10^{16}	0	0	5.40×10^{16}
	2.0×10^{18}	1.70×10^{17}	9.08×10^{15}	0	1.88×10^{17}
Electroplated	1.0×10^{18}	2.21×10^{16}	0	0	2.21×10^{16}
Cu/Al (1 μm)	2.0×10^{18}	6.35×10^{16}	0	0	6.35×10^{16}
	3.0×10^{18}	6.17×10^{16}	0	0	6.17×10^{16}
Electroless Cu/Al (6 μm)	3.0×10^{18}	3.07×10^{16}	8.14×10^{13}	0	3.23×10^{16}
Electroless	1.0×10^{18}	0	0	0	0
Ni/Al	2.0×10^{18}	4.86×10^{14}	0	0	4.86×10^{14}
	3.0×10^{18}	0	0	0	0
Anodized Al	1.0×10^{18}	0	0	4.92×10^{16}	4.92×10^{16}
	2.0×10^{18}	0	0	2.18×10^{17}	2.18×10^{17}

Table 4.5: The thermal desorption data for the samples from Run 6. The implant fluence and the total deuterium desorbed as HD and D_2 molecules are listed for each sample.

Sample	Fluence (D/cm^2)	HD (D/cm^2)	D_2 (D/cm^2)	Total D (D/cm^2)
316L SS	1.0×10^{18}	2.67×10^{16}	0	2.67×10^{16}
	2.0×10^{18}	4.97×10^{16}	1.10×10^{15}	5.19×10^{16}
Cu/SS	1.0×10^{18}	2.88×10^{16}	0	2.88×10^{16}
	2.0×10^{18}	8.82×10^{16}	1.10×10^{15}	9.05×10^{16}
Ni/SS	1.0×10^{18}	0	0	0
	2.0×10^{18}	5.92×10^{14}	0	5.92×10^{14}

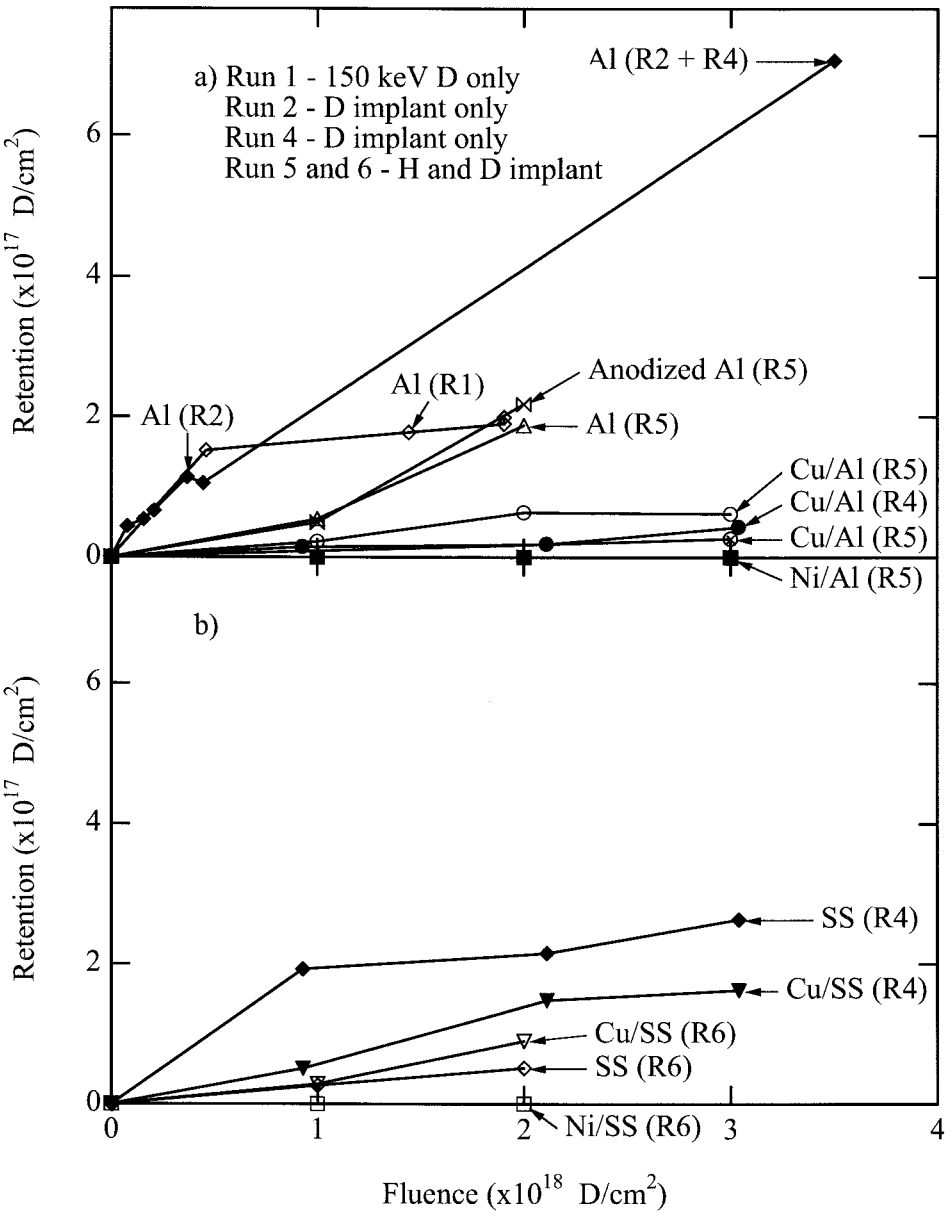

Figure 4.1: The deuterium retention sums from Runs 4, 5 and 6 for the a) coated and bare Al 6061-T6 samples and b) the coated and bare SS 316L samples.

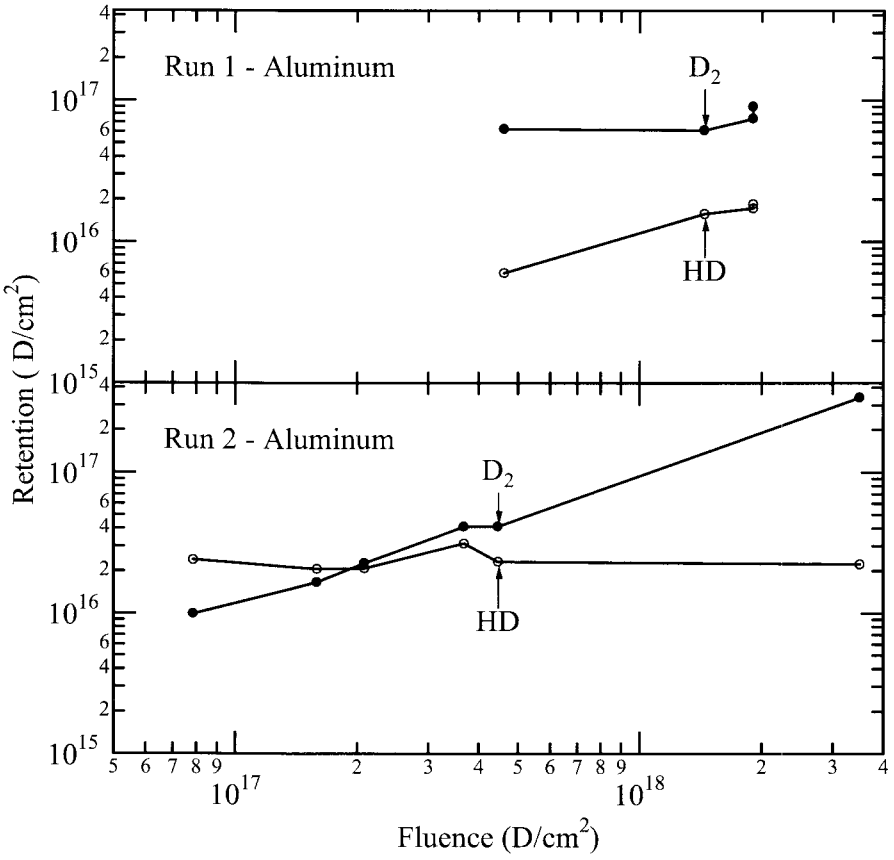

Figure 4.2: A comparison of the deuterium thermally desorbed as HD versus D_2 for the Al 6061-T6 samples implanted with a) a monoenergetic beam during Run 1 and b) a multi-energy beam during Run 2.

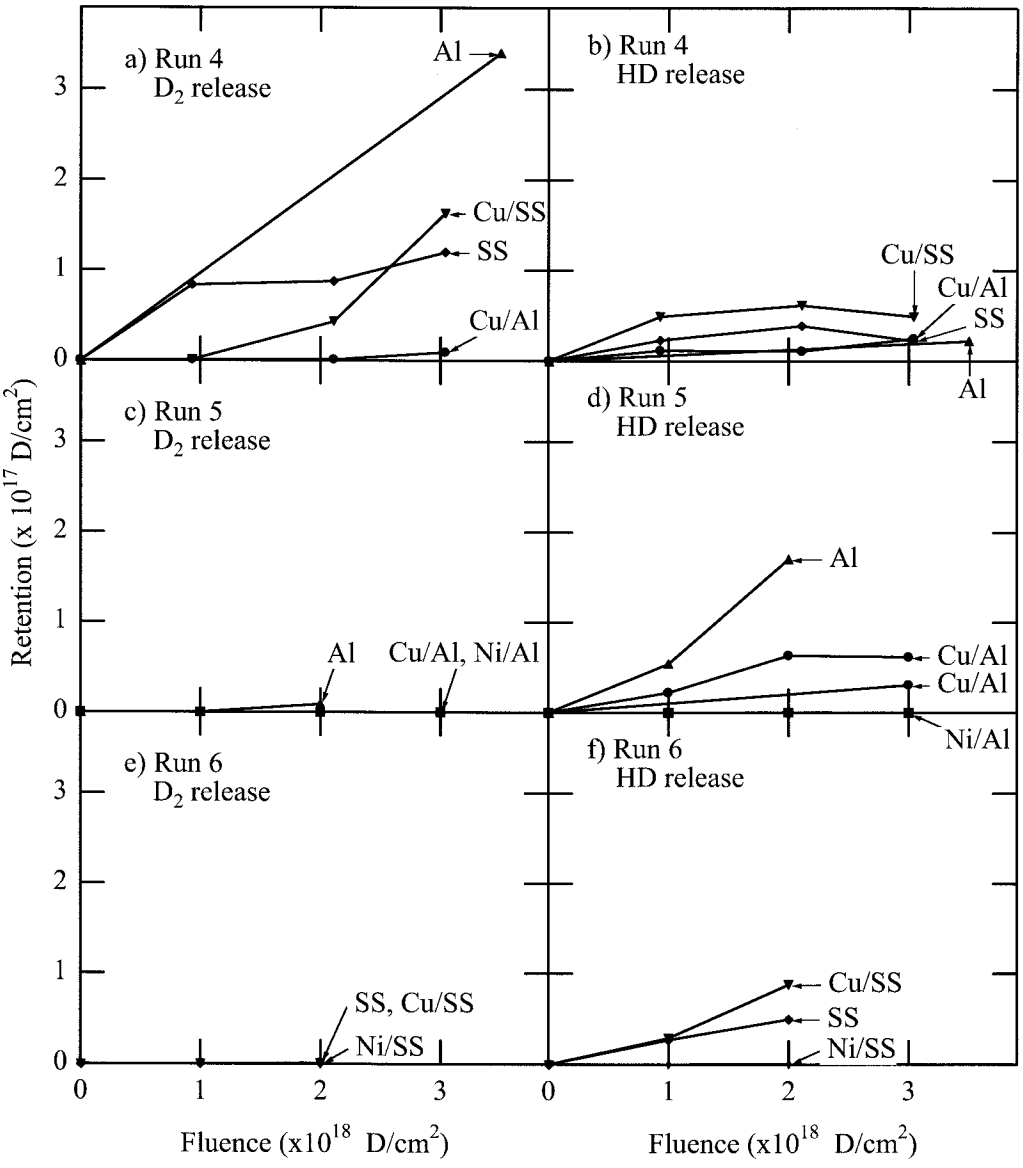

Figure 4.3: A comparison of the deuterium thermally desorbed as HD versus D_2 for the samples implanted during Runs 4, 5, and 6.

4.2 D(d,p)T Nuclear Reaction Profiling

D(d,p)T nuclear reaction analysis is used to measure the build-up of deuterium in the near surface region of the samples during implantation. The detector geometry used during Runs 1 through 4 allowed protons resulting from the D(d,p)T reaction anywhere on the stainless steel sample holder, the stainless steel mounting screws, and the Al 6061–T6 samples to impinge on the detector. Therefore only a fraction of the signal is attributed to the Al 6061-T6 samples and the results must be considered only qualitatively. No specific information on a single sample is known, only the general buildup of deuterium in the near-surface of the samples over the entire beam spot. Deuterium buildup in the near surface region of the samples implanted during Run 1 is shown in Fig. 4.4. There was a steady increase in the yield of detected deuterium throughout the high fluence implant resulting in a concentration of 0.027 D/Al (or 3.3×10^{16} D/cm^2) within the first 0.2 μm of the sample. Two features in Fig. 4.4 are worth mentioning. The first is the dip in the spectrum when 20 % of the total sample area was replaced with new samples. The second is the 22 % decrease in the spectrum when the sample heater was left at 348 K overnight. Normally the heater is turned off overnight. The deuterium concentration recovered after 20 minutes or 3×10^{16} D/cm^2 of resumed implantation. Fig 4.5 shows the calculated D/Metal concentration assuming a thin, uniformly loaded layer extending from 0 to 0.2 μm deep for the D(d,p)T profiling during Run 2. The assumption of the uniformity is only a rough approximation to the true retention profile. The average deuterium concentration within this 0.2 μm layer was 0.014 D/Al at a fluence of 4.5×10^{17} D/cm^2. This concentration and thickness corresponds to 1.7×10^{16} D/cm^2, or about 16 % of the total D measured from thermal desorption. Fig 4.6 shows the proton yields measured during Run 4. The sample matrix during this run consisted of Al 6061–T6, SS 316L, and copper surfaces. Therefore, analysis of the data is difficult due to the difference in the deuterium range in the various metals. The trend in the increase of the deuterium buildup with fluence is still clearly visible.

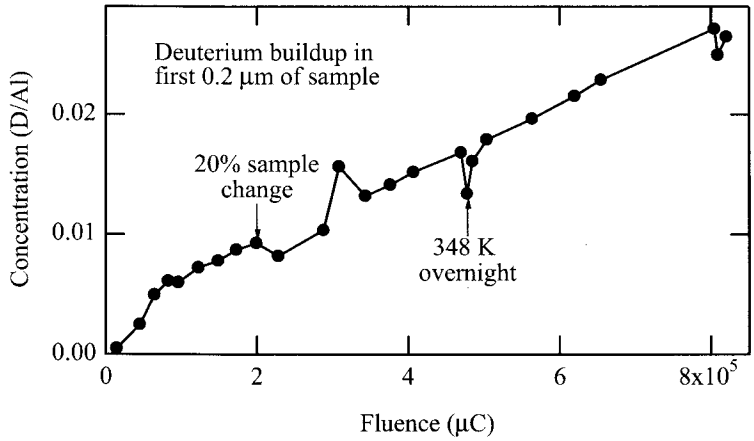

Figure 4.4: The total deuterium in the first 0.2 μm depth of the samples measured by nuclear reaction profiling versus the fluence for the Run 1 samples.

The nuclear reaction profiling analysis of the samples implanted during Runs 5 and 6 was completed using the ErD_2 calibrations discussed in Sec. 2.3.2. The five silicon detectors used during these experiments were collimated to limit detection to a single sample. The collection fluence for the spectra obtained with the 200 keV deuterons was $4.76x10^{16}$ D/cm^2. The deuterium concentration versus depth for the implanted samples was calculated in a manner similar to that of the ErD_2 samples. The concentration profiles for each sample are shown in following sections. Integrating the deuteron concentration over the depth gives the total deuterium in the near surface region of the samples during the implant. This is plotted versus fluence in Fig. 4.7a) for Run 5 samples and b) for Run 6 samples. The anodized Al 6061-T6 has the highest deuterium concentration followed by the Al 6061-T6. The copper and nickel coated samples and the SS 316L all show considerably less deuterium build-up during the implant.

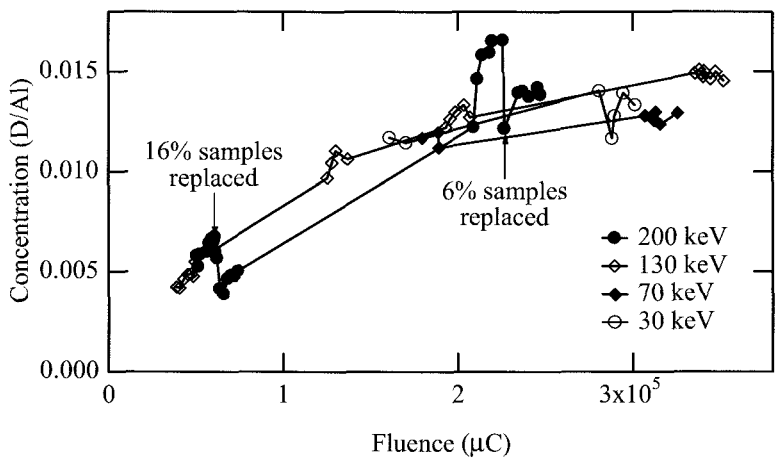

Figure 4.5: The total deuterium in the first 0.2 μm depth of the samples measured by nuclear reaction profiling versus the fluence for the Run 2 samples.

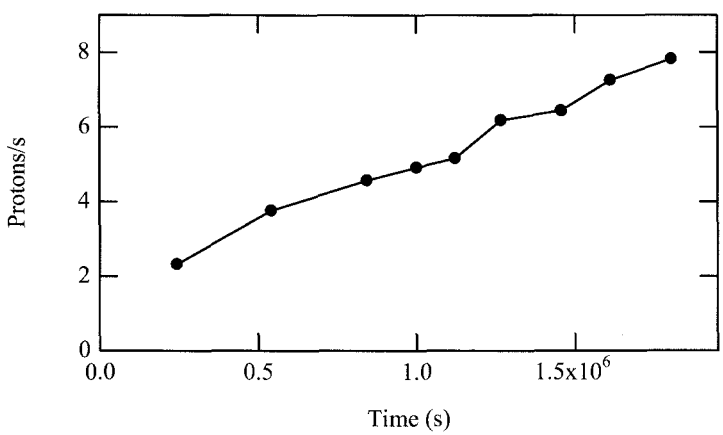

Figure 4.6: The protons collected in the silicon detector versus time during Run 4.

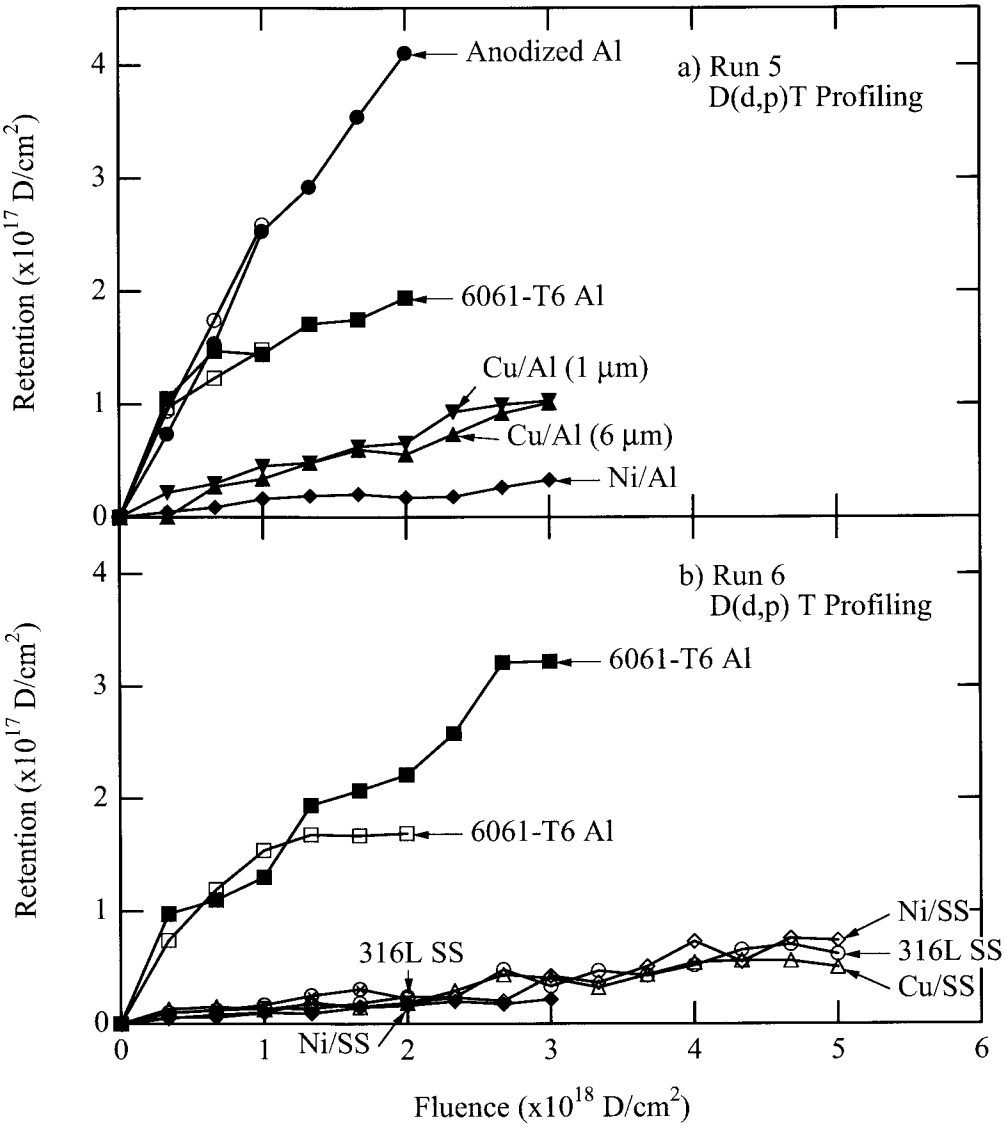

Figure 4.7: The total deuterium in the near surface region of the samples measured by nuclear reaction profiling versus the fluence for the a) Run 5 samples and b) Run 6 samples. The accumulation of deuterium in the copper and nickel coated samples and the SS 316L is considerably less than that of the bare and anodized Al 6061-T6.

4.3 D(^{3}He,p)^{4}He Nuclear Reaction Profiling

The ErD_2 calibration for the D(^{3}He,p)^{4}He nuclear reaction profiling discussed in Sec. 2.4.2 was used to calculate the deuterium permeation for samples implanted during Run 6. Collection fluences of either $5x10^{15}$ ^{3}He/cm^2 or $1x10^{16}$ ^{3}He/cm^2 were used to obtain spectra with sufficient statistics. The deuterium concentration versus depth profiles are discussed for each sample in following sections. The integration of the depth profile gives the total concentration of deuterium trapped in the zirconium layer on the backside of the samples and thus the amount of permeated deuterium. The measured deuterium is listed in Table 4.6 for the samples implanted during Run 6. These values are plotted for the SS 316L samples in Fig. 4.8. Deuterium readily permeated both the SS 316L and copper coated SS 316L samples. In neither case has a steady-state been reached. All of the other samples do not show detectable amounts of permeation. The D(^{3}He,p)^{4}He nuclear reaction profiling technique was also used to profile the front surface of the samples at the end of the experiment. Table 4.7 compares the near-surface deuterium measured by the D(d,p)T reaction during implantation to the deuterium measured by D(^{3}He,p)^{4}He at the end of the experiment. The decrease in the measured deuterium is probably due to the exchange of the implanted protons with the deuterons after the final deuteron implant.

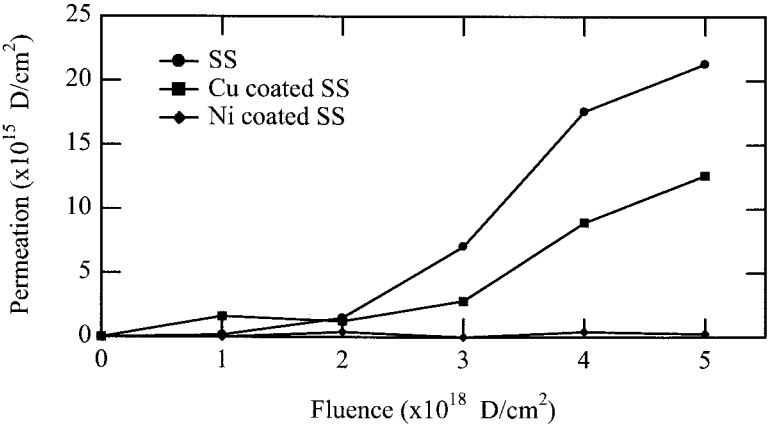

Figure 4.8: The concentration of permeated deuterium versus the implant fluence for the SS 316L samples implanted during Run 6.

Table 4.6: The measured deuterium at the given fluences in the zirconium layer on the backside of the samples.

Sample	Permeated Deuterium (D/cm^2)				
Fluence	$1x10^{18}$ D/cm^2	$2x10^{18}$ D/cm^2	$3x10^{18}$ D/cm^2	$4x10^{18}$ D/cm^2	$5x10^{18}$ D/cm^2
SS	$1.66x10^{14}$	$1.49x10^{15}$	$7.06x10^{15}$	$1.76x10^{16}$	$2.13x10^{16}$
Cu/SS	$1.61x10^{15}$	$1.23x10^{15}$	$2.80x10^{15}$	$8.92x10^{15}$	$1.26x10^{16}$
Ni/SS	NA	$< 5x10^{13}$	$< 3x10^{14}$	$< 3x10^{14}$	$< 3x10^{14}$
Al	$< 3x10^{14}$	$< 3x10^{14}$	$< 5x10^{13}$	NA	NA
Cu/Al	$< 3x10^{14}$	$< 3x10^{14}$	$< 2x10^{14}$	NA	NA
Ni/Al	$< 3x10^{14}$	$< 3x10^{14}$	$< 5x10^{13}$	NA	NA

Table 4.7: The measured deuterium in the front surface of the samples. The final deuterium fluence reached before the measurement, the depth of the measured deuterium, and the measured deuterium during $D(^3He,p)^4He$ and D(d,p)T profiling are all listed.

Sample	Fluence (D/cm^2)	Layer Profiled (μm)	$D(^3He,p)^4He$ (D/cm^2)	D(d,p)T (D/cm^2)
SS	$5.0x10^{18}$	0.30	$1.15x10^{16}$	$6.19x10^{16}$
Cu/SS	$5.0x10^{18}$	0.41	$1.41x10^{16}$	$5.05x10^{16}$
Ni/SS	$5.0x10^{18}$	0.30	$1.58x10^{16}$	$7.40x10^{16}$
Al	$3.0x10^{18}$	1.50	$2.00x10^{17}$	$3.22x10^{17}$
Cu/Al	$3.0x10^{18}$	0.33	$1.42x10^{16}$	NA
Ni/Al	$3.0x10^{18}$	0.21	$3.80x10^{15}$	$2.18x10^{16}$

5 Aluminum 6061-T6

Al 6061-T6 is the base-line material for these experiments. All six experiments included Al 6061-T6 samples in the matrix. During Run 1, high flux 150 keV deuterons were implanted into Al 6061-T6 to high fluences. Multi-energy deuterons were implanted during Run 2. This multi-energy implant was continued during Run 4 to a fluence of $3.5x10^{18}$ D/cm^2. Both protons and deuterons were implanted to a fluence of $2.0x10^{18}$ D (and p)/cm^2 during Run 5 and $3.0x10^{18}$ D (and p)/cm^2 during Run 6.

The thermal desorption spectra for the HD and D_2 molecules released from the Al 6061-T6 samples implanted during Run 1 are shown in Fig. 5.1. The 1 K/s temperature ramp is plotted on the right-hand axis. There is a steady increase in both the desorbed HD and D_2. The thermal desorption spectra of the multi-energy implants during Run 2 are shown in Fig. 5.2. Again, there is a steady increase in the desorbed deuterium. There are several differences between the Run 1 data and the Run 2 data. First, during Run 1 carbon built up on the surface of the sample during the implant, increasing the retention of deuterium. The mono-energetic implant of Run 1 produced damage in a smaller range in the sample than the multi-energy implants of Run 2. But, Run 1 went to a much higher fluence. Generally, the broad distribution of deuterium released as HD is thought to be the result of deuterium diffusion to the surface of the sample where it recombines with a hydrogen atom and is released. As the temperature of the sample increases, the D_2 gas pressure inside the blisters increases until the blisters rupture. The narrow D_2 peaks in Fig. 5.2 are thought to be the result of this effect. Fig. 5.3 shows the desorption spectra for low fluence implants of single energies during Run 2. The small release of D_2 in Fig. 5.3 indicates that bubbles are not yet formed in these samples. The TDS data for Runs 4 and 5 are shown in Fig. 5.4a-c) and d-f), respectively. The deuterium was released in the form of HD and D_2 during the thermal ramp. The released HD shown in Fig. 5.4b) is most likely the result of deuterium atoms trapped in the sample diffusing to the surface where they recombine with a proton forming and HD molecule. However, Fig. 5.4c) shows that most of the deuterium was released as D_2 molecules that probably formed in bubbles and blisters in the Al 6061-T6. The H_2, HD, and D_2 spectra from the samples implanted with both protons and deuterons during Run 5 (Fig. 5.4d-f)) all have a narrow peak around 675 K. This peak was not visible in the Run 4 H_2 data and may be due to H_2 bubbles and blisters forming in the Al 6061-T6 with the addition of the proton implantation. The broad, diffuse peak in the HD data from Run 4 also is missing in the Run 5 data. The Run 5 implantation cycles always ended with protons, therefore the reduction in deuterium released as D_2 may be the result of the protons "washing out" or exchanging with the deuterium trapped in bubbles and blisters. Kamada *et al* [50] completed an experiment with successive implants of 25 keV D_2^+ and 100 or 140 keV H_2^+ into Al 6061-T6 as well. They found that the deuterium retained in the sample decreased as the hydrogen fluence increased even though the implant energy of the hydrogen was significantly larger than the deuterium. This suggests that isotopic exchange from a collision between the incoming hydrogen and the trapped deuterium was probably not the cause of deuterium de-trapping, but was caused by some other exchange mechanism. This is consistent with the decrease in trapped deuterium from Run 4 to Run 5.

30,000X SEM images of the Al 6061-T6 samples implanted during Run 2 are shown in Fig. 5.5. Extensive blistering is seen at all of the fluences. Figs. 5.6a) and b) show SEM images at 500X of the Al 6061-T6 sample before and after implantation in Run 4, respectively. The implantation has clearly caused a significant amount of damage. The SEM image at 30,000X shown in Fig. 5.6c) of the implanted sample distinctly shows that blisters have formed on the surface. The SEM images at 2,000X and 20,000X shown in Fig. 5.7 of the Al 6061-T6 sample before and after implantation in Run 5 reveal the high degree of damage done to the Al 6061-T6 surface. Kamada *et al* [51] have also performed 25 keV H_2^+ implants on thin aluminum samples for TEM analysis. They found that along with the laterally arranged bubbles in the implant region there were "tunnel structures" that occupy a much larger volume than the bubbles and make the surface of the sample rough. These tunnels do not connect to the surface, allowing pressure to build-up that may lead to blisters.

The D(d,p)T nuclear reaction profiling (NRP) results of the build-up of deuterium in the near-surface region of the samples during Run 5 are shown in Fig. 5.8. The depth resolution of these measurements, due to limitations in the experimental setup, is not sufficient to distinguish between deuterium trapped at the surface oxide or deuterium trapped at specific depths in the bulk. However, the quantity of deuterium in the near-surface may be calculated from the profiles. There is a steady increase in the concentration throughout the implant. Both the retention versus fluence plot, Fig. 4.1, and the NRP results indicate that the deuterium retention in Al 6061-T6 has not reached saturation. The D(d,p)T results for the samples implanted during Run 6 are shown in Fig. 5.9. At 3.0×10^{18} D/cm^2 the deuterium retention still does not appear to have reached saturation. After completion of Run 6, the front surface of the Al 6061-T6 sample was profiled using the D(^{3}He,p)^{4}He nuclear reaction. The results are shown in Fig. 5.10. The depth resolution for this technique was much better than the D(d,p)T profiling. Deuterium was detected to a depth of 1.5 μm, the limit of this technique.

Deuterium permeation measurements were taken at regular intervals throughout Run 6. A thin zirconium layer on the backside of the samples trapped deuterium that permeated through the sample. After each 1×10^{18} D (and p)/cm^2 implant cycle, the zirconium was profiled by the D(^{3}He,p)^{4}He nuclear reaction. The deuterium profile was integrated to determine the total amount of deuterium trapped in the zirconium. The deuterium profiles from the Zr on the Al 6061-T6 samples implanted up to a fluence of 3×10^{18} D/cm^2 are shown in Fig. 5.11. No deuterium was detected in the Zr, statistical scatter is observed in the spectra.

Typically, the low surface recombination rate for aluminum results in a high concentration of deuterium in the implantation region even at low fluxes. This high concentration of deuterium combined with a low solubility leads to the formation of bubbles that make modeling the behavior of hydrogen in aluminum difficult. However, extensive research has been completed on hydrogen interaction in aluminum and how bubbles may form. Myers *et al* [39] discuss three hydrogen traps; the surface oxide, vacancy defects caused by irradiation defects, and D_2 bubbles. The irradiation defects have a binding enthalpy of 0.52 eV. However, the trapping at the surface oxide and in bubbles is significantly stronger than that at the irradiation defects. Ades and Companion discussed the formation of blisters in Ref 52. Hydrogen is thought to diffuse to voids where it combines to form molecular hydrogen. With increased concentrations the pressure will increase and

enlarge the void. However, two atoms at interstitial sites adjacent to a vacancy are more stable than a hydrogen molecule. This suggests that hydrogen atoms will collect at sites around the void instead of forming molecules. The stress caused by the slightly negative charge of the atoms around the border of the void may promote blisters. Although, permeation was not detected up to fluences of 3.0×10^{18} D/cm^2, the amount of deuterium retained in the sample is higher than that desired by APT.

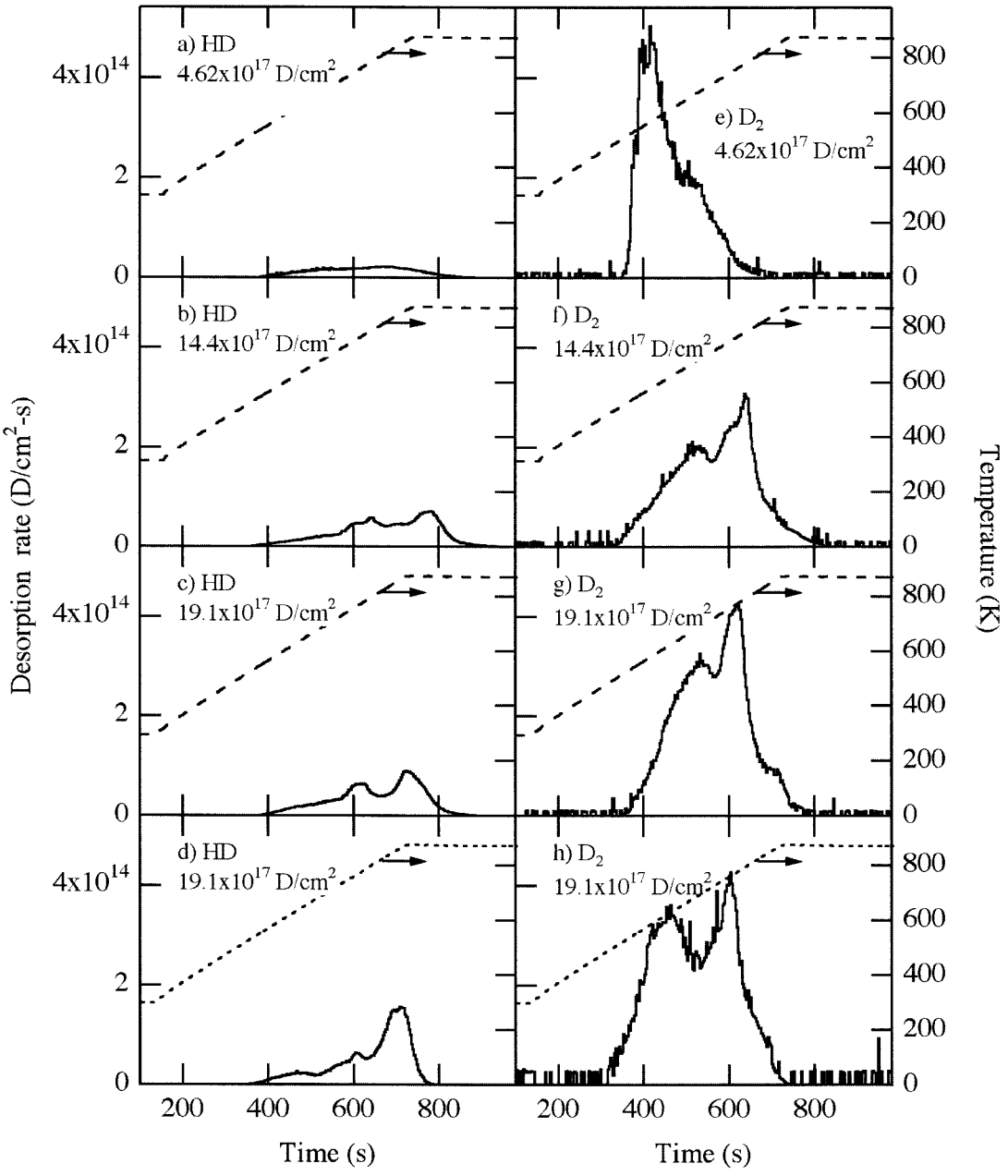

Figure 5.1: The thermal desorption spectra for the Al 6061-T6 samples implanted with 150 keV deuterons during Run 1.

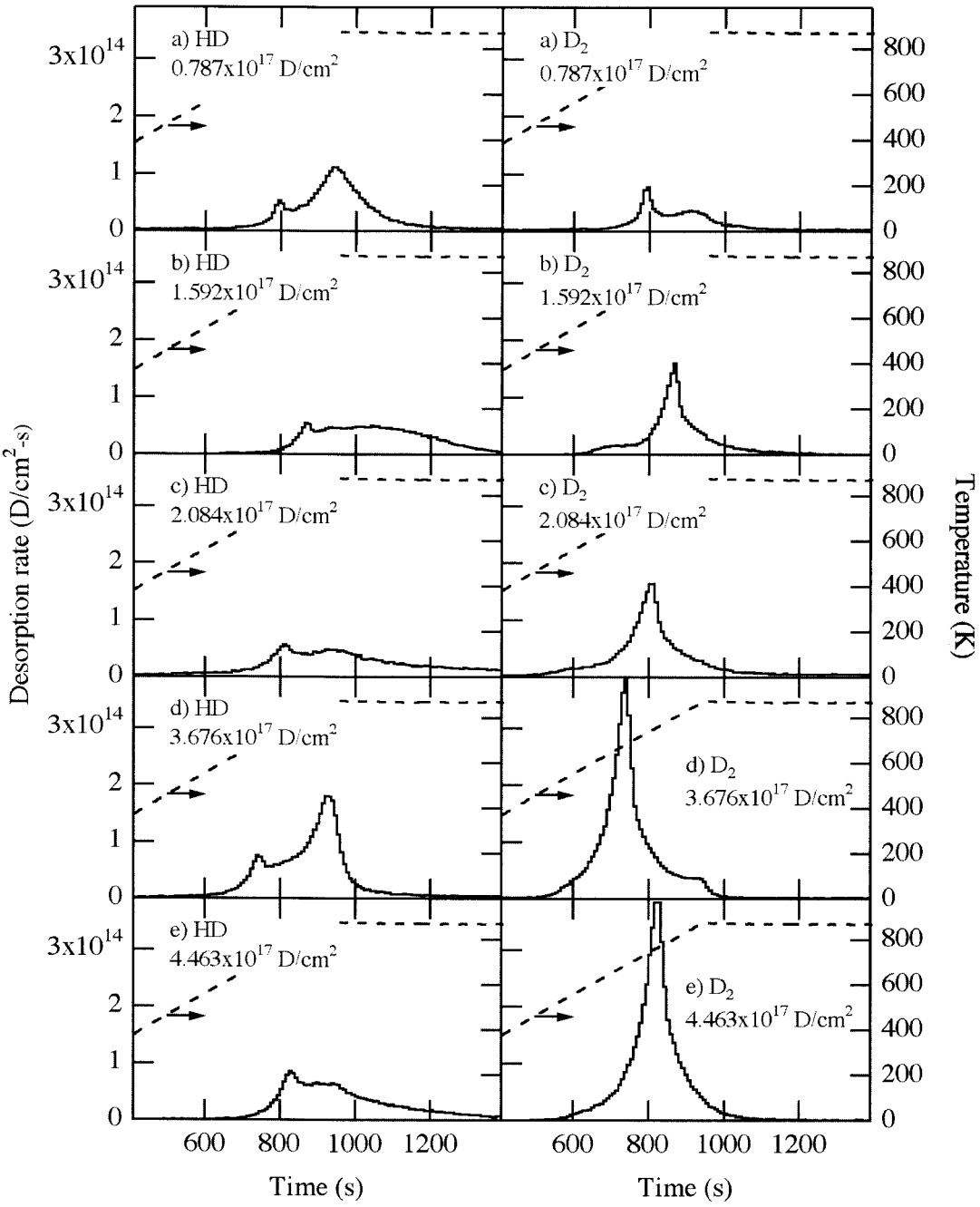

Figure 5.2: The thermal desorption spectra for the Al 6061-T6 samples implanted with multi-energy deuterons during Run 2.

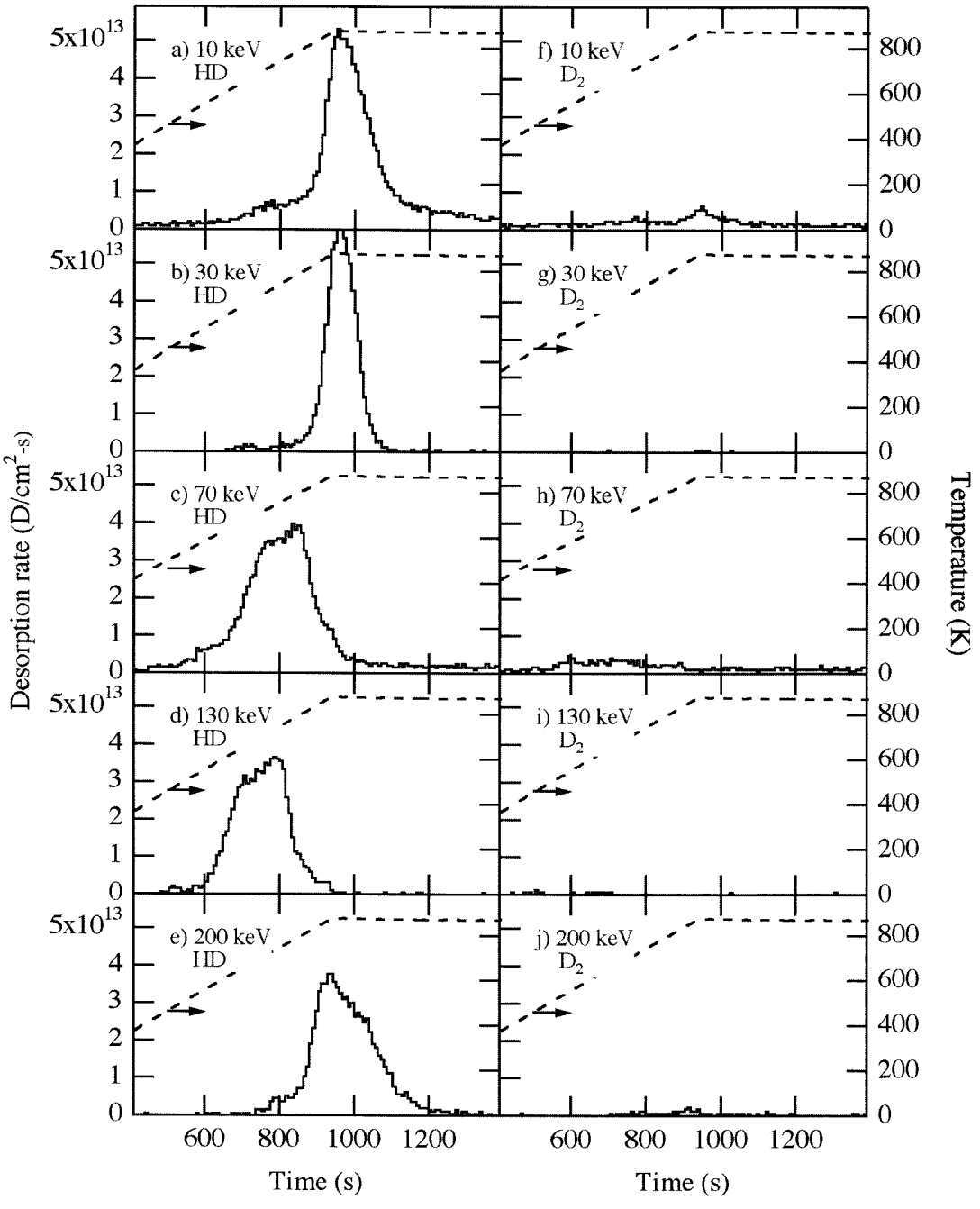

Figure 5.3: The thermal desorption spectra for the Al 6061-T6 samples implanted with 10, 30, 70, 130 and 200 keV single energy deuterons during Run 2. The low fluence prevented bubbles from forming in the Al 6061-T6, resulting in the mobile deuterium releasing as HD.

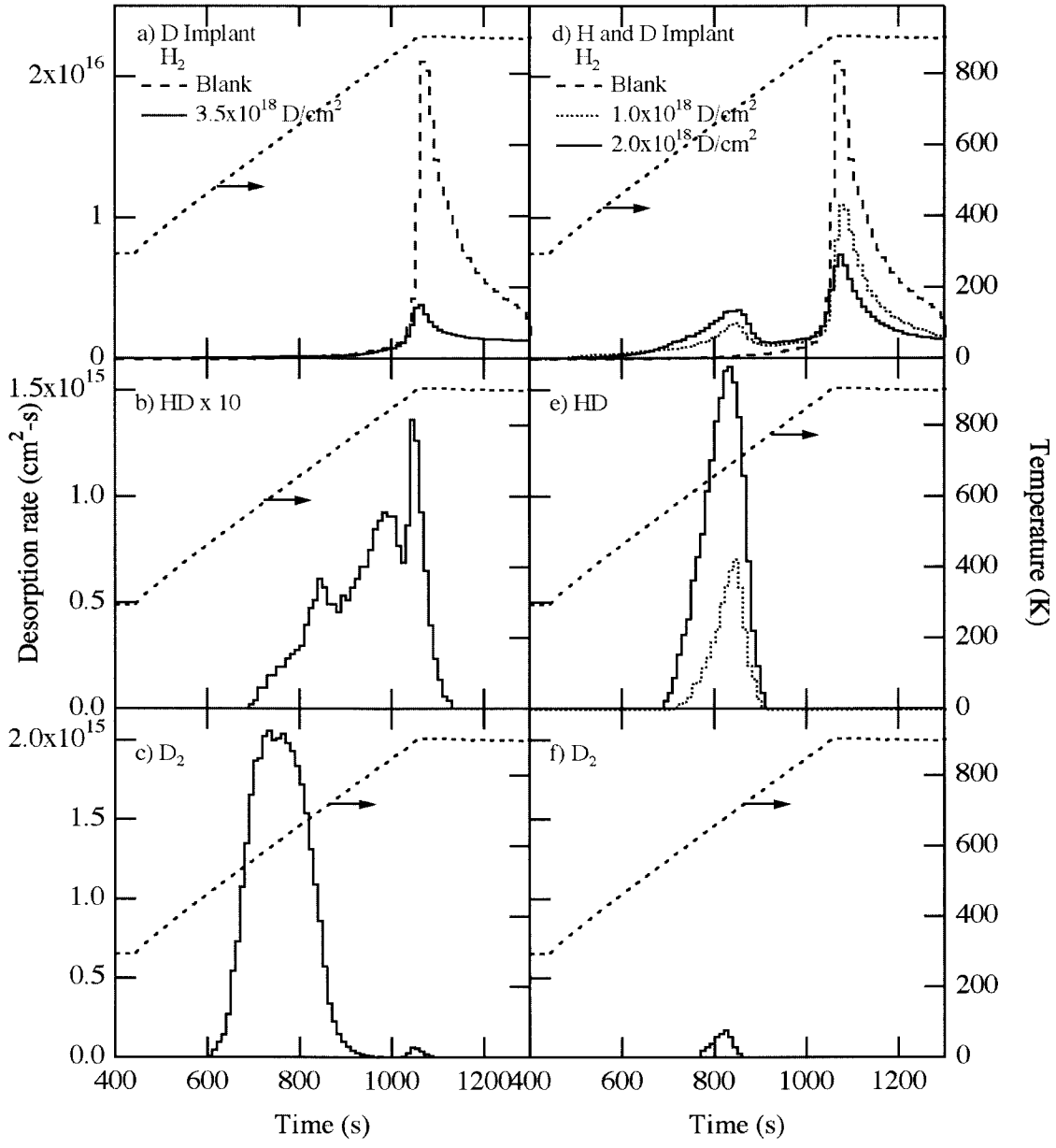

Figure 5.4: The thermal desorption spectra for the Al 6061-T6 samples implanted with deuterons during Run 4 (a-c) and deuterons and protons during Run 5 (d-f). Notice that the spectrum in b) is multiplied by a factor of ten. The broad HD spectrum in b) is probably the result of deuterium diffusing to the surface and recombining with hydrogen. The narrow peaks of H_2, HD, and D_2 at 675 K in c-f) are due to the release from bubbles.

a) Fluence = 0.79×10^{17} D/cm^2

b) Fluence = 2.08×10^{17} D/cm^2

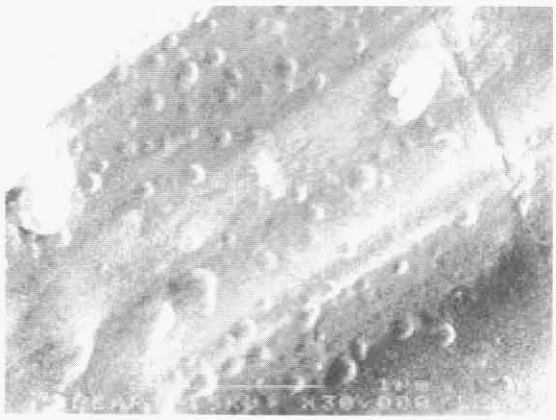

c) Fluence = 4.46×10^{17} D/cm^2

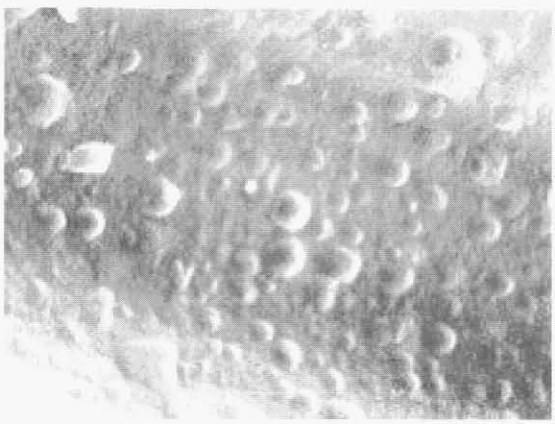

Figure 5.5: SEM images of the Al 6061-T6 samples implanted with multi-energy deuterons to fluences of a) 0.79×10^{17} D/cm^2, b) 2.08×10^{17} D/cm^2, and c) 4.46×10^{17} D/cm^2 during Run 2. The surface shows an increase of blistering with the increase of fluence.

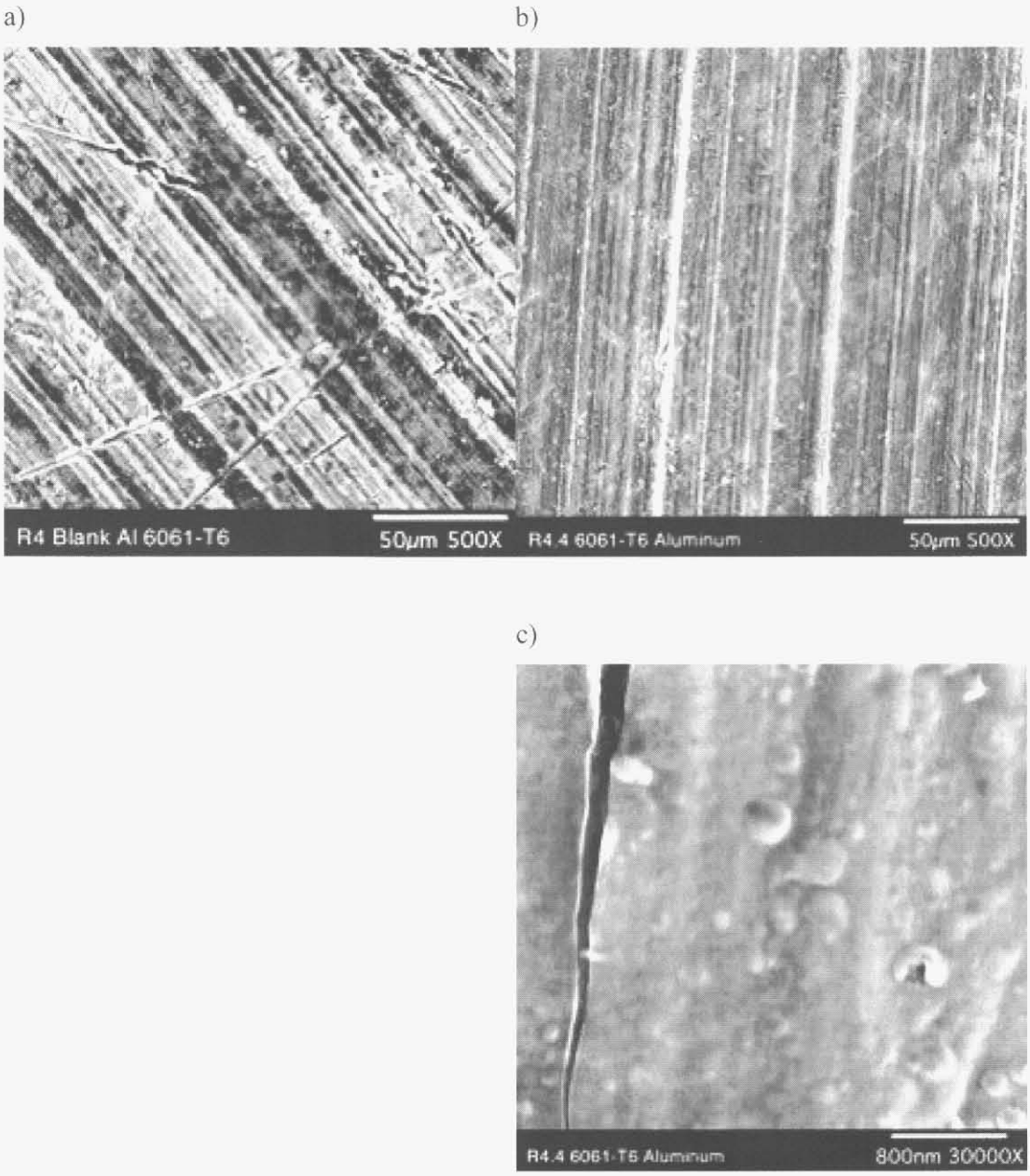

Figure 5.6: SEM images of the Al 6061-T6 sample before implantation at 500X (a) and after the implantation of 3.5×10^{18} D/cm^2 during Run 4 at 500X (b) and 30,000X (c). The surface shows a significant amount of damage due to the implantation. Cracks and blisters on the surface are clearly visible.

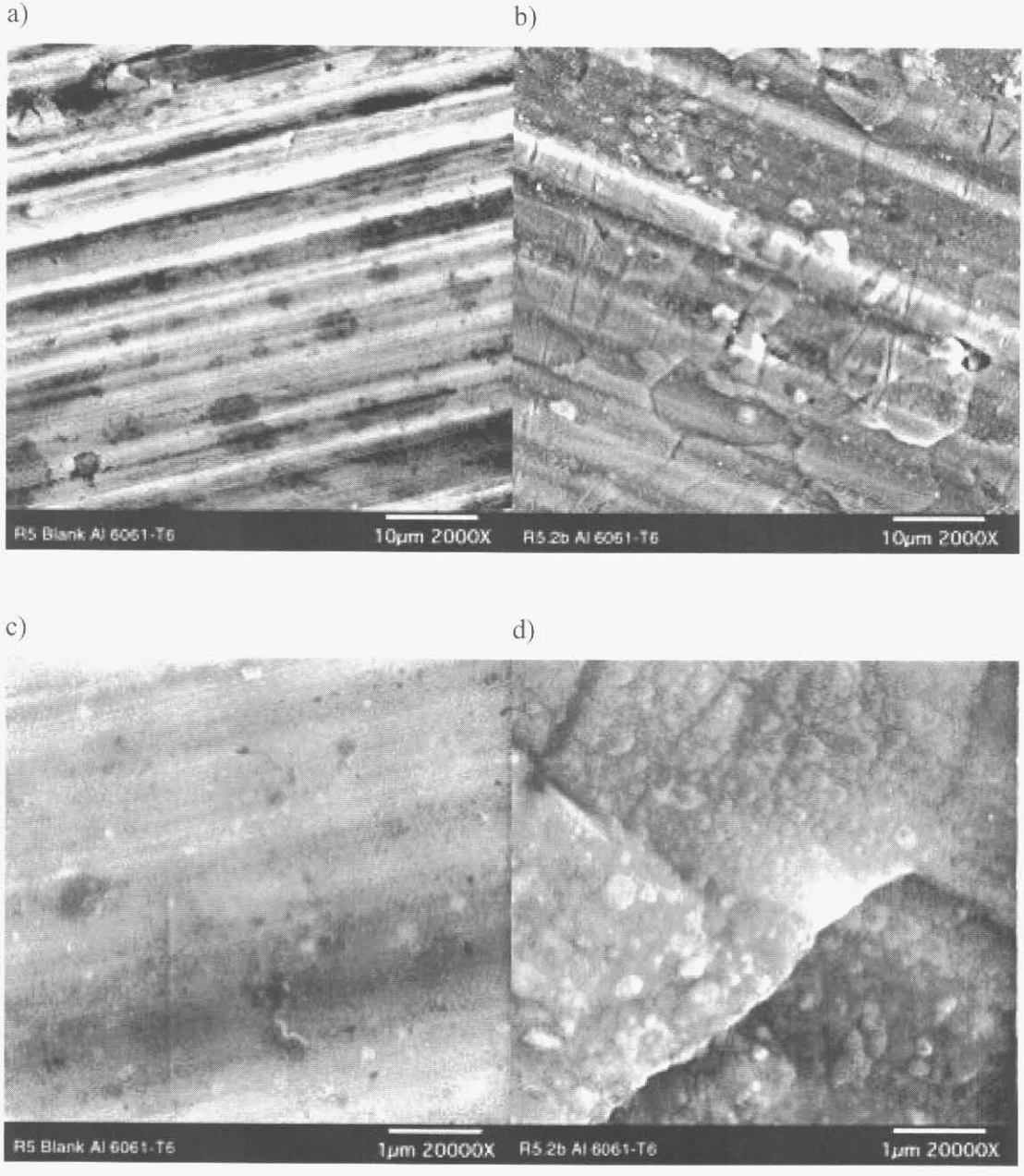

Figure 5.7: SEM images of the Al 6061-T6 sample before implantation at 2,000X (a) and 20,000X (c). SEM images of the Al 6061-T6 samples after the implantation of $2x10^{18}$ D/cm^2 and $2x10^{18}$ p/cm^2 during Run 5 at 2,000X (b) and 20,000X (d). There is considerable damage to the surface of the sample due to the implantation. Blisters and cracks on the surface are clearly visible.

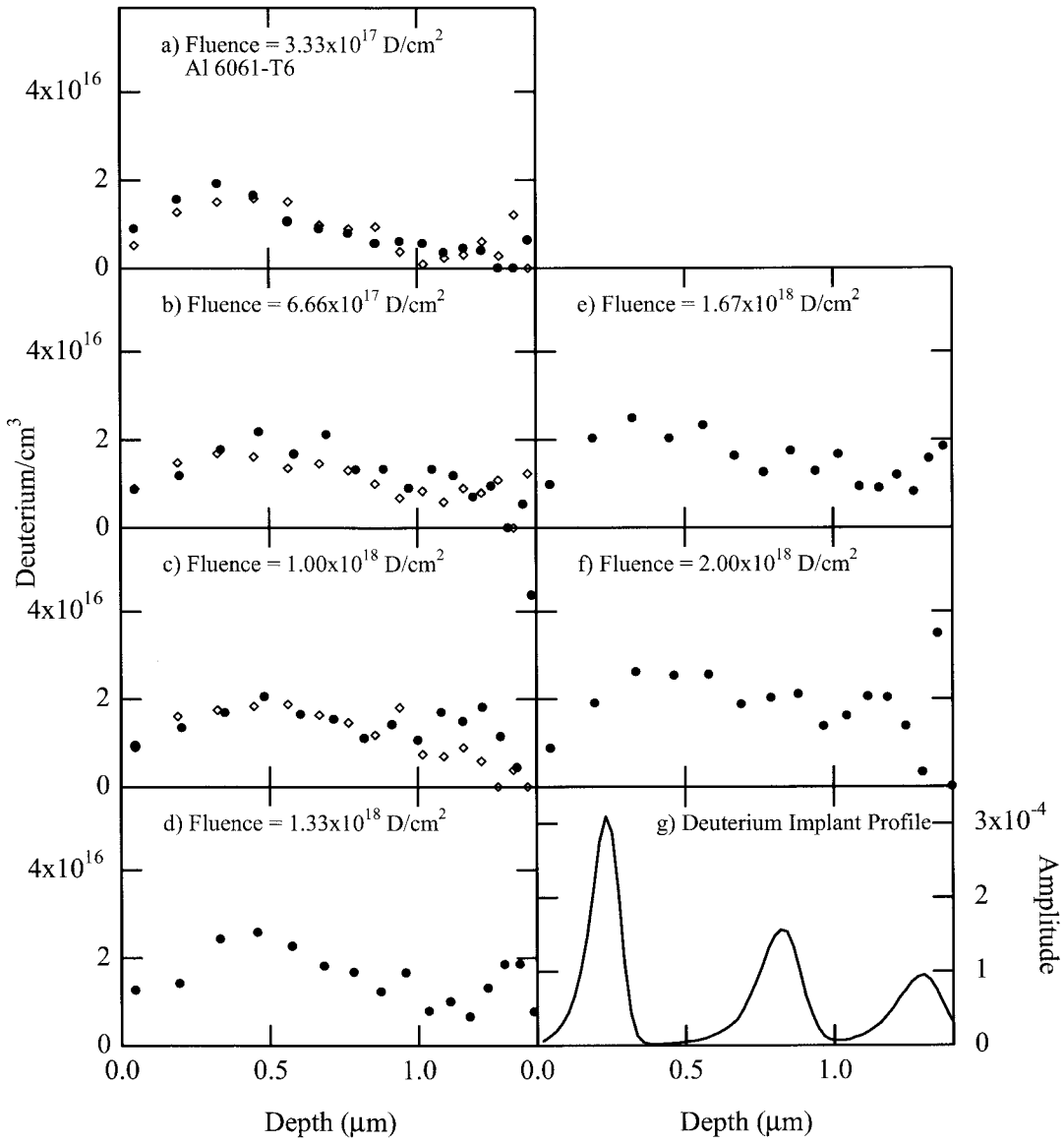

Figure 5.8: The build up of the deuterium concentration in the two Al 6061-T6 samples (open diamonds and closed circles) during Run 5. The spectra were collected during the bombardment of 200 keV deuterons to a fluence of 4.76×10^{16} D/cm^2. The fluence that is stated in the figure is the total deuterium implanted in the sample when the profile was taken.

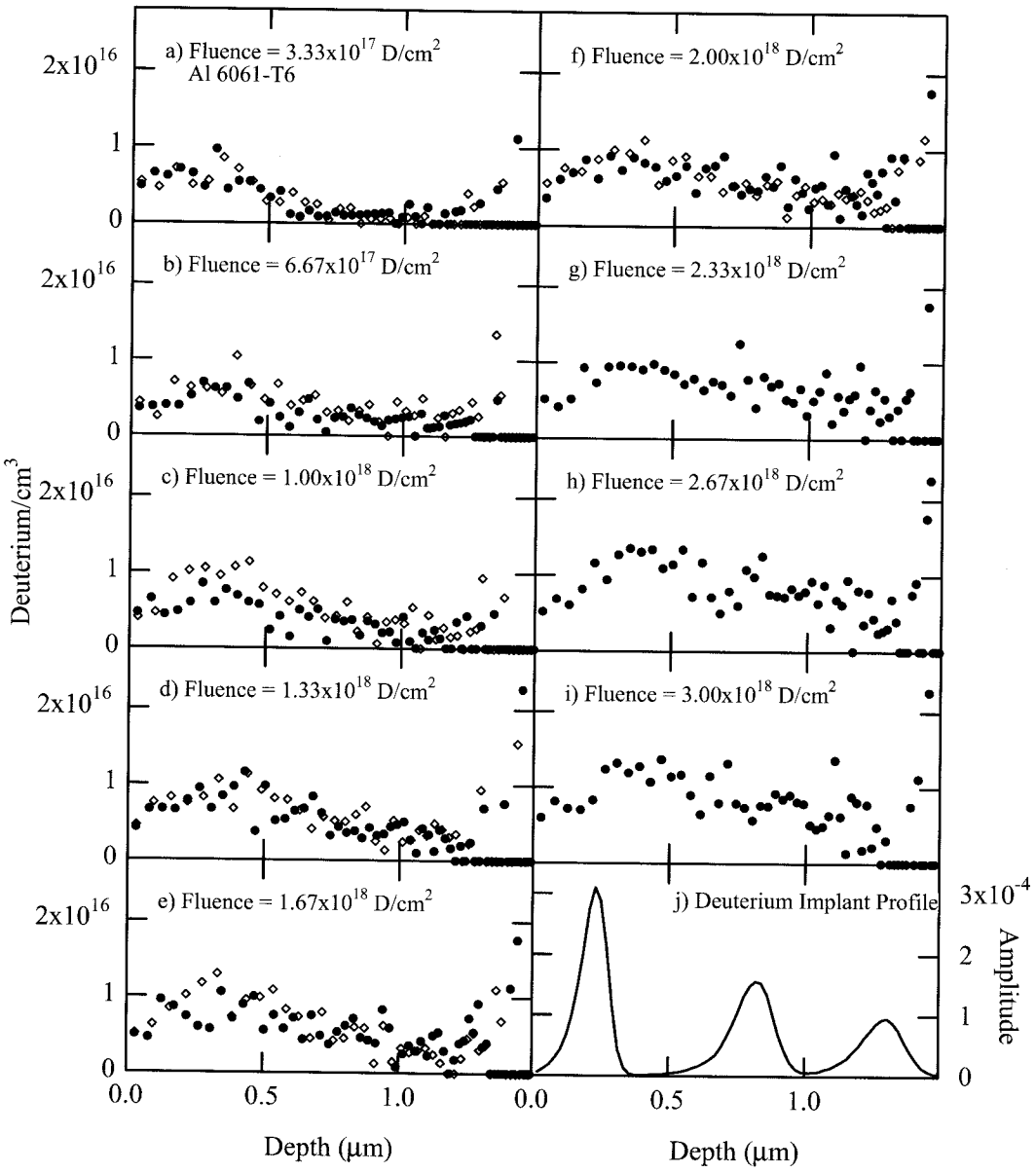

Figure 5.9: The build up of the deuterium concentration in the two Al 6061-T6 samples (open diamonds and closed circles) during Run 6. The spectra were collected during the bombardment of 200 keV deuterons to a fluence of 4.76×10^{16} D/cm^2. The fluence that is stated in the figure is the total deuterium implanted in the sample when the profile was taken.

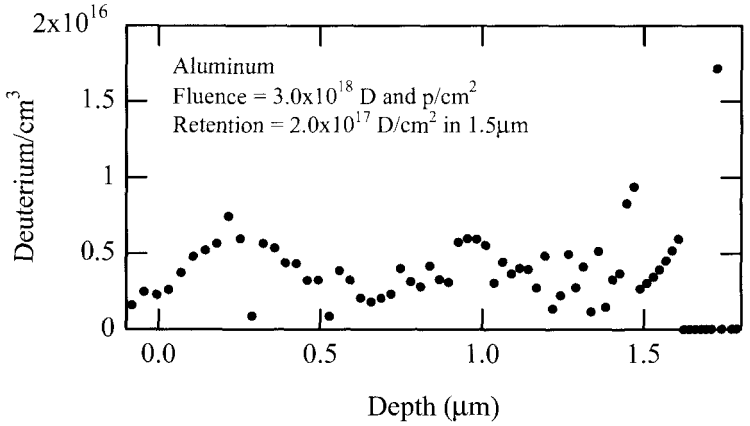

Figure 5.10: The deuterium concentration in the near surface of the front side of the Al 6061-T6 sample after the $5x10^{18}$ D and p/cm^2 implant of Run 6. The spectrum was collected during the bombardment of 650 keV ^{3}He ions to a fluence of $5x10^{15}$ He/cm^2. The measured deuterium retained is given.

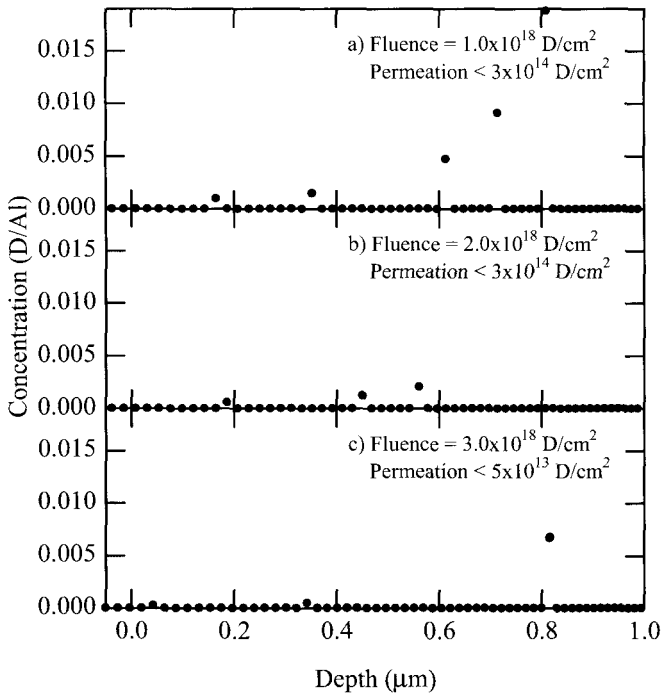

Figure 5.11: The deuterium concentration in the zirconium layer on the backside of the Al 6061-T6 sample during Run 6. The spectra were collected during the bombardment of 650 keV ^{3}He ions to a fluence of $5x10^{15}$ He/cm^2 in a) and b) and $1x10^{16}$ D/cm^2 in c) after each $1x10^{18}$ D (and p)/cm^2 implant cycle. The fluence that is stated in the figure is the total deuterium implanted in the sample when the profile was taken. No deuterium was measured in the Zr; the scatter in the plot is due to statistics. An upper limit to the deuterium permeation is given in the figure.

6 Copper coated Al 6061-T6

The copper coated Al 6061-T6 sample has been studied extensively. Copper coatings, prepared three different ways, were implanted during Runs 4, 5 and 6. All three coated samples retained much less deuterium than the Al 6061–T6 sample. During Run 4 the samples were implanted with deuterium up to a fluence of 3.04×10^{18} D/cm^2. The thermal desorption data for the copper coated Al 6061-T6 samples implanted during Run 4 are shown in Fig. 6.1. The spectra of the released HD and D_2 have a similar appearance. There is no clear indication from the released D_2 that bubbles or blisters were formed in the copper layer. Both an electroplated and an electroless electroplated sample were implanted during Run 5. The thermal desorption data for the electroless electroplated copper sample is shown in Fig. 6.2a-c). The addition of the proton implants resulted in a reduction in the release of D_2 from that in Run 4. The broad HD peak with limited D_2 supports the idea that bubbles and blisters are not formed as discussed in Chapter 5. The thermal desorption data for the electroplated copper coated Al 6061-T6 samples implanted during Run 5 are shown in Fig. 6.2d-f). No D_2 was released. The H_2 and HD spectra are very different from those of the electroless sample. This is due to the difference in the thickness of the copper coatings. The electroless electroplated copper layer is approximately 6 μm thick (see Fig. 6.6) whereas the electroplated copper layer is only 1 μm thick (see Fig. 6.8). A comparison of these two samples determines the importance of the thickness of the copper layer. A thick layer ensures that all of the implant damage occurs in the copper and provides a barrier for the migrating deuterium into the aluminum substrate. A thin coating may allow some implantation to occur directly into the aluminum substrate. In this case, the thin coating would provide an oxide free surface to enhance recombination, but would not be a migration barrier to the deuterium implanted directly into the aluminum. The thermal desorption results indicate that retention is significantly lower if the copper coating is thicker than the implant range of the deuterium.

The SEM images of the surface of the copper sample implanted during Run 4 shown in Fig. 6.3 show small changes in the surface resulting from the implantation, but no blisters. After the copper coating was applied, the surface was burnished. This produced two distinct surfaces, burnished and as-plated. In both regions, the implants appear to have etched or pitted the copper surface. Fig. 6.4 shows the copper coating to be approximately 4 μm thick. Fig. 6.5 shows the surface of the electroless electroplated sample implanted during Run 5. There are no obvious changes in the surface resulting from the implantation. However, the blister-like structures in Fig. 6.5 are identified as areas where the coating did not adhere to the substrate in Fig. 6.6b). The adhesion can be improved with the right parameters for the electroless electroplating process. Fig. 6.7 shows the very different surface of the electroplated copper coating implanted during Run 5. Again, there are not obvious signs of damage. There is possibly the same pitting as seen with the sample implanted during Run 4.

The nuclear reaction profiling data for the two copper coated Al 6061-T6 samples implanted during Run 5 is shown in Fig. 6.9. The near-surface deuterium concentration in both samples has not reached saturation (see Fig. 4.7). The deuterium concentration in the electroplated copper coating (1 μm thick) is low in the first 0.3 μm and increases around 0.5 μm indicating that the deuterium may be building up at the copper-substrate interface.

The helium profiling of the front surface of the electroless copper coated Al 6061-T6 sample implanted during Run 6, Fig. 6.10, shows that there is a high deuterium concentration at the surface of the sample. Thus, the deuterium is probably migrating to the surface where it is then trapped. This could be due to the build up of carbon during the implantation or an oxide layer. The $D(^3He,p)^4He$ profiling of the zirconium layer on the back surface of the sample shows that there is negligible amounts of deuterium permeating through up to a fluence of $3.0x10^{18}$ D/cm^2 (Fig. 6.11). The random scattering in the plots is due to statistics. The spectra between 0 and 0.8 μm were integrated and the results are listed in the figure as upper limits to the amount of permeated deuterium.

The copper coating greatly reduces the amount of retained deuterium from that of the Al 6061-T6. The importance of a coating thicker than the implant range of the deuterons is shown. The permeation measurements are encouraging as well.

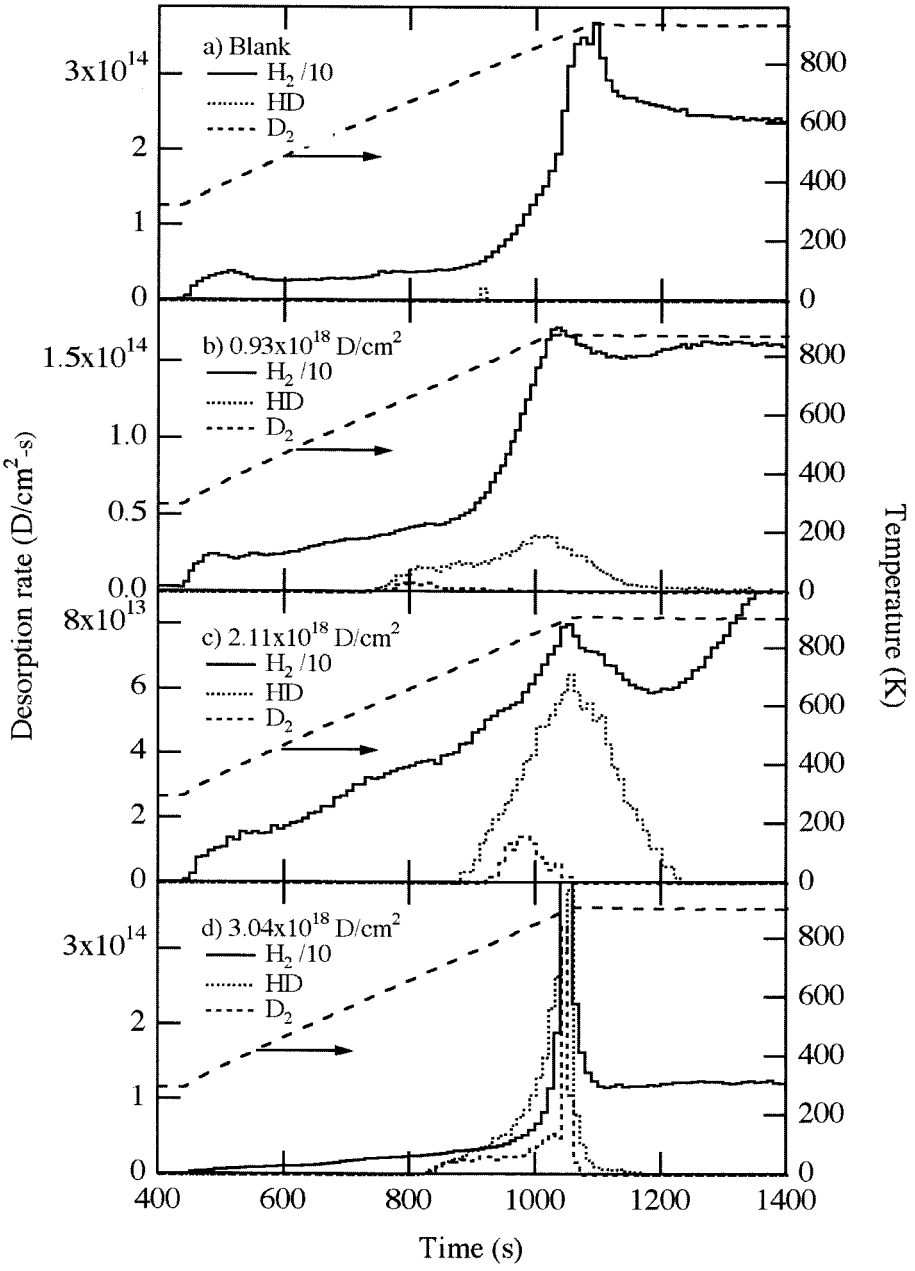

Figure 6.1: The thermal desorption spectra for the copper coated Al 6061-T6 samples implanted with b) 0.93x10^{18}, c) 2.11x10^{18}, and d) 3.04x10^{18} D/cm^2 during Run 4.

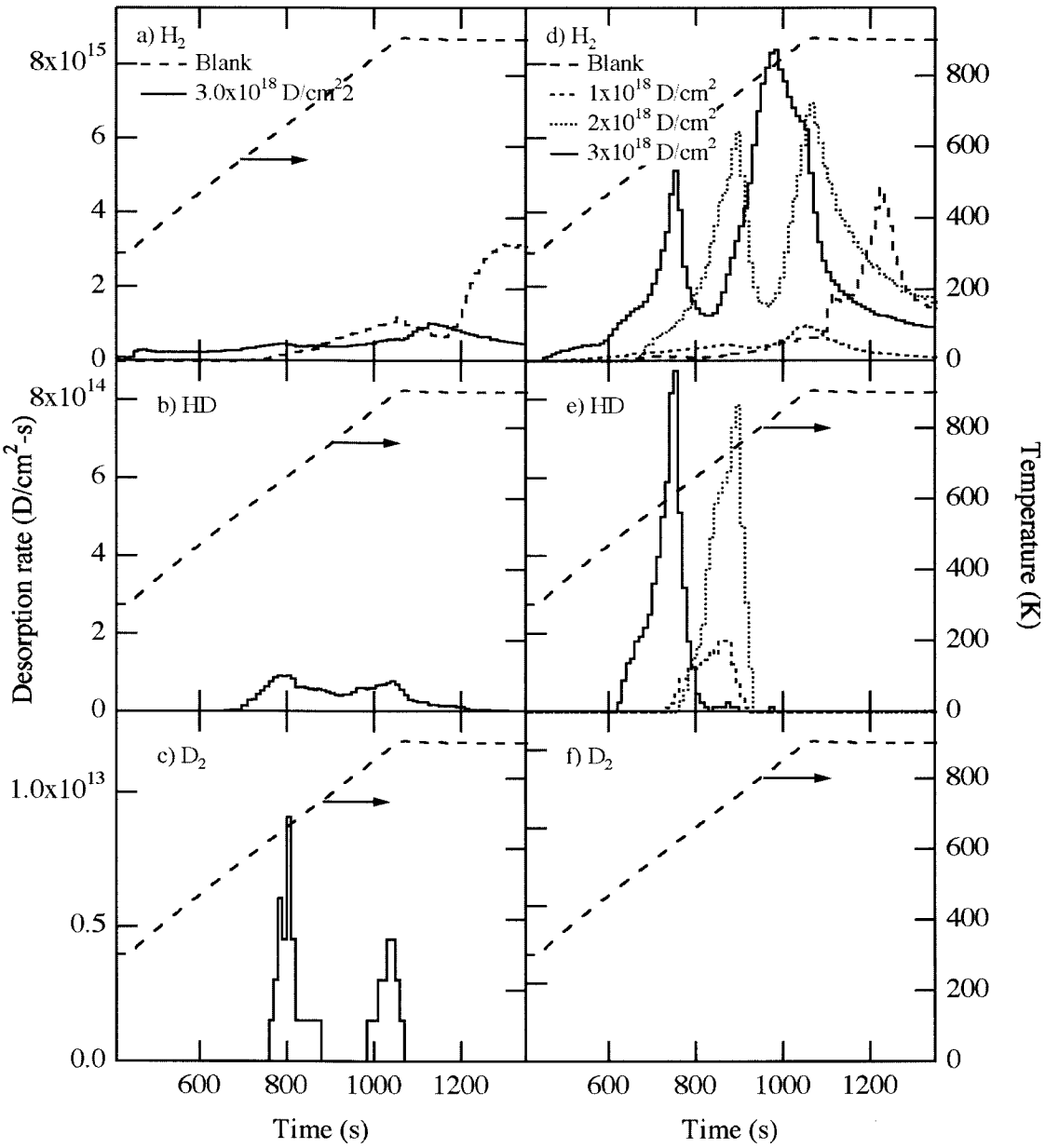

Figure 6.2: The thermal desorption spectra of H_2, HD, and D_2 for the electroless electroplated copper coated Al 6061-T6 sample (a-c) and the electroplated copper coated Al 6061-T6 sample (d-f) implanted with both protons and deuterons during Run 5. No D_2 was measured from any of the samples for the electroplated samples.

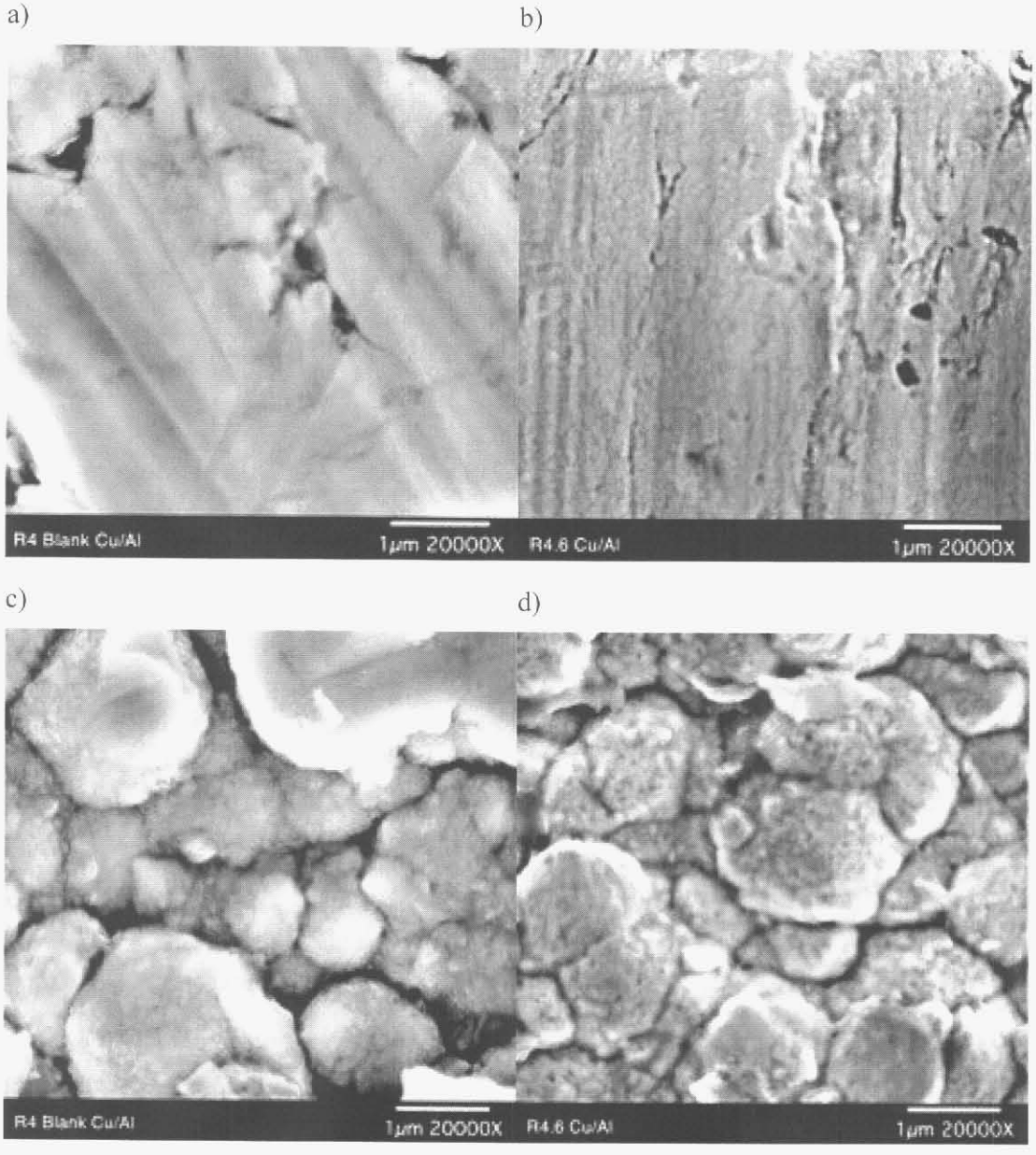

Figure 6.3: SEM images at 20,000X of the surface of the copper coated Al 6061-T6 samples before and after implantation to 3.04×10^{18} D/cm^2 in Run 4. The surface was burnished after the copper coating was applied creating two distinct surfaces. The burnished area imaged before implantation (a) and after implantation (b). The as-plated area imaged before implantation (c) and after implantation (d).

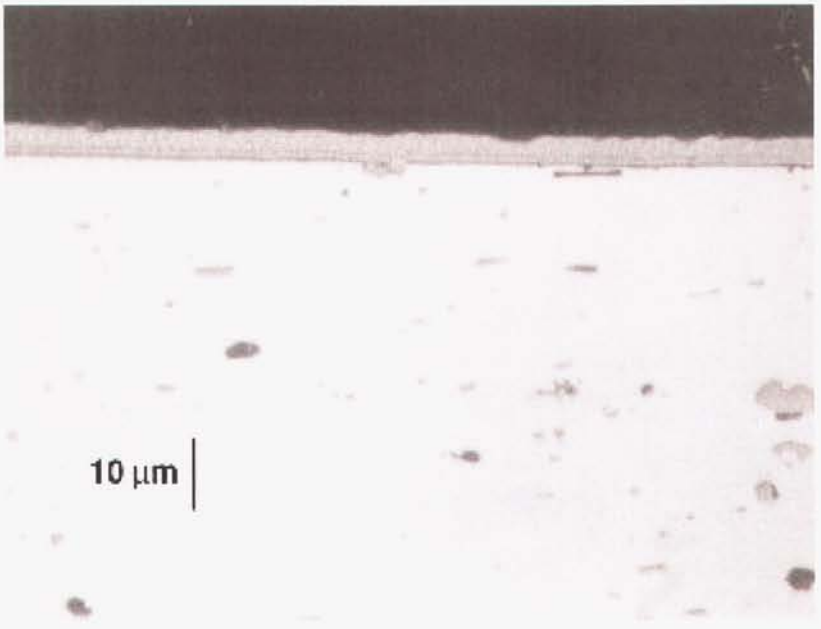

Figure 6.4: An optical image at 1000X of the cross section of the electroplated copper coated Al 6061-T6 sample before implantation during Run 4. The aluminum is on the bottom, the medium gray stripe is the 4 μm thick copper coating, and the dark area above the copper is the potting material.

a) b)

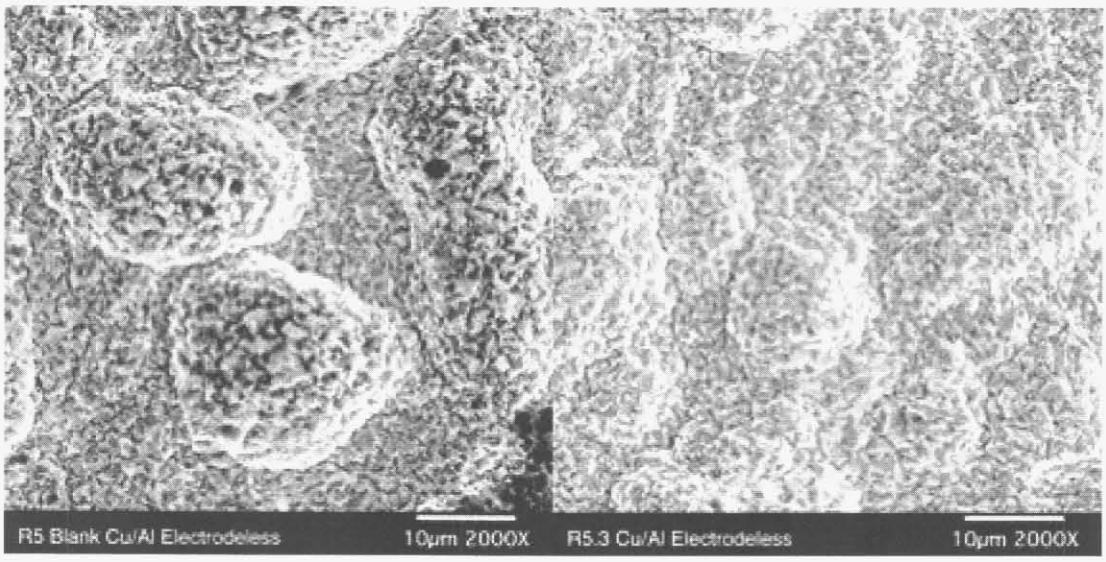

Figure 6.5: SEM images at 20,000X of the surface of the electroless electroplated copper coated Al 6061-T6 samples from Run 5. a) is before implantation and b) is after implantation with $3x10^{18}$ D/cm^2 and $3x10^{18}$ p/cm^2.

a) b)

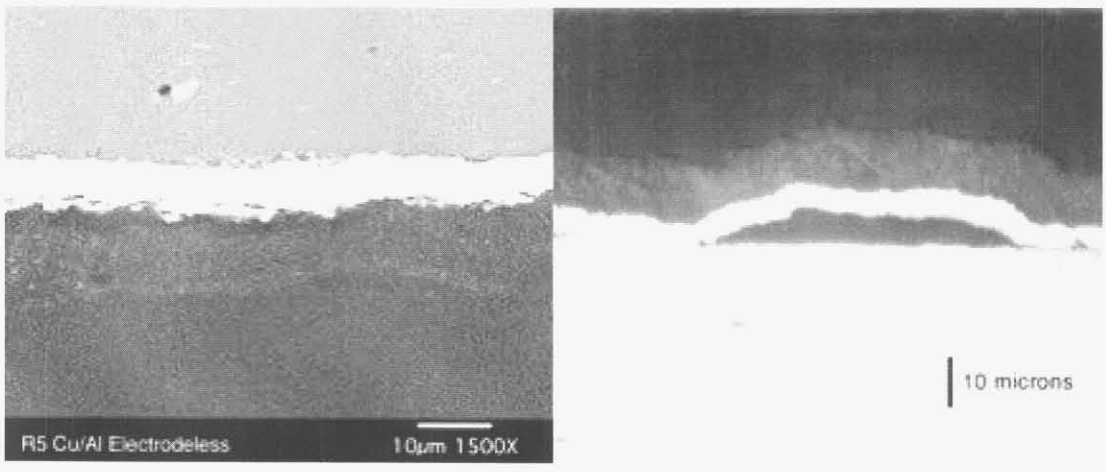

Figure 6.6: Cross section images of the electroless electroplated copper coated Al 6061-T6 sample before implantation during Run 5. a) is a SEM image at 1500X where the upper portion of the picture is aluminum, the light stripe is the 6 µm thick copper coating and the darker portion on the bottom is the potting material. b) is an optical image at 1000X. The aluminum is on the bottom, the light area is the copper, and the darker textured area above the copper is the potting material.

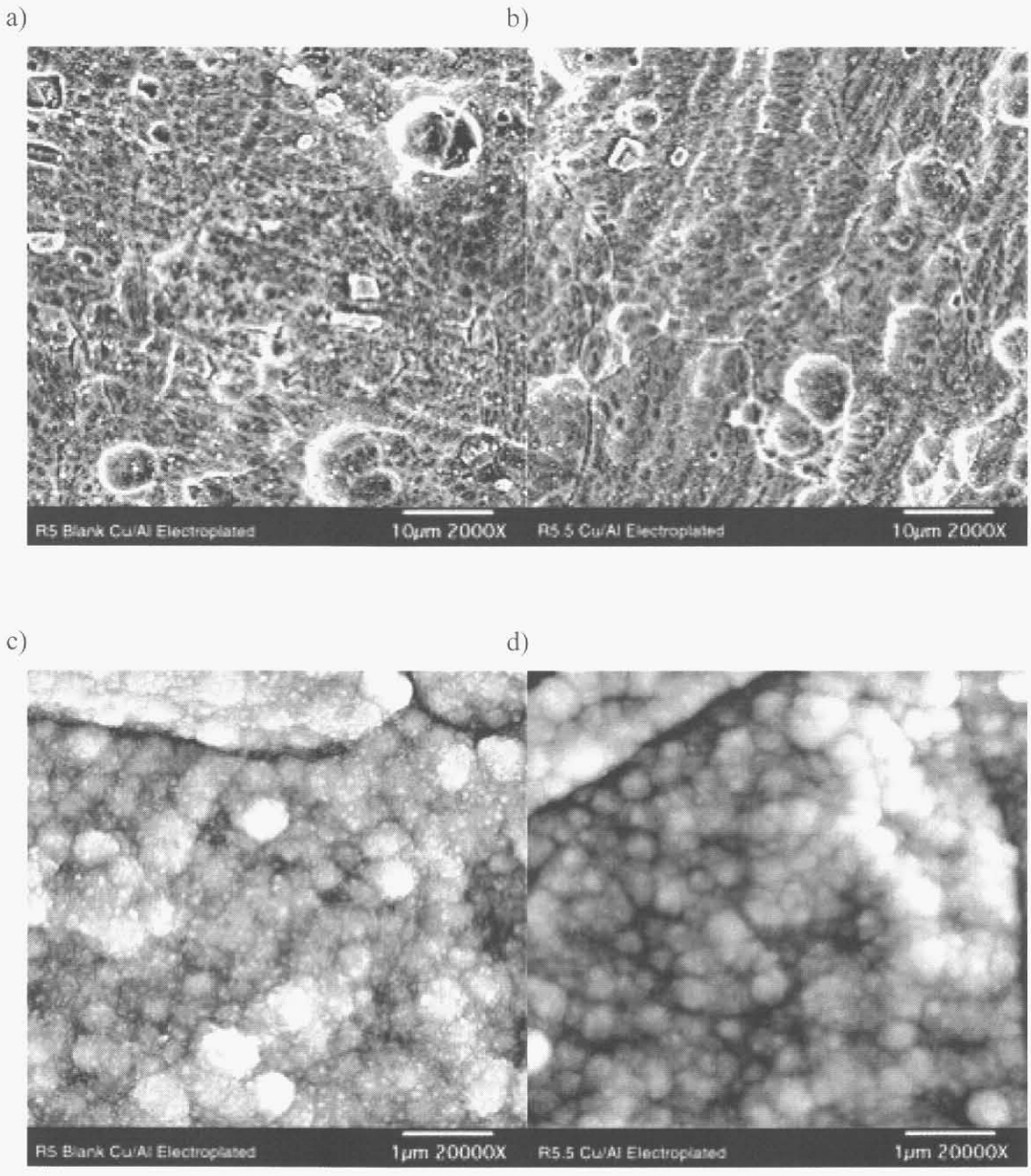

Figure 6.7: SEM images of the surface of the electroplated copper coated Al 6061-T6 sample before implantation at 2,000X (a) and at 20,000X (c) and after implantation of $3x10^{18}$ D/cm^2 and $3x10^{18}$ p/cm^2 at 2,000X (b) and 20,000X (d).

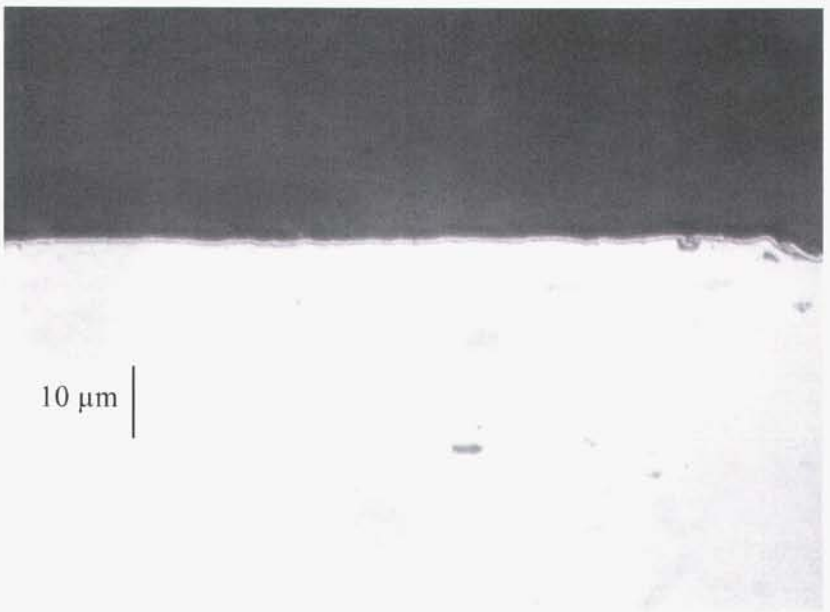

Figure 6.8: An optical image at 1000X of the cross section of the electroplated copper coated Al 6061-T6 sample before implantation during Run 5. The aluminum is on the bottom, the thin light area above the aluminum is the copper, and the darker textured area above the copper is the potting material.

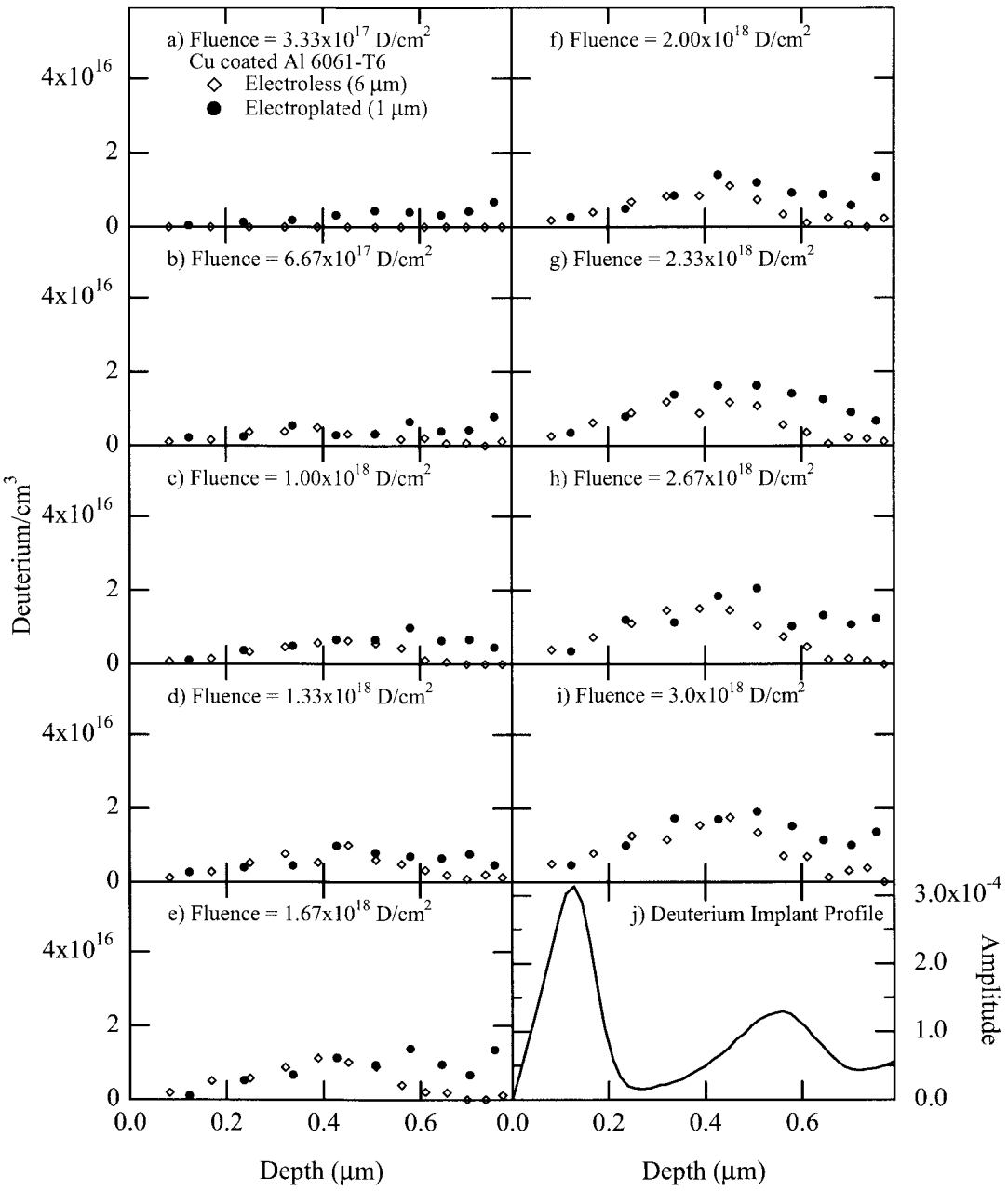

Figure 6.9: The build up of the deuterium concentration in the electroless electroplated copper (open diamonds) and the electroplated copper coated Al 6061-T6 sample (solid circles) during Run 5. The spectra were collected during the bombardment of 200 keV deuterons to a fluence of 4.76×10^{16} D/cm^2. The fluence that is stated in the figure is the total deuterium implanted in the sample when the profile was taken.

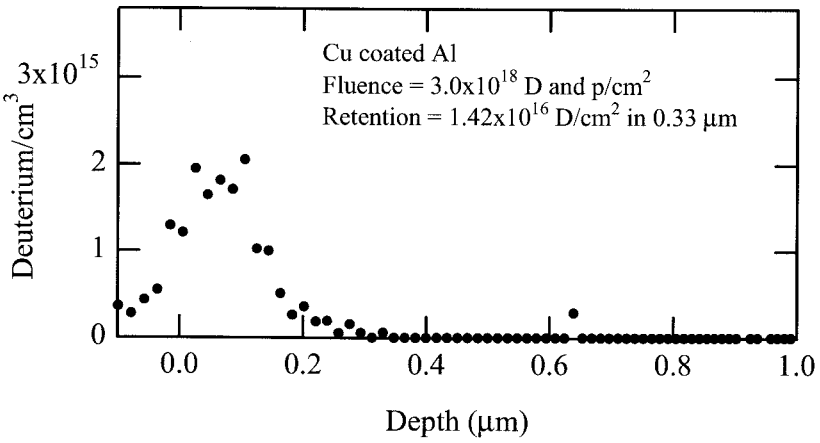

Figure 6.10: The deuterium concentration in the near surface of the front side of the copper coated Al 6061-T6 sample after the $5x10^{18}$ D and p/cm^2 implant of Run 6. The spectrum was collected during the bombardment of 650 keV ^{3}He ions to a fluence of $5x10^{15}$ He/cm^2. The measured deuterium retained is given.

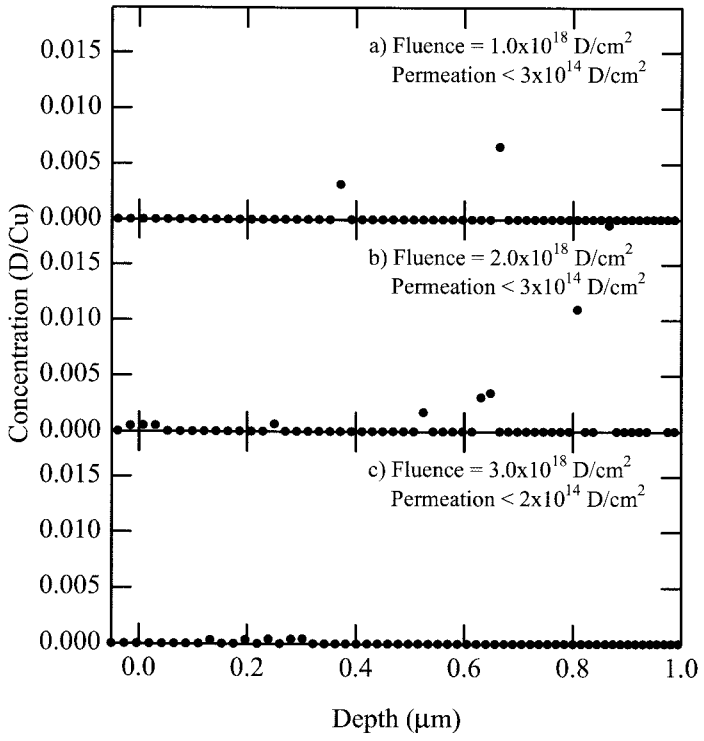

Figure 6.11: The deuterium concentration in the zirconium layer on the back side of the copper coated Al 6061-T6 sample during Run 6. The spectra were collected during the bombardment of 650 keV ^{3}He ions to a fluence of $5x10^{15}$ He/cm^2 in a) and b) and $1x10^{16}$ D/cm^2 in c) after each $1x10^{18}$ D (and p)/cm^2 implant cycle. The fluence that is stated in the figure is the total deuterium implanted in the sample when the profile was taken. No deuterium was measured in the Zr; the scatter in the plot is due to statistics. An upper limit to the deuterium permeation is given in the figure.

Intentionally Left Blank

7 Nickel coated Al 6061-T6

Nickel coated Al 6061-T6 samples were implanted with protons and deuterons during Run 5 and 6; they were not included in the earlier runs. The experimental results for the nickel coated Al 6061-T6 samples are very promising. The application of an electroless nickel coating is a well understood process and easier to control than the electroless electroplating copper process. The thermal desorption spectra for the released H_2 from the sample implanted during Run 5 is shown in Fig. 7.1. The large H_2 release from the sample implanted with $2.0x10^{18}$ D/cm^2 is not understood. No deuterium was released as HD or D_2.

The SEM images of the nickel surface up to 20,000X resolution show no visible change in the metal due to the proton and deuteron implants. SEM images of the surface before and after implantation at 2000X are shown in Fig. 7.2. A SEM image and an optical image of the cross section of the nickel coating before implantation are shown in Fig. 7.3. The coating is approximately 8 μm thick.

The nuclear reaction profiling of the near surface deuterium build up during Run 5 in Fig. 7.4 reveals small amounts of deuterium building up in the near surface region during the implantation. This concentration does not appear to have reached saturation. The absence of deuterium in the TDS spectra indicates that the deuterium is released, possibly by the implantation of the protons after the deuterons. The nuclear reaction profiling of the sample implanted during Run 6, Fig. 7.5, shows similar results. The concentration of deuterium in the near surface continues to increase. The helium profiling of the front surface after the final implantation of $3.0x10^{18}$ D (and p)/cm^2 during Run 6 shows that the deuterium is trapped at the surface (see Fig. 7.6). This is similar to the results for the copper coated Al 6061-T6 sample. Again, this could be due to the build up of carbon at the surface during implantation or any oxide on the surface. The D(^{3}He,p)^{4}He profiling of the zirconium layer on the back surface of the nickel coated Al 6061-T6 sample implanted during Run 6 is shown in Fig. 7.7. No deuterium permeated through to the outer surface up to a fluence of $3.0x10^{18}$ D (and p)/cm^2.

The nickel coating reduces the amount of retained and permeated deuterium to negligible amounts. Based on these results, nickel coated Al 6061-T6 appears to be a strong candidate for the structure of the APT tubes.

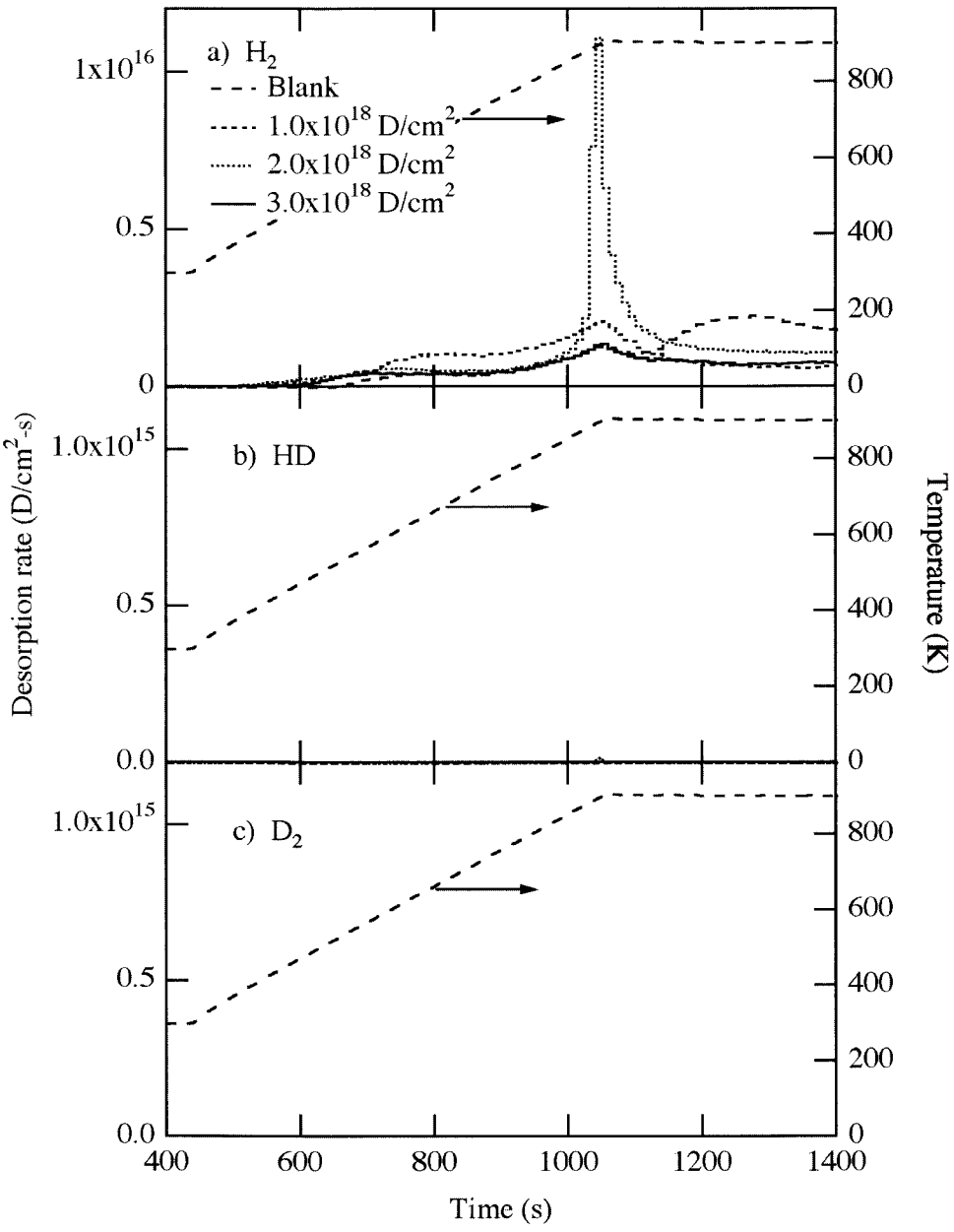

Figure 7.1: The thermal desorption spectra of a) H_2, b) HD, and c) D_2 for the electroless electroplated nickel coated Al 6061-T6 sample implanted with both protons and deuterons during Run 5. There was no HD or D_2 released during the desorption.

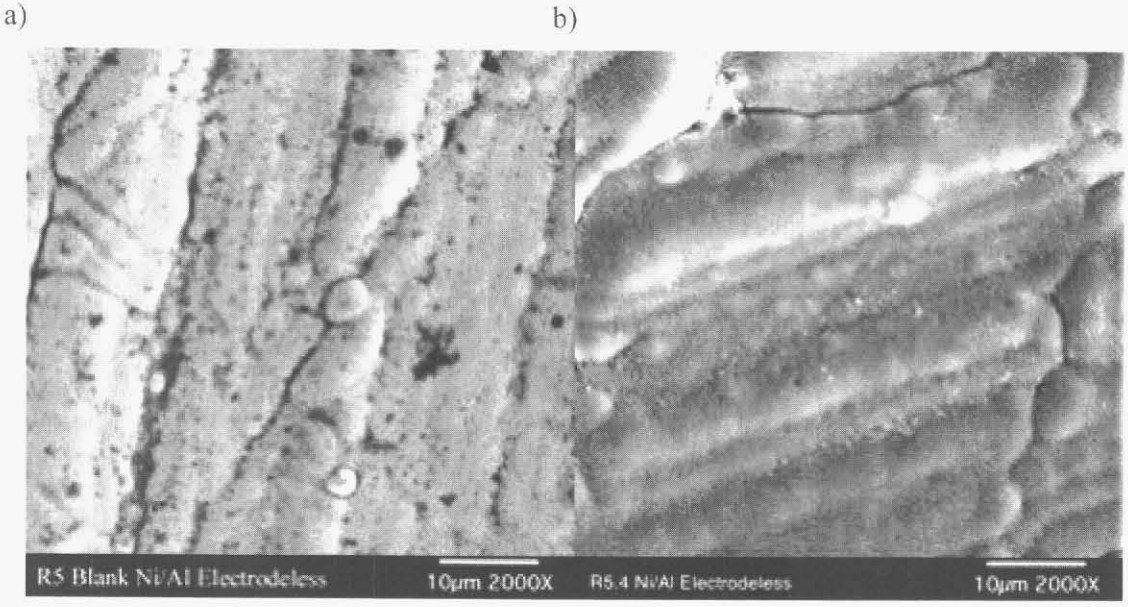

Figure 7.2: SEM images at 2000X of the Ni coated Al 6061-T6 sample a) before and b) after the implantation of $3.0x10^{18}$ D/cm^2 and $3.0x10^{18}$ p/cm^2 during Run 5. The surface shows no visible damage due to the implantation here and at higher magnifications.

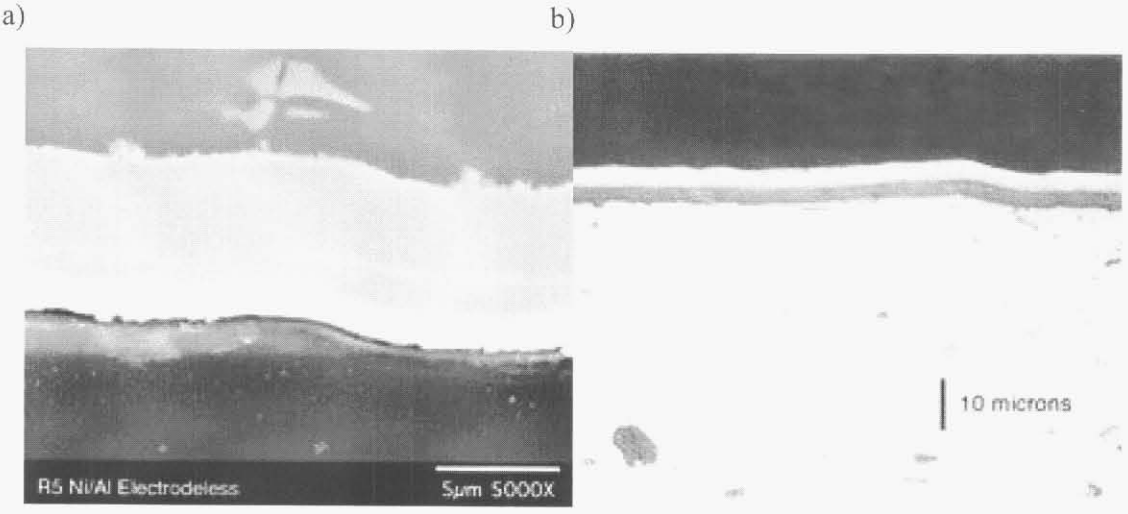

Figure 7.3: Cross section images of the electroless electroplated nickel coated Al 6061-T6 sample before implantation during Run 5. a) is a SEM image at 5000X where the upper portion of the picture is aluminum, the light stripe is the 8 μm thick nickel coating and the darker portion on the bottom is the potting material. b) is an optical image at 1000X of the nickel coated aluminum sample. The aluminum is on the bottom, and the darker area on the top is the potting material. The nickel appears as two very distinct layers, unlike the SEM image.

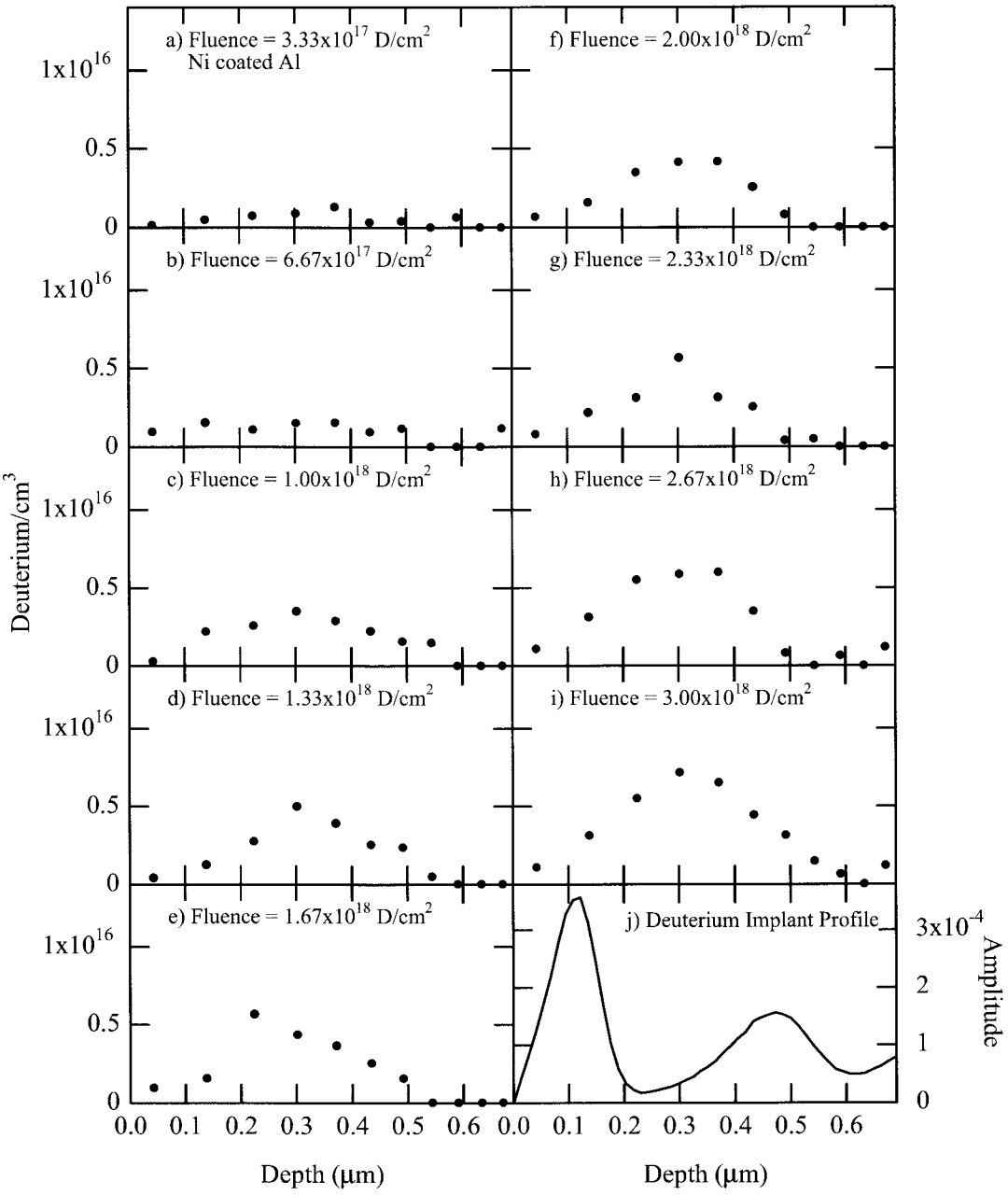

Figure 7.4: The build up of the deuterium concentration in the nickel coated Al 6061-T6 sample during Run 5. The spectra were collected during the bombardment of 200 keV deuterons to a fluence of 4.76×10^{16} D/cm^2. The fluence that is stated in the figure is the total deuterium implanted in the sample when the profile was taken.

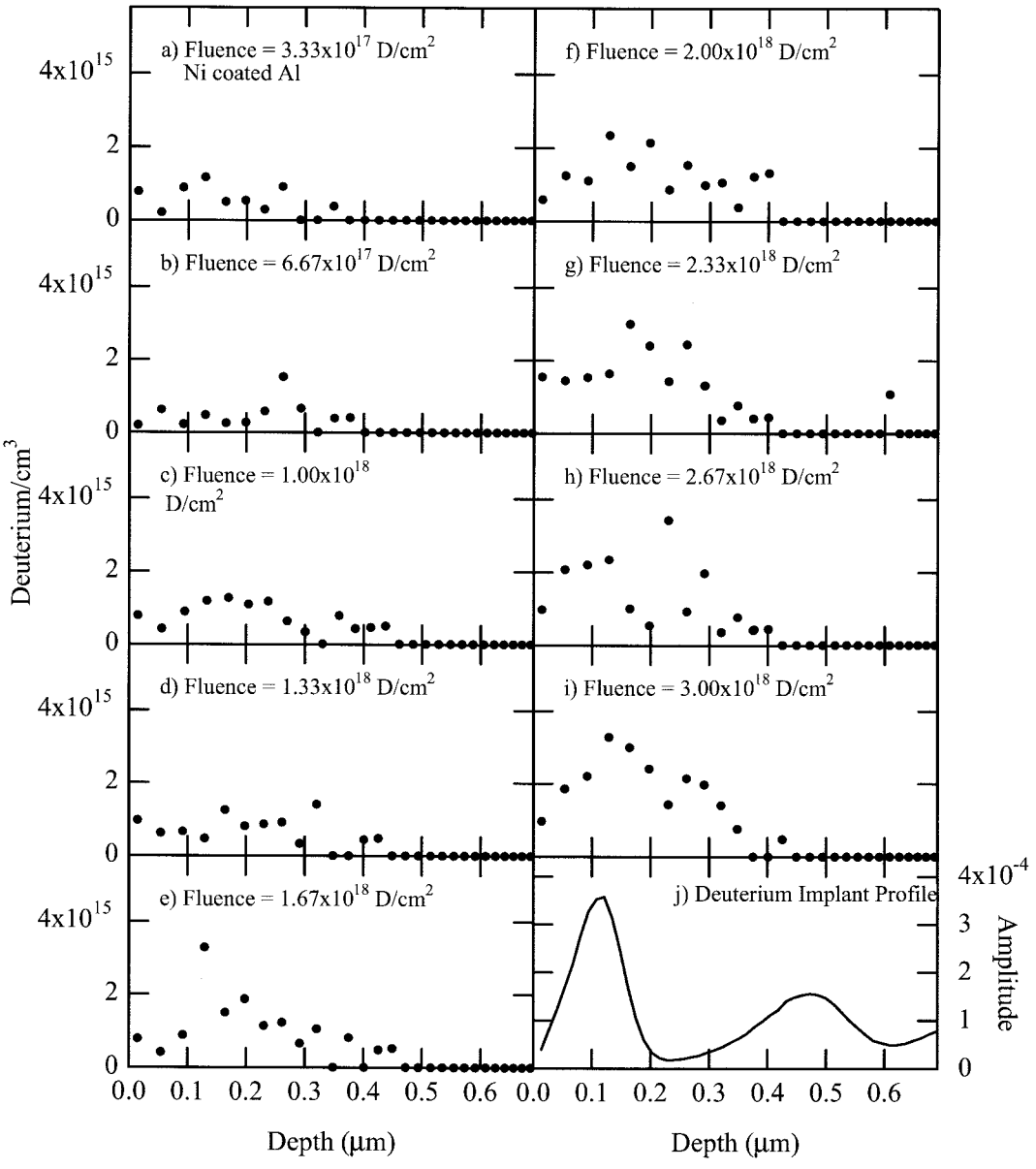

Figure 7.5: The build up of the deuterium concentration in the nickel coated Al 6061-T6 sample during Run 6. The spectra were collected during the bombardment of 200 keV deuterons to a fluence of 4.76×10^{16} D/cm^2. The fluence that is stated in the figure is the total deuterium implanted in the sample when the profile was taken.

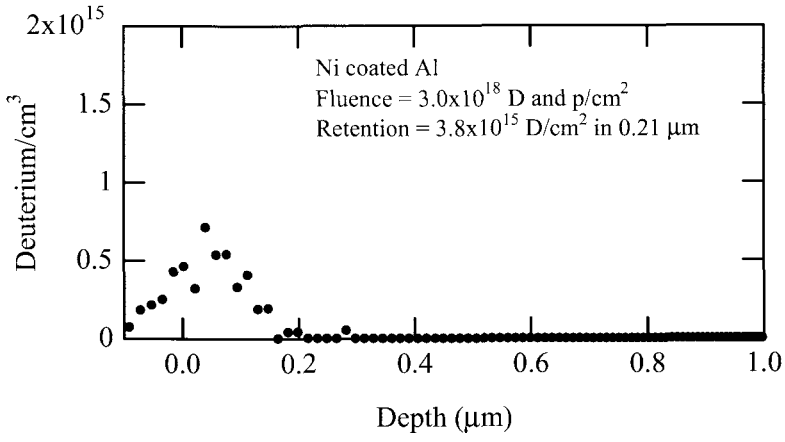

Figure 7.6: The deuterium concentration in the near surface of the front side of the nickel coated Al 6061-T6 sample after the $5x10^{18}$ D and p/cm^2 implant of Run 6. The spectrum was collected during the bombardment of 650 keV ^{3}He ions to a fluence of $5x10^{15}$ He/cm^2. The measured deuterium retained is given.

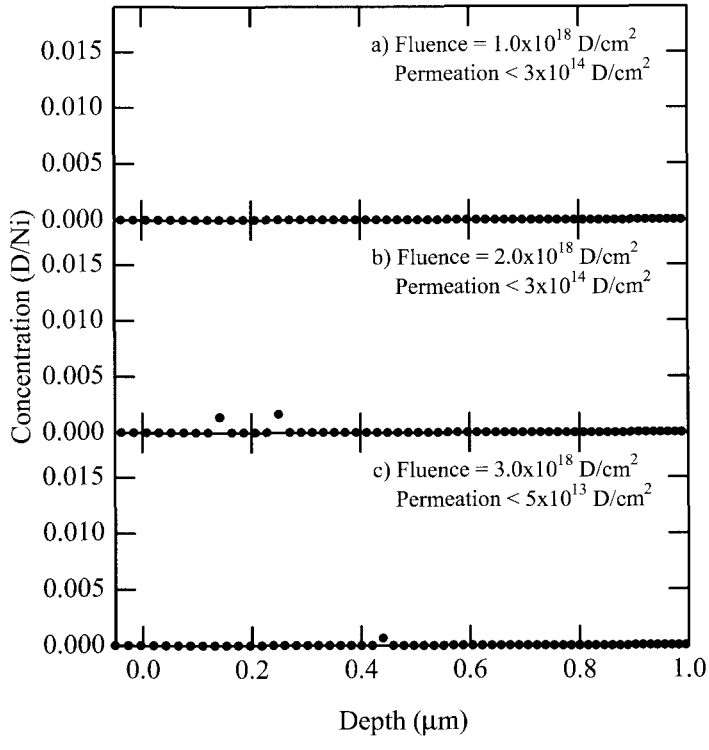

Figure 7.7: The deuterium concentration in the zirconium layer on the backside of the nickel coated Al 6061-T6 sample during Run 6. The spectra were collected during the bombardment of 650 keV ^{3}He ions to a fluence of $5x10^{15}$ He/cm^2 in a) and b) and $1x10^{16}$ D/cm^2 in c) after each $1x10^{18}$ D (and p)/cm^2 implant cycle. The fluence that is stated in the figure is the total deuterium implanted in the sample when the profile was taken. No deuterium was measured in the Zr; the scatter in the plot is due to statisitics. An upper limit to the deuterium permeation is given in the figure.

8 Anodized Aluminum 6061-T6

An Al 6061-T6 sample with and anodized surface layer was included in the matrix of Run 5. The porosity of anodized aluminum may promote the release of deuterium and, therefore, reduce permeation as well. Song *et. al.* [52] studied the permeation of hydrogen through various oxide coatings on aluminum. They found that the oxide layers did serve as permeation barriers. However, they concluded that the anodized aluminum had less of a barrier effect than other oxide layers. Song's experiments were performed with the vapor phase permeation technique, not with implanted hydrogen. The implantation of hydrogen directly into the bulk can cause important differences in retention and permeation results.

The thermal desorption spectra for H_2 and various water and methane molecules (masses 16, 17, 18, and 19) are shown in Fig. 8.1. The deuterium retained in the anodized aluminum was released as HDO (mass 19) during TDS. The samples were washed with ethanol before thermal desorption; the ethanol cracking pattern allows mass 19 as well. The mass 19 that was released at lower temperatures is due to the ethanol and the higher temperature release is due to HDO. This mass 19 peak was not seen in the thermal desorption spectra of the other samples. The amount of deuterium retained within the sample is similar to that of the bare aluminum sample (Fig. 4.7) and does not appear to have reached saturation. The nuclear reaction profiling data shown in Fig. 8.2 confirms that a steady-state has not been reached. The near-surface deuterium concentration measured by NRP is much greater in the anodized aluminum than the bare aluminum (Fig. 4.1). This suggests that during implantation a high concentration of deuterium builds up in the anodized layer, but is released before thermal desorption. The release could be promoted by the anodized layer or by the proton implantation that followed the deuteron implants. The anodized layer does not reduce the overall retention compared to bare aluminum.

It was not possible to take SEM images of the implanted anodized aluminum samples, therefore only images of the sample before implantation are shown in Fig. 8.3. The porosity of the anodized layer is very clear. An optical image of the cross section of the anodized aluminum layer is shown in Fig. 8.4. The anodized layer is approximately 17 μm thick.

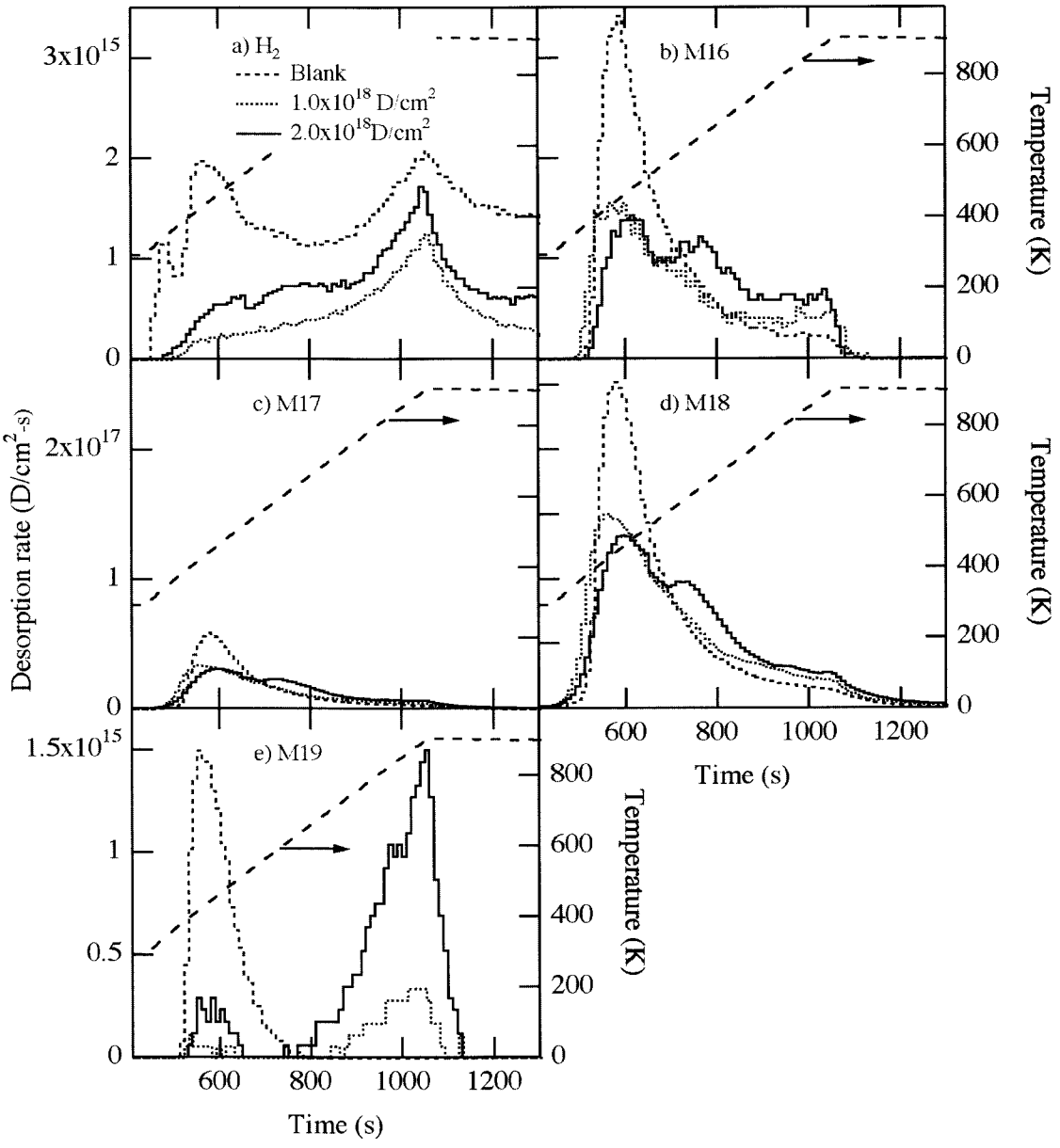

Figure 8.1: The thermal desorption spectra of a) H_2, b) mass 16, c) mass 17, d) mass 18 and e) mass 19 for the anodized aluminum samples implanted with both protons and deuterons during Run 5. The deuterium was desorbed as HDO (mass 19) only, no HD or D_2 was measured. The lower peak in the mass 19 spectra is attributed to ethanol used to wash the samples, whereas the higher temperature peak is attributed to HDO.

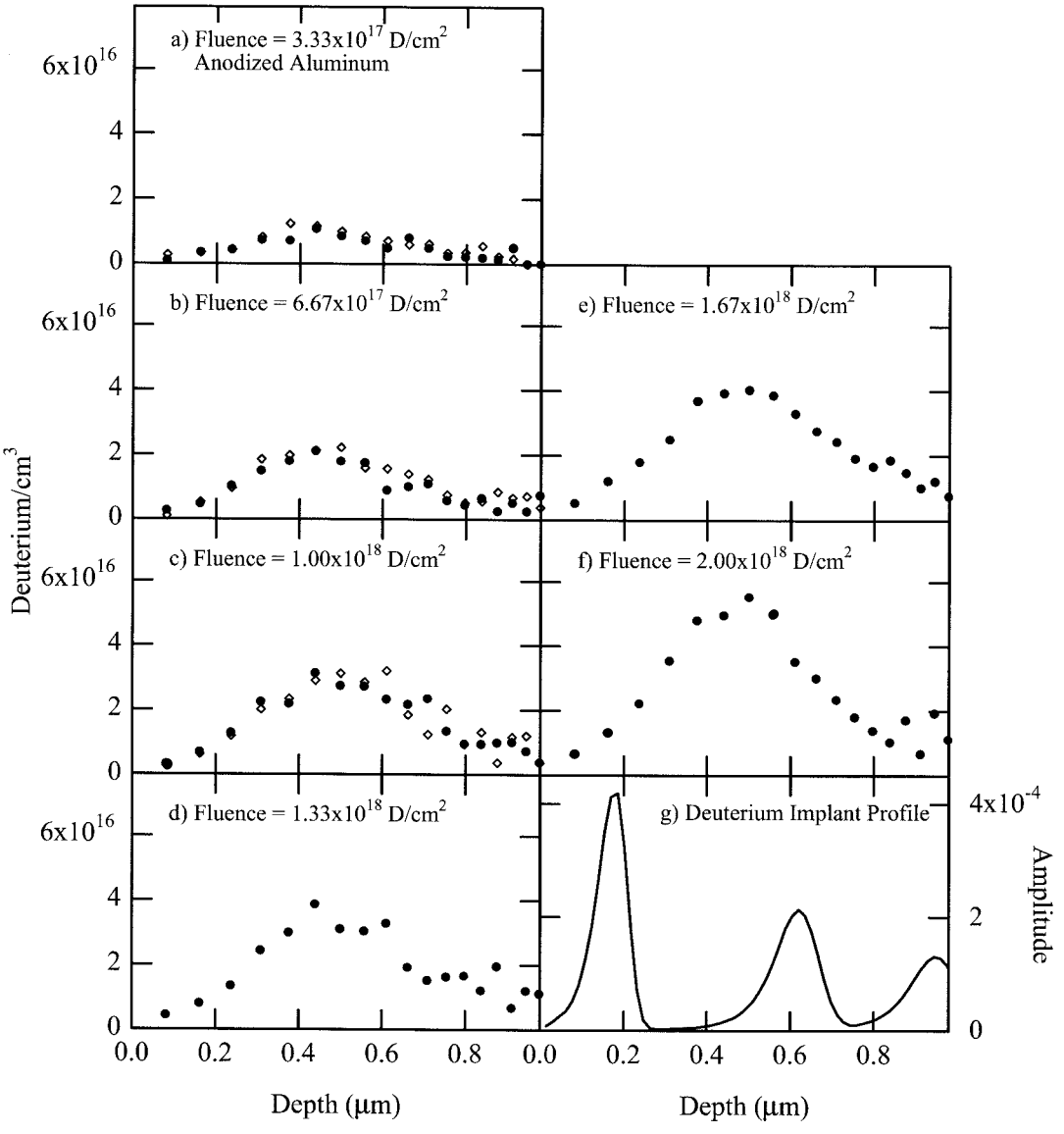

Figure 8.2: The build up of the deuterium concentration in the two anodized aluminum samples (open diamonds and closed circles) during Run 5. The spectra were collected during the bombardment of 200 keV deuterons to a fluence of 4.76×10^{16} D/cm^2. The fluence that is stated in the figure is the total deuterium implanted in the sample when the profile was taken.

a) b)

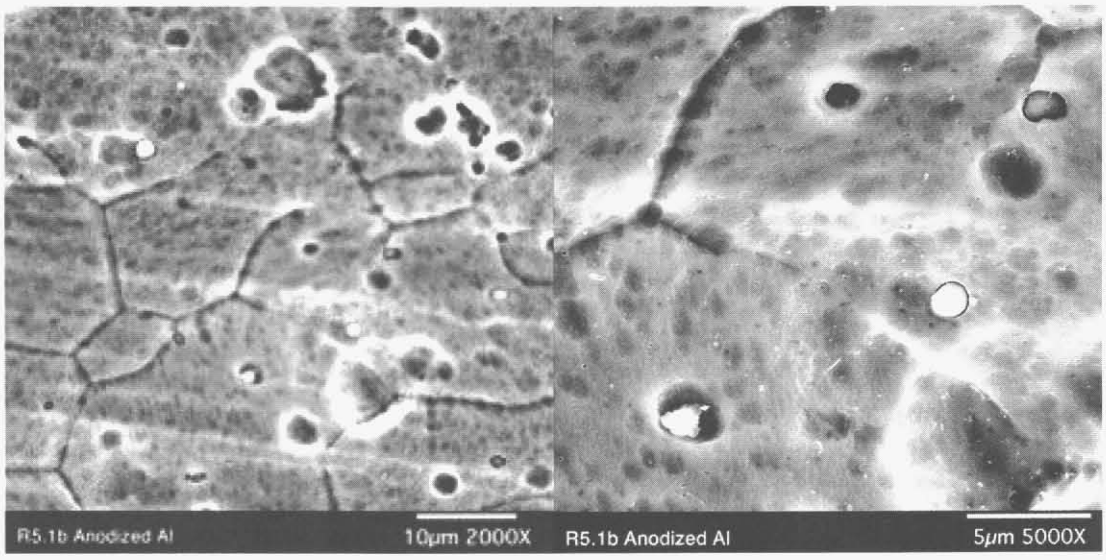

Figure 8.3: SEM images of the anodized aluminum sample at a) 2000X and b) 5000X before implantation. It was not possible to take SEM images of the implanted sample due to charging.

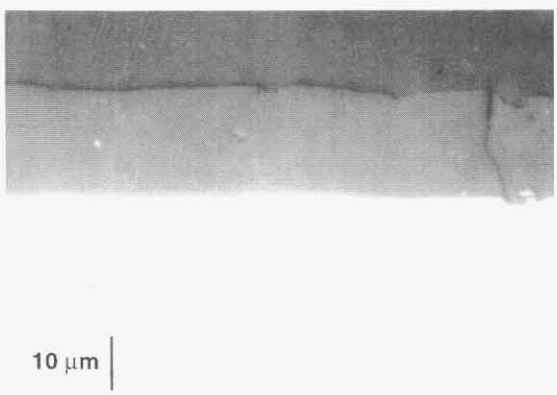

Figure 8.4: An optical image at 1000X of the cross section of the anodized aluminum sample before implantation during Run 5. The aluminum is on the bottom, the medium gray section is the anodized aluminum, and the dark area on top is the potting material.

9 Stainless Steel 316L

Aluminum tubes are somewhat difficult to weld with high integrity, and this prompted the investigation of thin-walled SS 316L as a possible APT tube material. SS 316L was included in Run 4, multi-energy deuteron implant, and Run 6, multi-energy deuteron and proton implant. The thermal desorption spectra for the samples implanted during Run 4 are shown in Fig. 9.1. The sample implanted to a fluence of 0.93×10^{18} D/cm^2 was heated to 873 K during the first ramp, Fig. 9.1a). It was then decided that the SS 316L samples should be ramped to 1273 K to insure the release of all the retained deuterium. Therefore, the sample was reheated to 1273 K. Fig. 9.1b) shows the release of some more HD at the higher temperatures. The high solubility and low defect binding energy of hydrogen in stainless steel does not favor bubble precipitation. The broad HD and D_2 peaks are consistent with the idea that the retained deuterium migrates to the surface where it recombines to form molecules and is released. If bubbles formed, narrow peaks would result from the deuterium release when the bubbles broke. The thermal desorption spectra for the samples implanted during Run 6 are shown in Fig. 9.2. Again, the amount of deuterium released as D_2 is considerably reduced, probably due to the implant of protons after the deuterons.

The SEM images shown in Fig. 9.3 of the sample surface both before and after the deuterium implantation reveal no obvious changes, such as surface blisters, in the metal. As indicated above, this was expected for SS 316L at the fluxes used in this experiment.

The D(d,p)T nuclear reaction profiling of the near surface during the deuteron implantation of the sample during Run 6 is shown in Fig. 9.4. There is a steady increase in the amount of measured deuterium. The front surface of the sample was profiled with the D(^{3}He,p)^{4}He profiling technique after the final implantation to a fluence of 5.0×10^{18} D (and p)/cm^2. Fig. 9.5 shows that the deuterium concentration is on the surface as is expected. The high mobility of deuterium in stainless steel and the low recombination rate for deuterium on the stainless steel surface would cause the deuterium to build-up at the surface. The most interesting result for the SS 316L is the D(^{3}He,p)^{4}He profiling of the zirconium layer on the back surface of the sample shown in Fig. 9.6. The profiling of the zirconium layer shows that deuterium permeated through to the outside surface. After an implant fluence of 5.0×10^{18} D (and p)/cm^2 was reached, 2.13×10^{16} D/cm^2 was measured in the zirconium.

The stainless steel sample retained a little less deuterium than the aluminum sample, but more than the coated aluminum samples. However, the stainless steel sample does show high amounts of deuterium permeation, a costly problem for APT.

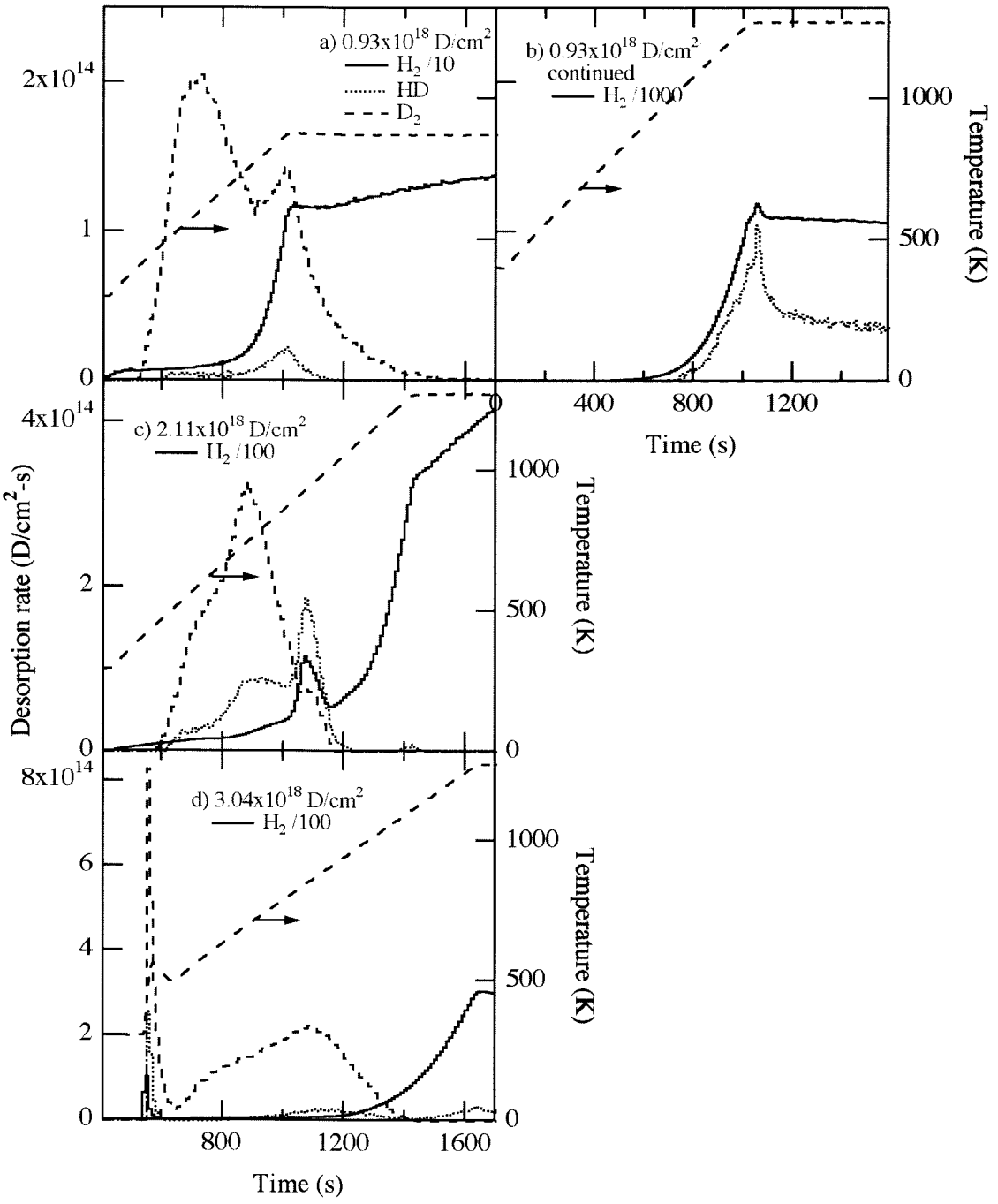

Figure 9.1: The thermal desorption spectra for the stainless steel sample implanted with deuterons to a flux of a-b) 0.93×10^{18}, c) 2.11×10^{18} and d) 3.04×10^{18} D/cm^2 during Run 4. The temperature was ramped to 873 K in a), then a second ramp to 1273 K was completed and is shown in b). In d) the ramp increased too quickly during the beginning of the desorption of the 3.04×10^{18} D/cm^2 sample.

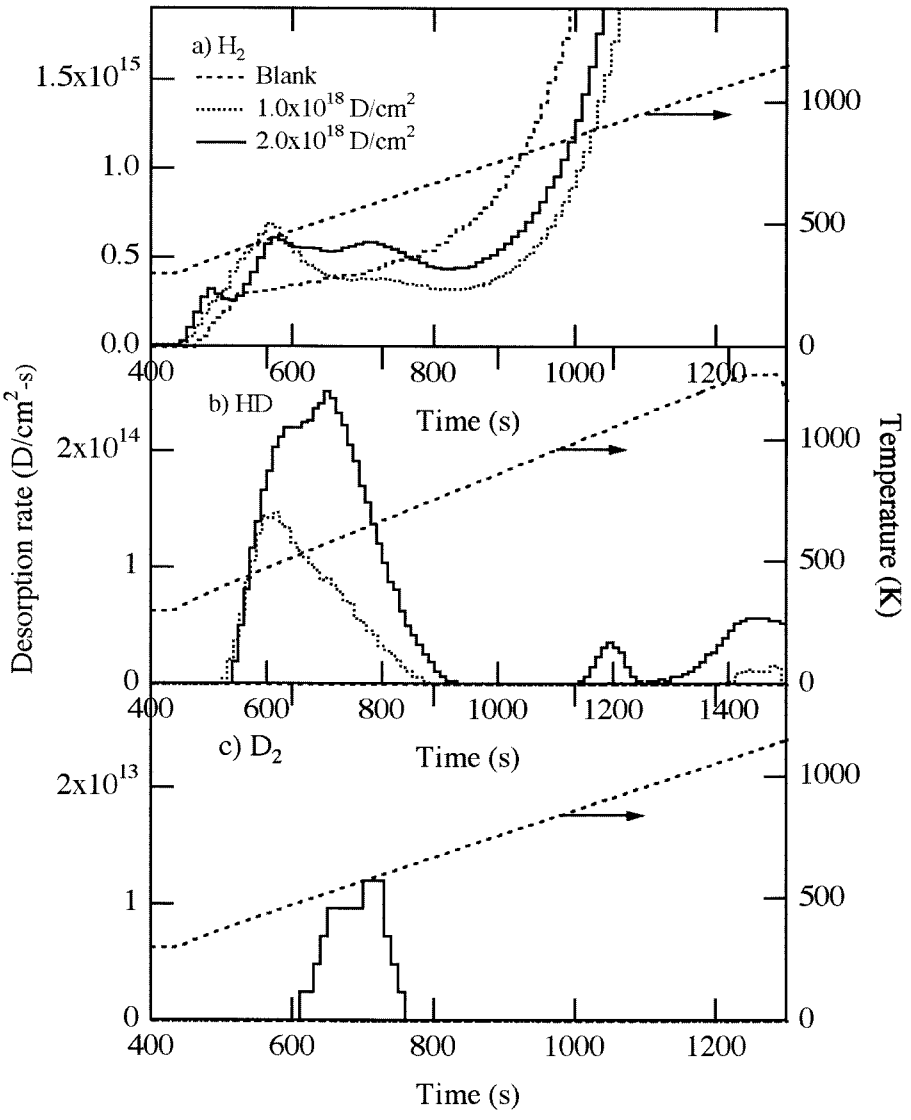

Figure 9.2: The thermal desorption spectra for a) H_2, b) HD, and c) D_2 for the stainless steel sample implanted with deuterons to a flux of 1.0x10^{18}, 2.0x10^{18} and 3.0x10^{18} D (and p)/cm^2 during Run 6.

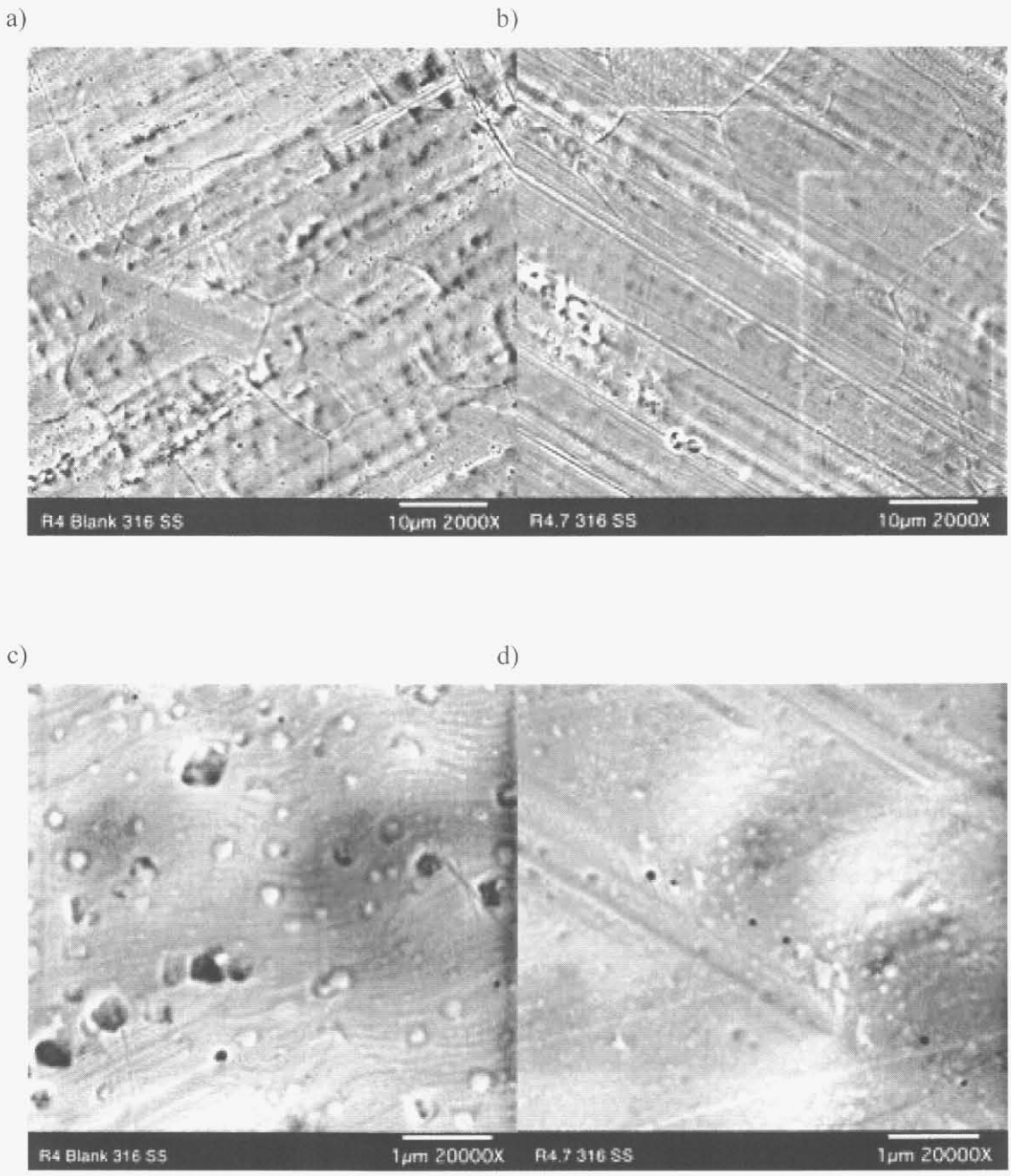

Figure 9.3: SEM images at 2,000X of the stainless steel sample used in Run 4 a) before implantation and b) after the implantation of 3.04×10^{18} D/cm^2. SEM images at 20,000X c) before implantation and d) after the implantation of 3.04×10^{18} D/cm^2. There is no visible difference in the samples due to implantation.

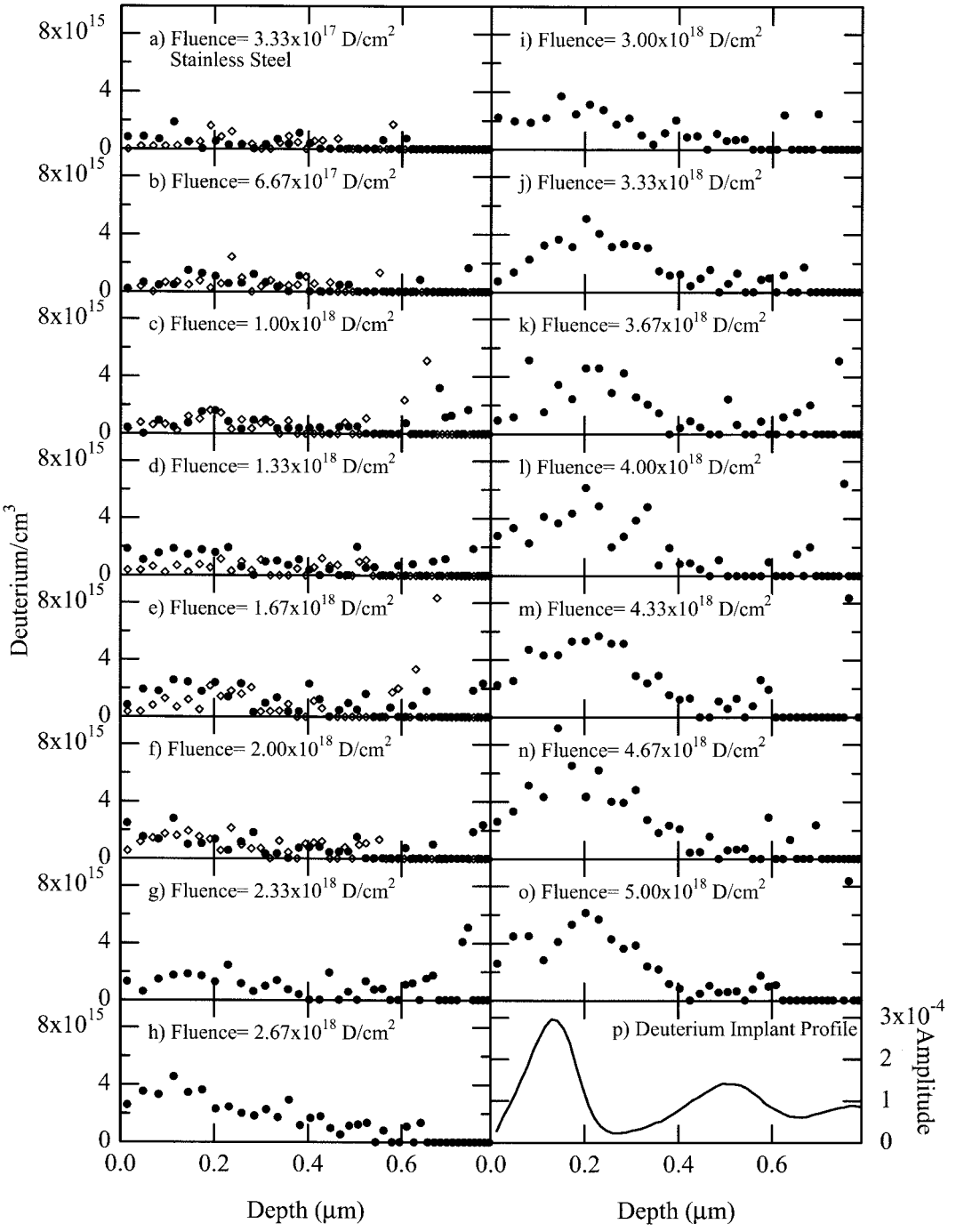

Figure 9.4: The build up of the deuterium concentration in the stainless steel sample implanted during Run 6. The spectra were collected during the bombardment of 200 keV deuterons to a fluence of 4.76×10^{16} D/cm^2. The fluence that is stated in the figure is the total deuterium implanted in the sample when the profile was taken. a-f) show profiles from two stainless steel samples implanted during the run.

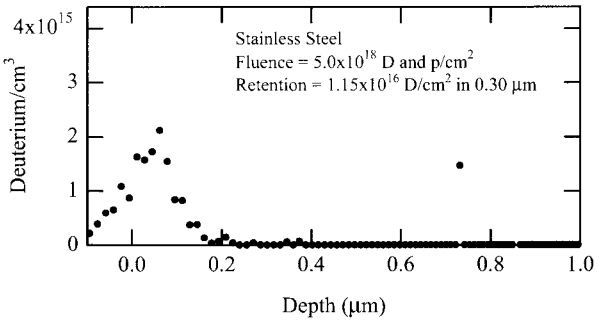

Figure 9.5: The deuterium concentration in the near surface of the front side of the stainless steel sample after the $5x10^{18}$ D and p/cm^2 implant of Run 6. The spectrum was collected during the bombardment of 650 keV ^{3}He ions to a fluence of $5x10^{15}$ He/cm^2. The retained deuterium is calculated by integrating the deuterium concentration.

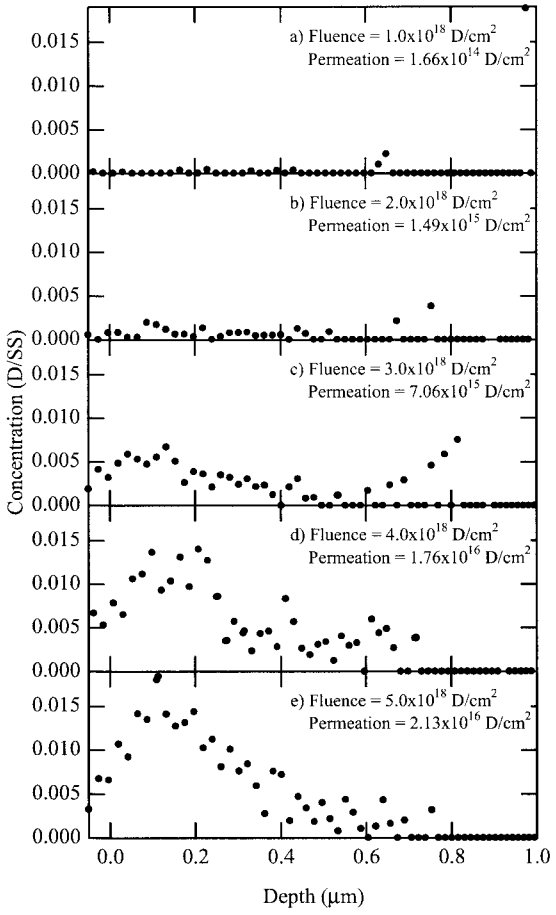

Figure 9.6: The build up of the deuterium concentration in the zirconium layer on the backside of the stainless steel sample during Run 6. The spectra were collected during the bombardment of 650 keV ^{3}He ions to a fluence of $1x10^{16}$ He/cm^2 after each $1x10^{18}$ D (and p)/cm^2 implant cycle. The fluence that is stated in the figure is the total deuterium implanted in the sample when the profile was taken. The deuterium permeation is calculated by integrating the concentration and is listed in the figure.

10 Copper coated SS 316L

Copper coated SS 316L samples were implanted with deuterons during Run 4 and both deuterons and protons during Run 6. The TDS spectra of the released H_2, HD, and D_2 molecules shown in Fig. 10.1 suggest that bubbles are not forming in the copper coating. The deuterium atoms are migrating to the surface of the sample where they recombine with hydrogen causing broad peaks in the HD and D_2 spectra. As with the other samples, the addition of the protons in the implant during Run 6 has reduced the amount of deuterium released as D_2 during the desorption compared to the Run 4 desorption. Fig. 4.1 shows that there is a decrease in the amount of retained deuterium compared to the bare SS 316L sample, but the retention is greater than that of the copper coated Al 6061–T6. The retention in the copper coated SS 316L may have reached saturation, unlike that for the SS 316L.

The SEM images (Fig. 10.2) of the surface of the copper coated SS 316L samples implanted during Run 4 are similar to those of the copper coated Al 6061-T6 sample from Run 4 (Fig. 6.3), therefore the higher resolution images were omitted. As with the copper coated Al 6061-T6, the copper coating was burnished after it was deposited; thus there are two different surfaces, burnished and as-plated. There were signs of etching and pitting of the copper surface due to the deuterium implantation, but no other signs of damage were visible. An optical image of the cross section of the copper coated SS 316L implanted during Run 6 is shown in Fig. 10.3. The coating is approximately 8 μm thick.

The nuclear reaction profiling data of the near surface build up of deuterium in the sample implanted during Run 6 is shown in Fig. 10.4. There is a build up in the concentration of deuterium to about $4x10^{18}$ D (and p)/cm^2 and then a leveling off (see Fig 4.7). The helium profiling of the front surface of the copper coating after the implantation of $5.0x10^{18}$ D (and p)/cm^2 shows that the deuterium is concentrated on or near the surface (see Fig. 10.5). Again, this may be due to the build up of carbon on the surface during implantation or an oxide on the surface. The D(^{3}He,p)^{4}He profiling of the zirconium layer on the back surface of the copper coated SS 316L sample shows that deuterium is permeating through, Fig. 10.6. The permeation is half of that measured from the SS 316L sample, but is still considerable (Fig. 4.8).

The copper coated SS 316L sample retained less deuterium than the SS 316L sample during Run 4, but a little more than the SS 316L sample during Run 6 (Fig. 4.7). The copper coating does reduce the permeating fraction of deuterium compared to SS 316L up to the fluences reached in this experiment. In a comparison to the Al 6061-T6 samples, the copper coated Al 6061-T6 and SS 316L samples have similar retention, but the copper coated Al 6061-T6 samples have lower permeation than the copper coated SS 316L.

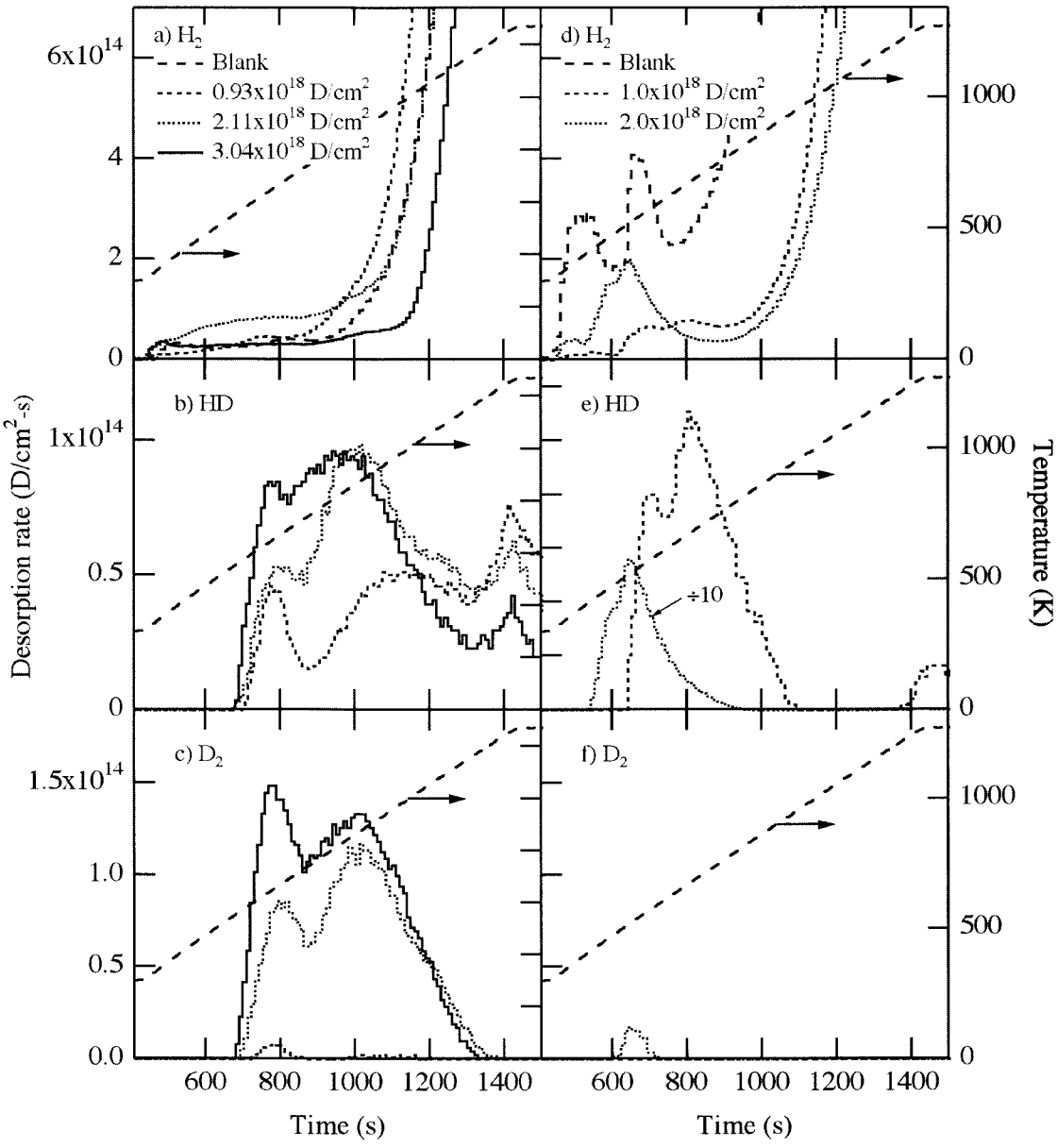

Figure 10.1: a-c) The thermal desorption spectra for the copper coated SS 316L samples implanted with deuterons to fluences of 0.93x10^{18}, 2.11x10^{18}, and 3.04x10^{18} D/cm^2 during Run 4. d-f) The spectra for the copper coated SS 316L samples implanted with protons and deuterons to fluences of 1.0x10^{18} and 2.0x10^{18} during Run 6. The blank samples were not implanted.

a) b)

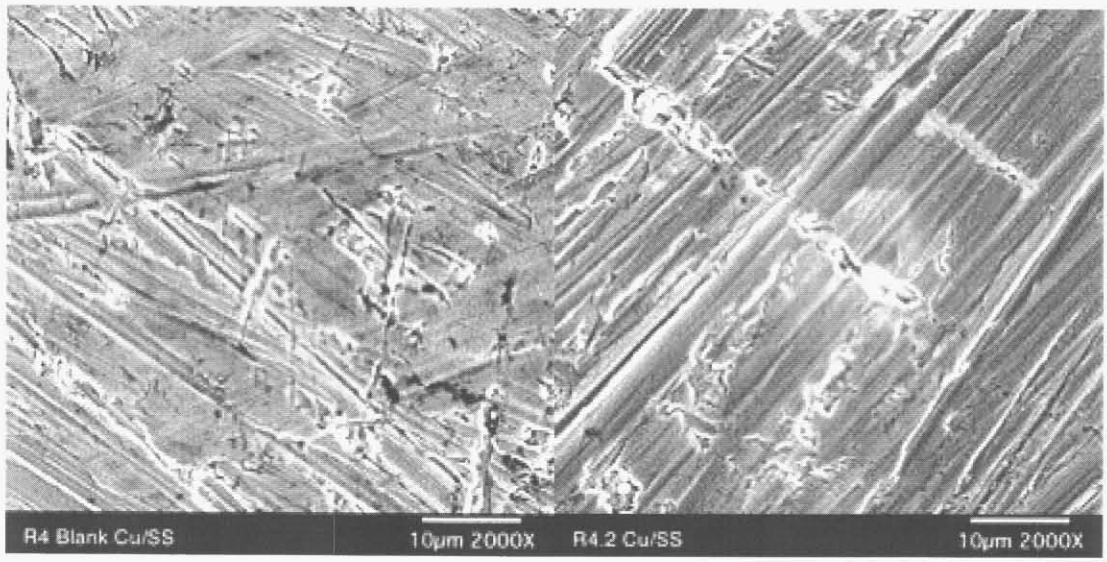

Figure 10.2: SEM images at 2000X of the copper coated SS 316L sample before, a), and after, b), the implantation of 3.04×10^{18} D/cm^2 during Run 4. The surface shows no visible damage due to the implantation.

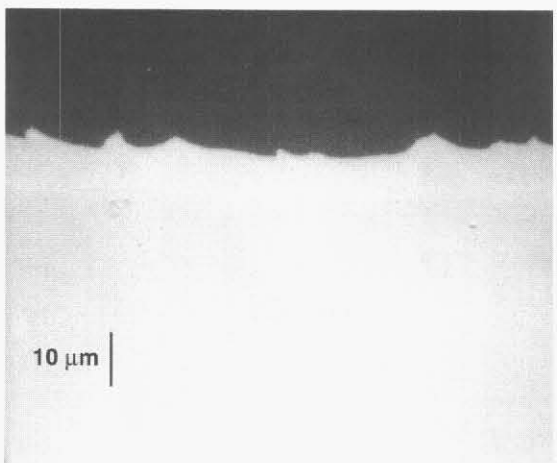

Figure 10.3: An optical image at 1000X of the copper coated SS 316L sample implanted during Run 6. The SS 316L is on the bottom and the lighter layer is the 8 µm thick copper coating. The darker area on top is the potting material.

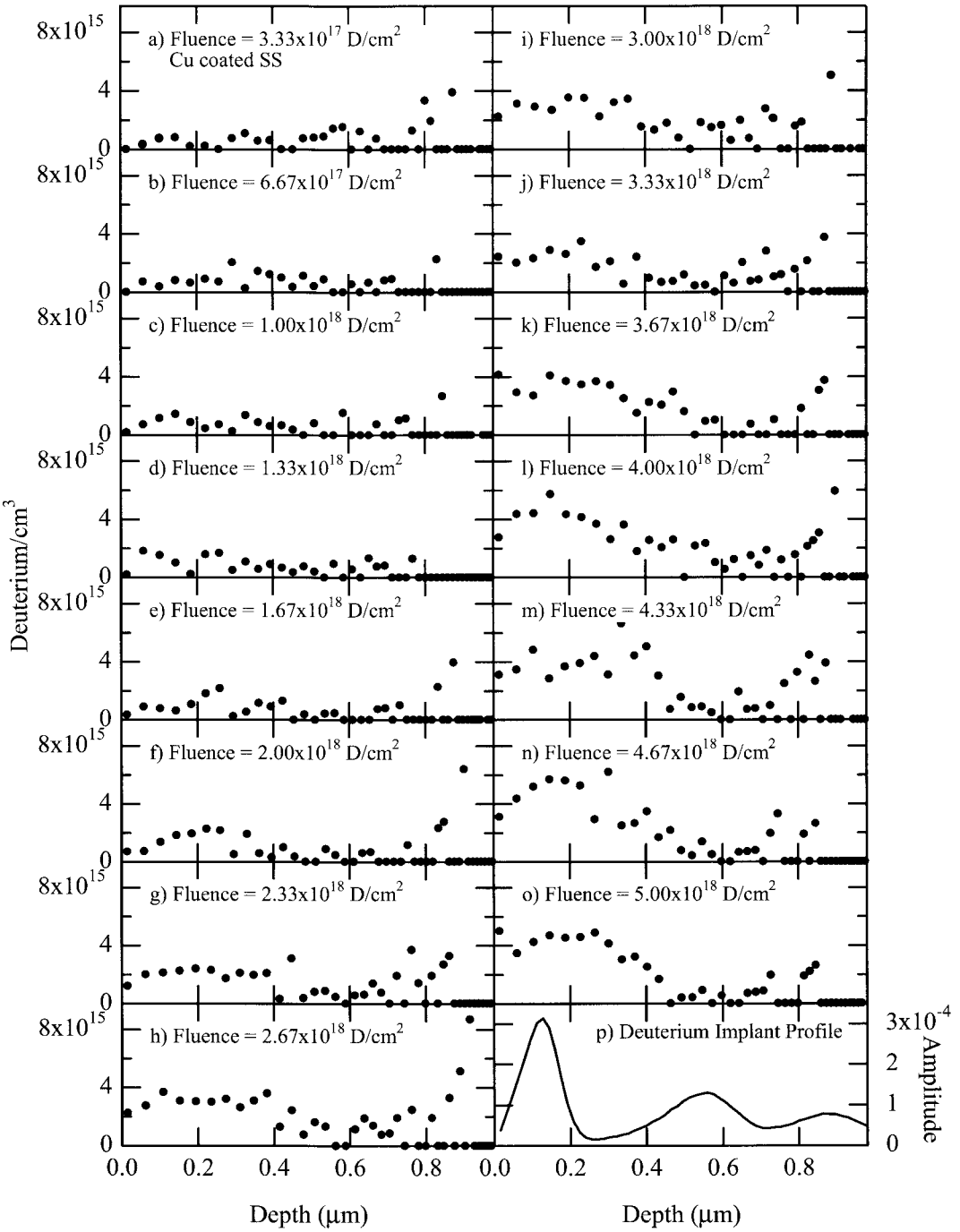

Figure 10.4: The build up of the deuterium concentration in the copper coated SS 316L sample implanted during Run 6. The spectra were collected during the bombardment of 200 keV deuterons to a fluence of 4.76×10^{16} D/cm^2. The fluence that is stated in the figure is the total deuterium implanted in the sample when the profile was taken.

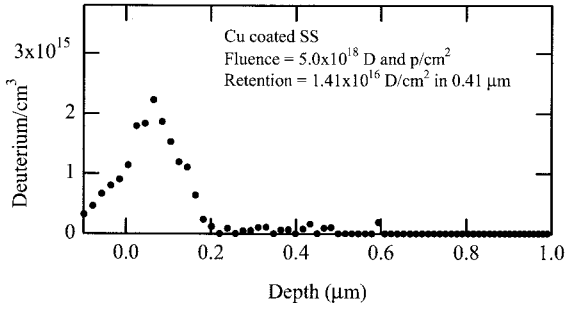

Figure 10.5: The deuterium concentration in the near surface of the front side of the copper coated SS 316L sample after the $5x10^{18}$ D and p/cm^2 implant of Run 6. The spectrum was collected during the bombardment of 650 keV ^{3}He ions to a fluence of $5x10^{15}$ He/cm^2. The retained deuterium is calculated by integrating the concentration.

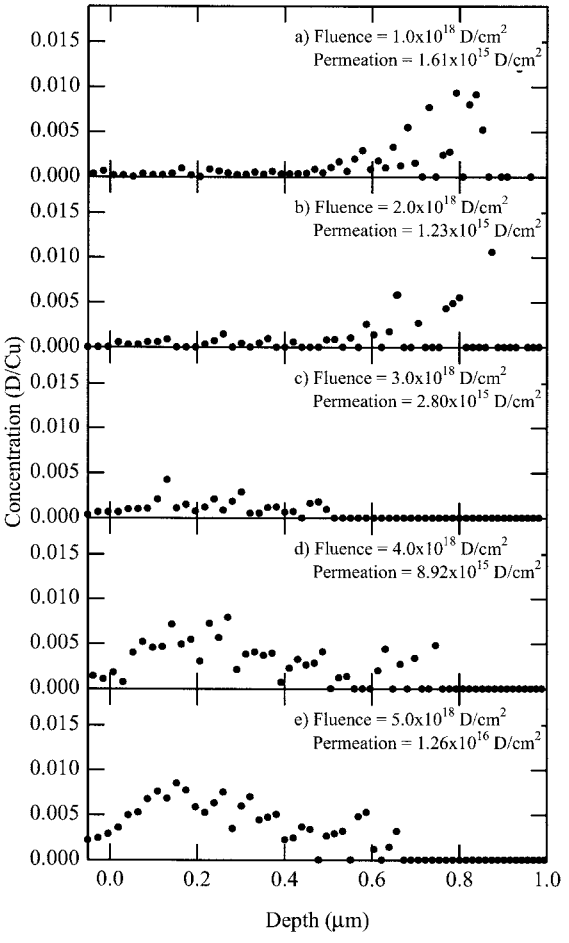

Figure 10.6: The deuterium concentration in the zirconium layer on the backside of the copper coated SS 316L sample during Run 6. The spectra were collected during the bombardment of 650 keV ^{3}He ions to a fluence of $1x10^{16}$ He/cm^2 after each $1x10^{18}$ D (and p)/cm^2 implant cycle. The fluence that is stated in the figure is the total deuterium implanted in the sample when the profile was taken. The permeated deuterium is calculated by integrating the concentration and is listed in the figure.

Intentionally Left Blank

11 Nickel coated SS 316L

Nickel coated SS 316L samples were implanted with deuterons and protons during Run 6. The retention and permeation results from the nickel coated SS 316L samples were very encouraging. The TDS spectra of the released H_2 and HD molecules for samples implanted to $1.0x10^{18}$ and $2.0x10^{18}$ D (and p)/cm^2 are shown in Fig. 11.1. A negligible amount of deuterium was released as HD and no deuterium was released as D_2. The D(d,p)T nuclear reaction profiling of the near surface build up of deuterium shows a steady increase in the concentration of deuterium in Fig. 11.2. The D(^{3}He,p)^{4}He profiling of the front surface of the sample upon completion of the $5.0x10^{18}$ D (and p)/cm^2 implantation shows some deuterium retention on or near the surface in Fig. 11.3. The helium profiling of the front surface of the sample after implantation to $5.0x10^{18}$ D (and p)/cm^2 shows that the deuterium is concentrated at or near the surface. The D(^{3}He,p)^{4}He profiling of the zirconium layer on the back surface of the samples indicates that negligible amounts of deuterium permeated through the nickel coated SS 316L up to a fluence of $5.0x10^{18}$ D (and p)/cm^2, Fig. 11.4. The scatter in the plots is not above statistical scatter. An upper limit to the amount of permeated deuterium is listed in the figure. The solubility of hydrogen graph shown in Fig. 3.5 helps to clarify why nickel may be successful at reducing permeation on stainless steel when copper is not. As discussed in Sec. 3.1.3, there is a discontinuity in deuterium concentration at the interface between the coating and the substrate based on the ratio of the solubility of hydrogen in the coating and in the substrate. The higher solubility of hydrogen in nickel compared to stainless steel would reduce the deuterium concentration in the substrate compared to the coating, whereas copper would have the exact opposite effect. Therefore, the measurements showing permeation in SS 316L and copper coated SS 316L and not in nickel coated SS 316L are expected.

There are no SEM or optical pictures of this sample. The nickel coating was determined to be approximately 8 μm thick using auger depth profiling.

The nickel coated SS 316L sample had excellent results. Measurements of the retention and permeation of deuterium showed negligible amounts. The deuterium measured during the implantation must easily migrate towards the front surface and release.

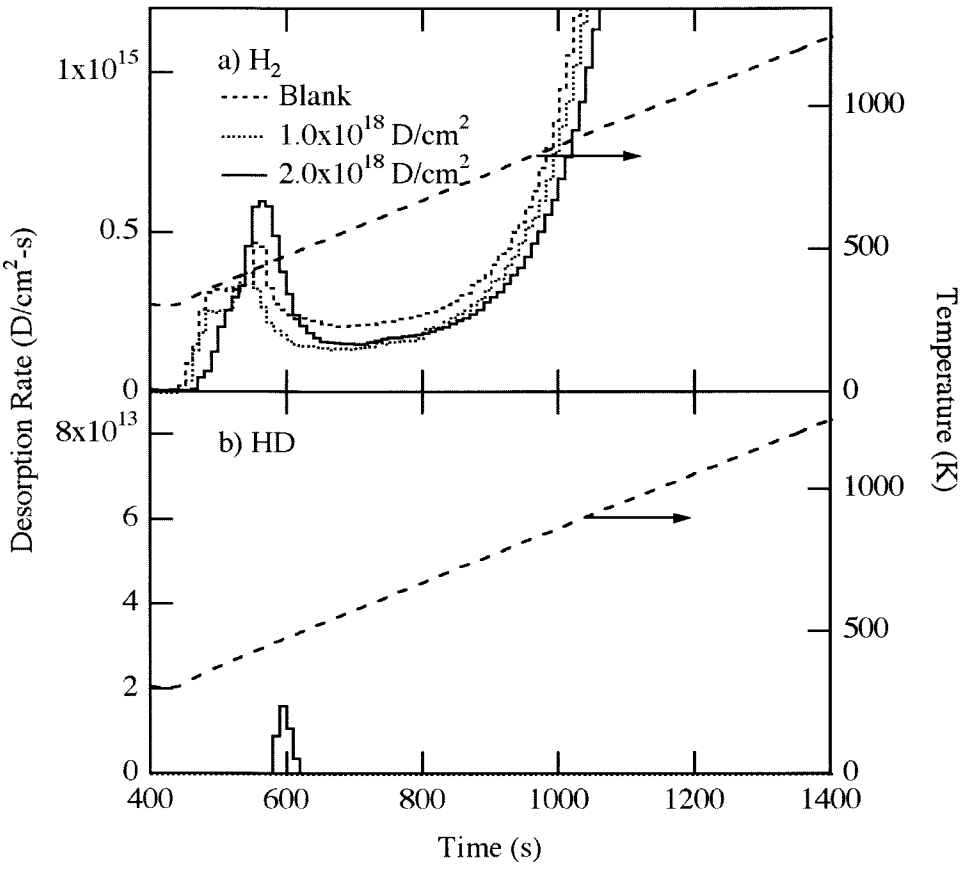

Figure 11.1: The thermal desorption spectra for the nickel coated SS 316L sample implanted with protons and deuterons to fluences of $1.0x10^{18}$ D/cm^2 and $2.0x10^{18}$ D/cm^2 during Run 6.

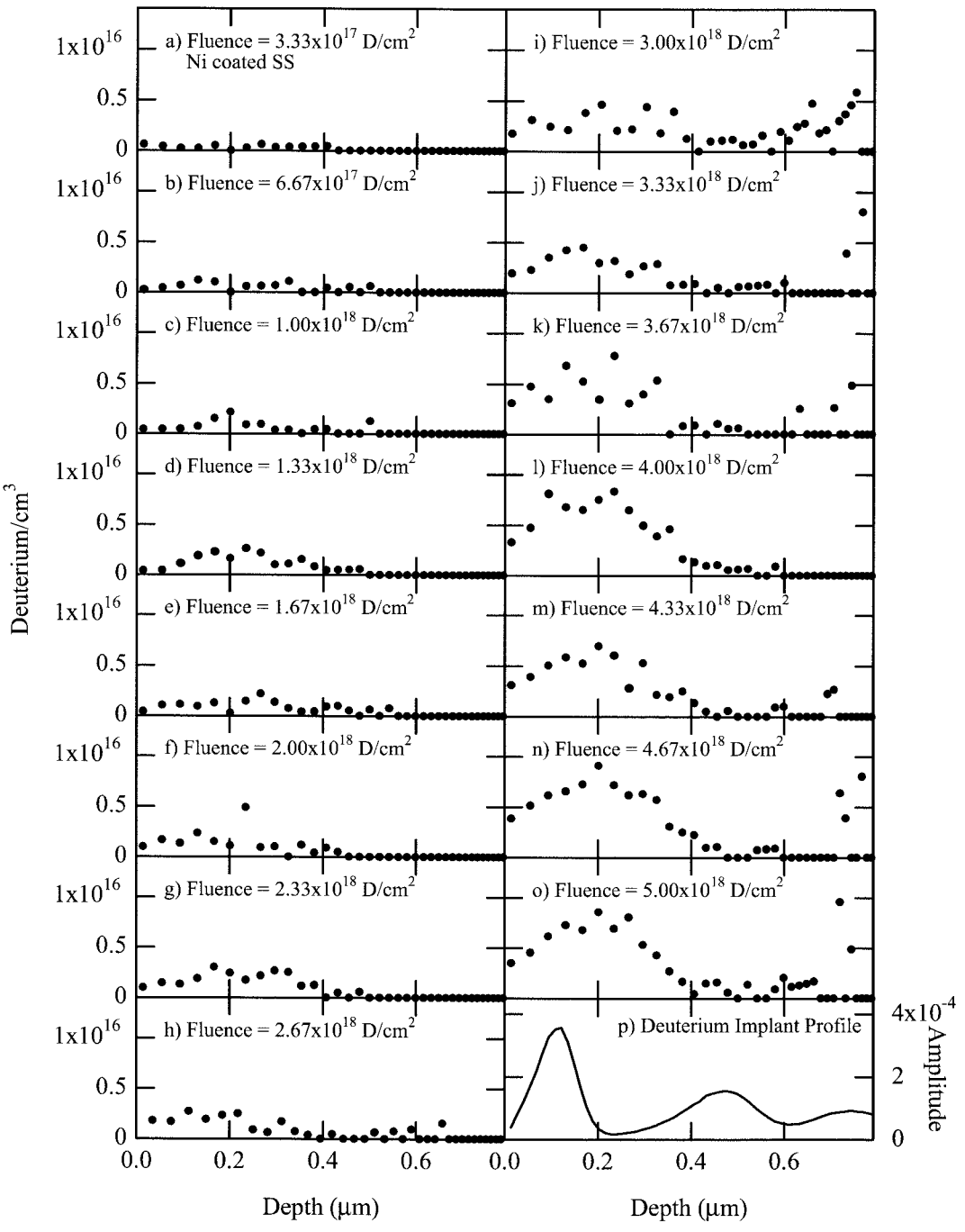

Figure 11.2: The build up of the deuterium concentration in the nickel coated SS 316L sample implanted during Run 6. The spectra were collected during the bombardment of 200 keV deuterons to fluence of 4.76×10^{16} D/cm^2. The fluence that is stated in the figure is the total deuteron implanted in the sample when the profile was taken.

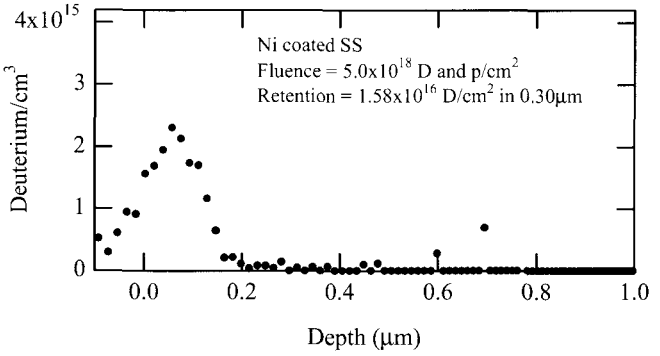

Figure 11.3: The deuterium concentration in the near surface of the front side of the nickel coated SS 316L sample after the $5x10^{18}$ D and p/cm^2 implant of Run 6. The spectrum was collected during the bombardment of 650 keV ^{3}He ions to a fluence of $5x10^{15}$ He/cm^2. The value for the retained deuterium calculated by integrating the deuterium concentration.

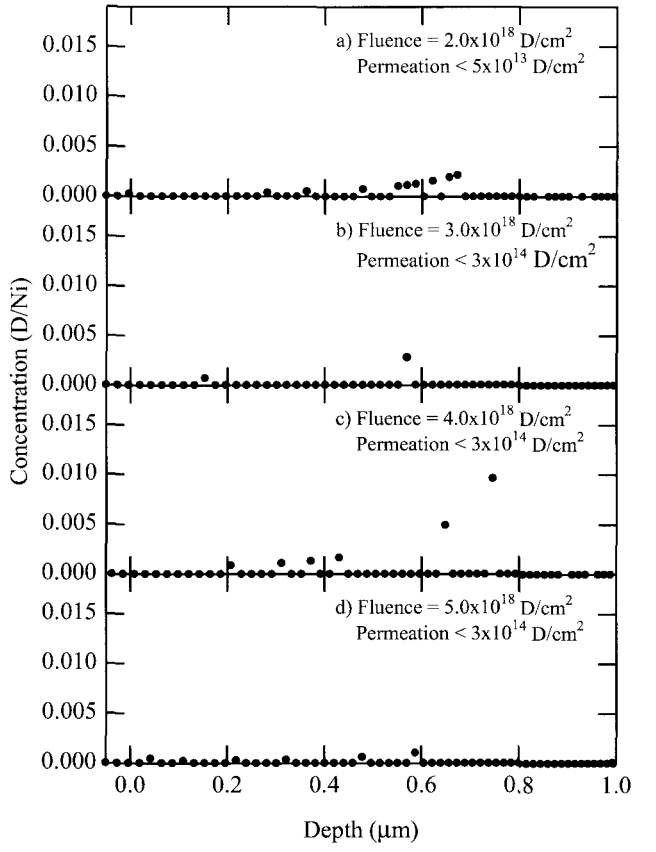

Figure 11.4: The deuterium concentration in the zirconium layer on the backside of the nickel coated SS 316L sample during Run 6. The spectra were collected during the bombardment of 650 keV ^{3}He ions to a fluence of $5x10^{15}$ He/cm^2 in b) and c) and $1x10^{16}$ D/cm^2 in a) and d) after each $1x10^{18}$ D (and p)/cm^2 implant cycle. The fluence that is stated in the figure is the total deuterium implanted in the sample when the profile was taken. No deuterium was mesured in the Zr; the scatter in the plot is due to statistics. An upper limit to the deuterium permeation is given in the figure.

12 Summary

The implantation of deuterons and protons into various Al 6061-T6 and SS 316L samples was completed to examine the hydrogen isotope retention and permeation in candidate materials for APT ^{3}He tube construction. These experiments increased in sophistication from mono-energetic deuteron implants to multi-energetic deuteron and proton implants to more accurately reproduce the conditions expected in APT. The samples implanted during these experiments also increased in sophistication. The 20% retention measured in the bare Al 6061-T6 and 10-20 % retention measured in the bare SS 316L after the implantation of multi-energy deuterons prompted the investigation of coated samples. Micron thick copper, nickel, and anodized aluminum coatings on the front surface of the samples (inside of the APT tube walls) were applied in an attempt to lower retention. The percent deuterium retention and permeation compared to the implanted deuterium are listed for all of the samples tested during these experiments in Table 12.1. A nickel coating approximately 6 μm thick on both the Al 6061-T6 and SS 316L substrates proved to be most successful at reducing both the retention and permeation of deuterium.

DIFFUSE code calculations for the nickel coated aluminum and nickel coated stainless steel samples were completed to indicate the implications to APT. The DIFFUSE code is not able to handle the formation of blisters in the aluminum samples. Therefore, DIFFUSE calculations for the bare aluminum and stainless steel were not completed. The calculations for the nickel coated samples were completed assuming that the average flux of APT is $5x10^{11}$ T/cm^2-s and the total wall area of the tubes is $1.2x10^7$ cm^2. These values estimate that 950 gm-T/yr will be incident on the tube walls. Fig. 12.1 shows retention and permeation calculations for nickel coated aluminum and nickel coated stainless steel for 10 years. The retention shown in Figs. 12.1a) and b) does not take long to reach saturation and is slightly lower in the nickel coated aluminum. After 10 years of operation, only 1 gm of tritium will be retained in the APT tube walls. The permeation shown in Figs. 12.1c) and d) differ by five orders of magnitude. Even with this large difference, the amount of tritium predicted to permeate through the APT tube walls is only $2x10^{-5}$ gm for the nickel coated aluminum and 3 gm for the nickel coated stainless steel.

There are a couple differences between the tritons and protons recoil injected into APT tube walls and the accelerator implantation of deuterons and protons into aluminum that should be mentioned. Fig. 12.2 illustrates these differences. First, three times as many protons as tritons will be injected into the APT tube walls. During these experiments an equal number of protons and deuterons were implanted into the samples. Second, the protons and tritons will be injected simultaneously into the APT tubes. The accelerator implantation of the deuterons and protons were alternated, with the protons implanted last. Kamada et al [50] implanted deuterons and then protons into a sample. The protons were implanted at a greater depth than the deuterons. They found that the protons replaced the deuterons trapped at defects. This is consistent with what was observed during these experiments. The samples implanted with only deuterons retained more deuterium than samples implanted with

deuterons and then protons (see Table 12.1). These two differences are not expected to have a large effect on the retention and permeation measured in the accelerator experiments.

The reduction in both retention and permeation produced by the nickel coatings and the ability to apply them to the inside of the APT tubes, indicate that both nickel coated Al 6061-T6 and nickel coated SS 316L tubes would be effective for use in APT.

Table 12.1: A summary of the deuterium retention and permeation measurements for samples implanted in this study. Column three lists the deuterium retention measured in samples implanted with multi-energy deuterons during Runs 2 and 4. Columns four and five list the deuterium retention and permeation, respectively, measured in samples implanted with multi-energy deuterons and protons during Runs 5 and 6. The percent listed is the percent of deuterium measured compared to the total implanted deuterium. The spaces left blank were not measured during these experiments.

Sample	Fluence (D/cm^2)	Retention - D (%)	Retention – D and p (%)	Permeation – D and p (%)
6061-T6 Al	$1x10^{18}$		5.4	0
	$2x10^{18}$		9.4	0
	$3x10^{18}$			0
	$3.5x10^{18}$	20.0		
Cu/Al	$1x10^{18}$	1.5		0
	$2x10^{18}$	0.6		0
	$3x10^{18}$	1.4	1.1	0
Ni/Al	$1x10^{18}$		0	0
	$2x10^{18}$		0.02	0
	$3x10^{18}$		0	0
Anodized Al	$1x10^{18}$		4.9	
	$2x10^{18}$		10.9	
316L SS	$1x10^{18}$	20.5	2.7	0.017
	$2x10^{18}$	10.1	2.5	0.075
	$3x10^{18}$	8.6		0.235
	$4x10^{18}$			0.440
	$5x10^{18}$			0.426
Cu/SS	$1x10^{18}$	5.5	2.9	0.161
	$2x10^{18}$	12.5	4.5	0.062
	$3x10^{18}$	5.4		0.093
	$4x10^{18}$			0.223
	$5x10^{18}$			0.225
Ni/SS	$1x10^{18}$		0	0
	$2x10^{18}$		0.03	0
	$3x10^{18}$			0

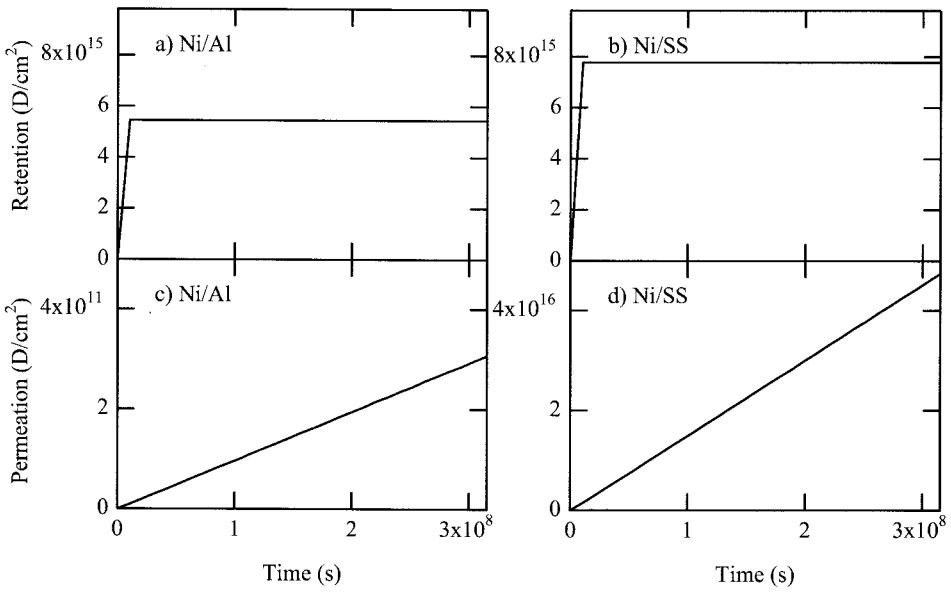

Figure 12.1: Calculations using the computer code DIFFUSE to predict the retention of a) nickel coated aluminum and b) nickel coated stainless steel and the permeation of c) nickel coated aluminum and d) nickel coated stainless steel over 10 years of APT operation based on measured deuterium retention and permeation.

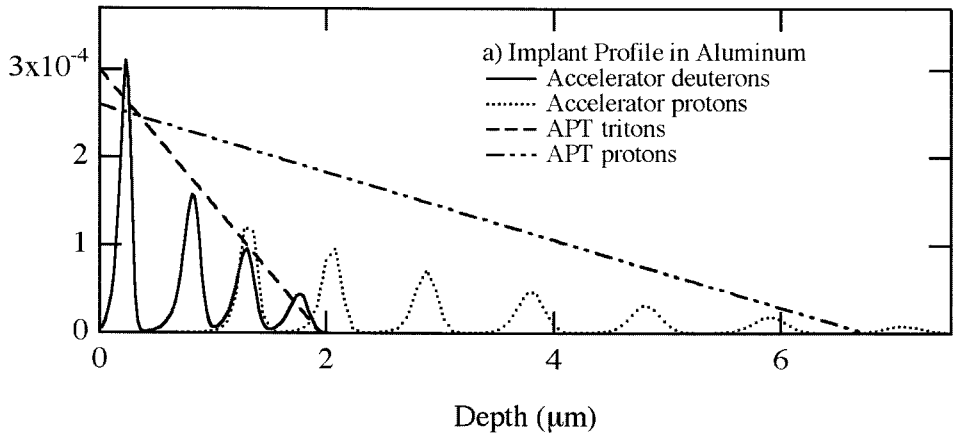

Figure 12.2: Implantation profiles for deuterons (solid curve) and protons (dotted curve) implanted into aluminum during these accelerator experiments. The implanted profiles are compared to the theoretical deuteron (dashed line) and proton (dash-dot line) implant profiles expected for the aluminum tubes in APT.

Intentionally Left Blank

13 References

1. L. Katz, M. Guinan and R. J. Borg, Phys. Rev. B**4** (1971) 330.
2. J. F. Ziegler, J. P. Biersack and U. Littmark, "The Stopping and Range of Ions in Solids", volume 1, Pergamon Press, New York, 1985.
3. D. F. Cowgill, Nucl. Inst. and Meth. **145** (1977) 507-516.
4. J. L. Tuck, Nucl. Fusion **1** (1961) 201.
5. E. J. Konopinski and E. Teller, Phys. Rev. **73** (1948) 822.
6. W. Moller and F. Besenbacher, Nucl. Inst. and Meth. **168** (1980) 111-114.
7. M. I. Baskes, J. Nucl. Mater. **92** (1980) 318-324.
8. T. Ishikawa and R. B. McLellan, Acta Metall. **34** (1986) 1091-1095.
9. W. Eichenauer and A. Pebler, Z. Mettallkde. **48** (1957) 373-377.
10. W. M. Robertson, Z. Metallkde. **64** (1973) 436-443.
11. M. R. Louthan, Jr. and R. G. Derrick, Corr. Sci. **15** (1975) 565-577.
12. W. Eichenauer, K. Hattenbach, and A. Pebler, Z. Metallkde. **52** (1961) 682-684.
13. M. Nakashima, Y. Aratono and E. Tachikawa, J. Nucl. Mater. **98** (1981) 27-34.
14. T. Tanabe, Y. Furuyama, N. Saitoh and S. Imoto, Trans. Jap. Inst. Met. **28** (1987) 706-714.
15. L. Katz, M. Guinan and R. J. Borg, Phys. Rev. B **4** (1971) 330-341.
16. K. Yamakawa, J. Phys. Soc. Japan, **47** (1979) 114-121.
17. D. M. Grant, D. L. Cummings and D. A. Blackburn", J. Nucl. Mater. **152** (1988) 139.
18. H. K. Perkins and Y. Noda, J. of Nucl. Mater. **71** (1978) 349-364.
19. O. Gautsch and G. Hoddap, J. Nucl. Mater. **152** (1988) 35.
20. H. Katsuta and K. Furukawa, J. Nucl. Sci. and Tech. **18** (1981) 143.
21. W. Eichenauer, W. Loser and H. Witte, Z. Mettallkde. **56** (1965) 287-293.
22. S. Yamaguchi, S. Nagata, K. Takahiro and S. Yamamoto, J. Nucl. Mater. **220-222** (1995) 878-882.
23. K. Kamada, A. Sagara, N. Sugiyama, and S. Yamaguchi, J. Nucl. Mater. **128-129** (1984) 664-669.
24. T. Hayashi, K. Okuno, K. Yamanaka, and Y. Naruse, J. Alloys Comp. **189** (1992) 195-199.

25. K. L. Wilson, R. A. Causey, M. I. Baskes and J. Kamperschroer, J. Vac. Sci. Technol. A **5** (1987) 2319-2324.

26. F. Besenbacher, J. Bottiger and S. M. Myers, J. Appl. Phys. **53** (1982) 3536-3546.

27. S. M. Myers and W. R. Wampler, J. Nucl. Mater. **111-112** (1982) 579.

28. R. A. Causey, R. A. Kerst and B. E. Mills, J. Nucl. Mater. **122-123** (1984) 1547-1552.

29. D. Presinger, P. Borgesen, W. Moller and B. M. U. Scherzer, Nucl. Instr. and Meth. B **9** (1985) 270.

30. T. Nagasaki, R. Yamada and H. Ohno, J. Nucl. Mater. **191-194** (1992) 258-262.

31. K. Yamaguchi, T. Namba and M. Yamawaki, J. Nucl. Sci. Technol. **24** (1987) 915.

32. P. Borgesen, B. M. U. Scherzer and W. Moller, Nucl. Instr. and Meth. B **9** (1985) 333.

33. R. A. Causey and M. I. Baskes, J. Nucl. Mater. **145-147** (1987) 284-287.

34. M. Braun, B. Emmoth, F. Waelbroeck and P. Wienhold, J. Nucl. Mater. **93-94** (1980) 861.

35. E. W. Thomas and M. Braun, J. Nucl. Mater. **111-112** (1982) 655.

36. F. Waelbroeck, J. Winter and P. Wienhold, J. Nucl. Mater. 111-112 (1982) 185.

37. K. L. Wilson and L. G. Haggmark, Thin Solid Films **63** (1979) 283.

38. Y. Kido, M. Kakeno, K. Yamada, T. Hioki and J. Kawamoto, J. Phys. F: Met. Phys. **12** (1982) 1567-76.

39. S. M. Myers, F. Besenbacher and J. K. Norskov, J. Appl. Phys. **58** (1985) 1841-1850.

40. S. M. Myers and D. M. Follstaedt, J. Nucl. Mater. **145-147** (1987) 322-325.

41. F. Besenbacher, B. Bech Nielsen and S. M. Myers, J. Appl. Phys. **56** (1984) 3384-3393.

42. M. Fukui, R. Sakamoto, K. Araki, T. Fujiwara, T. Muroga and N. Yoshida, J. Nucl. Mater. **220-222** (1995) 810-814.

43. P. B. Johnson and T. R. Armstrong", Nucl. Instr. Meth. **148** (1978) 85-92.

44. P. B. Johnson and T. R. Armstrong, Appl. Phys.Lett. **31** (1977) 325-327.

45. O. Petitpierre, W. Moller and B. M. U. Scherzer, J. Appl. Phys. **65** (1989) 1893-1897.

46. P. Borgesen, B. M. U. Scherzer and W. Moller, J. Appl. Phys. **57** (1985) 2733-2738.

47. K. L. Wilson and M. I. Baskes, J. Nucl. Mater. **76-77** (1978) 291-297.

48. K. L. Wilson and M. I. Baskes, J. Nucl. Mater. **111-112** (1982) 622-627.

49. J. Bohdansky, K. L. Wilson, A. E. Pontau, L. G. Haggmark and M. I. Baskes, J. Nucl. Mater. **93-94** (1980) 594-600.

50. K. Kamada, A. Sagara and S. Yamaguchi, Rad. Effects Lett. **86** (1985) 255-264.

51. K. Kamada, A. Sagara, H. Kinoshita and H. Takahashi, J. of Nucl. Mater. **155-157** (1988) 427-430.

52. W. Song, J. Du, Y. Xu and B. Long, J. of Nucl. Mater. **246** (1997) 139-143.

Intentionally Left Blank

Appendix A Supporting Documents and Calibrations

1. ES&H Standard Operating Procedure (SOP)
   Title: Accelerator Laboratory (U)
   Location: Bldg. 916, Room 104

2. FY98 Research Plan for the Deuterium Accelerator Experiments Performed for the Accelerator Production of Tritium Program.

3. Test Plan for Run 5: High Flux Deuteron and Proton Implantation Experiment.
   APT-MP-98-03

TIFIED INSPECTION REPORT

ALUMINUM COMPANY OF AMERICA
CUSTOMER P.O . . GOVT CONTRACT NO.
2024 /
PITTSBURGH, PA.
SHIPPED FROM: RIVERDALE IOWA
PAGE 001

We hereby certify that the material covered by this certificate has been inspected in accordance with, and has been found to meet, the applicable requirements described thereon, including any specifications forming a part of the description and that certain representative of the material has the composition limits and has the mechanical properties shown on the face of this sheet. Per
SAM L. SHELBY
Quality Assurance Manager

T C I ALUMINUM
2353 DAVIS AVE
HAYWARD, CA 94545

T C I ALUMINUM
2353 DAVIS AVENUE
HAYWARD, CA 94545

04-001

MF
1913

Invoice No.	Invoice Date	Code
22538918	95/01/17	280 867866
ALCOA No.	Ship Date	VIA
DS 58943	95/01/17	DAVIS TRANSPORT

Product Description: SHEET
B/L No.: 57536
Gross Weight: 1996
Alloy-Temper: 6061 T6

ITEM DESCRIPTION	Quantity Shipped PCS., FT., ETC.	Quantity Shipped Pounds	# of Tests & Dir[1]		Test[2]	Test[2]	Test[2]	Test[2]	Test[2]	Test[2]	Test[2]
					UTS1	TYS1	EL4D				
ITEM 1		1756									
.0320 IN TK X 48.000 IN W X											
144.000 IN LN CAT D 126859 (M)	LOT-622672	T6	8 L.T	MAX	49.0	39.6	13.5				
A/T 6061-T6 FLAT SHEET FOR	84PC			MIN	47.7	38.8	12.5				
DISTRIBUTORS TOLERANCE GUARANTEED											
PER QQ-A-250/11 REV F NT 1	SI FE	CU MN	MG CR	ZN TI							
& EXCEPT MARKING AMS4027 REV L	.64 .47	.25 .10	.99 .19	.00 .02							
& EXCEPT MARRING ASTMB209 REV 93	Cast analysis from a representative sample during the casting process										
((MARKED)) INTERLEAVED											
SKID WGT: 4500 LB											
QUAN TOL +/-10 %											
QPR D126859 REV 12											
CUST REQ 95-01-16											
***											
Pkg-No Lot-No Wgt Pc											
307141 622672 1756 84											

Chemical Composition	SI	FE	CU	MN	MG	CR	ZN	TI	OTHER EACH	OTHER TOTAL	ALUMINUM
Max.	.8	.7	.40	.15	1.2	.35	.25	.15	.05	.15	REMAINDER
Alloy 6061 Min.	.40		.15		.8	.04					
Chemical Composition Max.											
Min.											

1. When 2 or more tests per lot are made, the highest and the lowest values are reported for each property determined.
2. See test abbreviation explanation on the back of this sheet

T.C.I. ALUMINUM/NORTH TEL NO. 510 786 3302 Nov 08,96 15:55 P.02

Figure A. 1: The certification paper for the Al 6061-T6 used to make the samples implanted during the accelerator experiments.

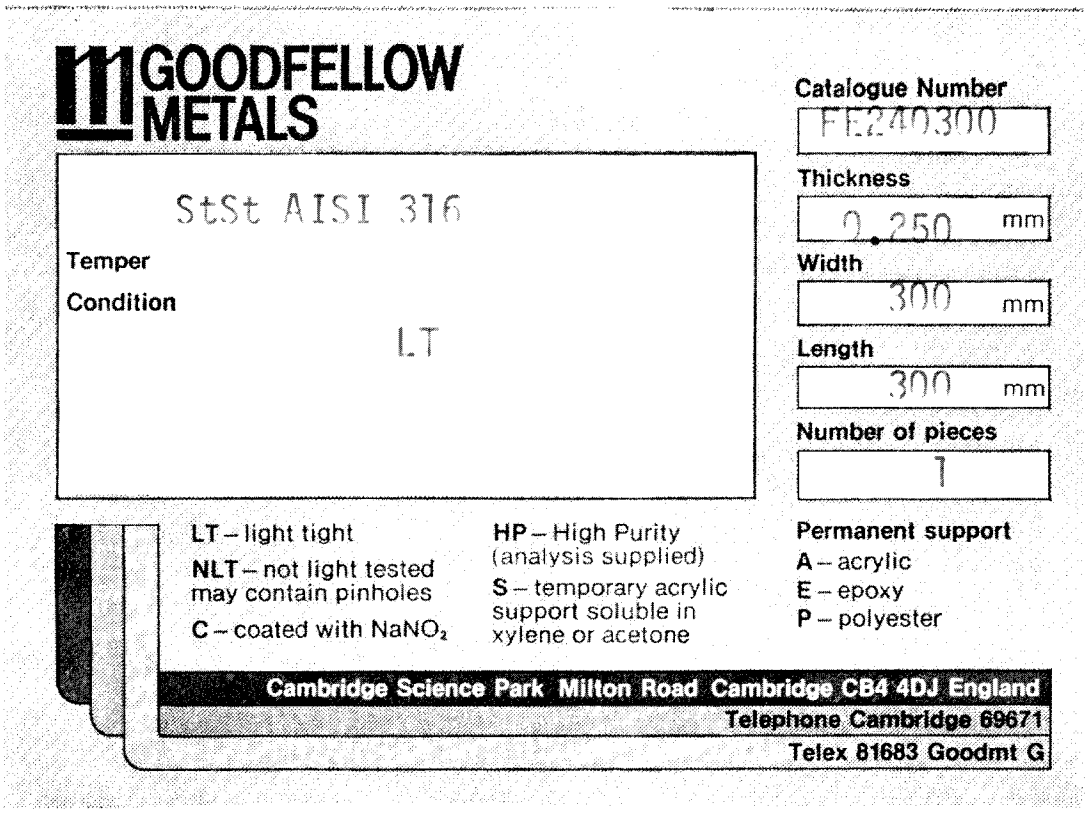

Figure A. 2: The label from the SS 316L used to make the samples implanted during the accelerator experiments.

PRIMARY STANDARDS LABORATORY

Sandia National Laboratories, Albuquerque, New Mexico 87185

CERTIFICATE

THERMOCOUPLE METER — File No. 23465
OMEGA
Model No. DP25-TC-A — *LIMITED*
Serial No. 7015800

with
THERMOCOUPLE (30' Type K):
OMEGA
Model No. GG-K-24SLE
Serial No. KA

Submitted by: Organization 08715
SNL/CA

Certified: March 03, 1997
Expires: September 03, 1997

The Digital Thermometer and thermocouple above were tested over the following range of temperatures by comparison to a calibrated Standard Platinum Resistance Thermometer (SPRT), and found to be within the following accuracy for the thermocouple type and temperature range listed below:

TC TYPE	RANGE	ACCURACY
K	50°C to 100°C	± 1.0°C

It is probable that the instrument and thermocouple combination will remain within the above accuracy for the certification interval.

Metrologist: WRA W. R. Anderson, Jr., 01541

Approved by: R. R. Romero, 01541

Copy to: Submitting organization
Organization 01541 File

Date received: 2/11/97
Date tested: 3/03/97

Page 1 of 2

Figure A. 3: The certification for the thermocouple meter and wire connected to the sample block during the implantation experiments.

Table A. 1: The label from the deuterium leak used to calibrate the thermal desorption measurements during these experiments.

Variable activity = 3.7e10
// Assume 1 Ci alpha decaying parent.
Variable thick = 0.313*2.54
// Thickness of the puck in cm.
Vacuum Instrument Corp.
Ronkonkoma, NY
(516) 737-0900	

Model OM-6DX Glass Capillary/922608	
Gas	Deuterium
Leak Rate	2.23x10-6 atm-cc/sec
Pressure	215 PSIA
10% Fall off date	11/2002
Temperature	24.44 C
Temp. Coeff.	0.2 %/C
Serial #	06-748 Sandia
Cal. Date	2/5/1997
P/N 487-294-1001 9/91	

14 Distribution

UNCLASSIFIED Unlimited Release Documents:

3	MS 9018	Central Technical Files, 8945-1
1	MS 0899	Technical Library, 9616
1	MS 9021	Classification Office, 8511 for Technical Library, MS 0899, 9616
1		DOE/OSTI via URL
2	MS 9402	Don Cowgill
2		Kristin Hertz
5		Rion Causey
1		John Goldsmith